

**RATIO-BASED EDGE DETECTION INSPIRED SPECKLE REDUCING  
ANISOTROPIC DIFFUSION**

(Thesis format: Monograph)

by

Asaduzzamana Babu

Graduate Program in Computer Science

A thesis submitted in partial fulfillment  
of the requirements for the degree of  
Master of Science

The School of Graduate and Postdoctoral Studies  
The University of Western Ontario  
London, Ontario, Canada

© 2013 Asaduzzaman Babu

## Abstract

Speckle Reducing Anisotropic Diffusion, SRAD, is a multiplicative speckle noise reduction method. In highly speckled environment, SRAD occasionally produces over-smoothed, dislocated/broadened edge lines and inadequate de-noising on homogeneous image regions where the speckles are well developed. Moreover, the performance of SRAD is highly dependent on the initial selection of a good homogeneous area. To overcome these weaknesses, we propose two different ratio-based edge detection inspired extensions to SRAD. One of the proposed extensions incorporates an edge-sensitive boosting factor to guide the gradient and Laplacian operator based edge detector of SRAD. The edge-sensitive boosting factor is defined by the global edge information provided by a ratio based edge detector. The other proposed extension introduces a weighted diffusion function in the original diffusion model of SRAD. The proposed diffusion function is a weighted sum of two components – (1) a global ratio-based edge detection inspired component and (2) the original diffusion function of SRAD. A common scaling function selection strategy for both extensions and the use of a larger window size for gathering local statistics have also been proposed. The proposed filters show significant improvement in speckle de-noising and edge preservation.

**Keywords:** speckle, speckle reduction, multiplicative noise reduction, anisotropic diffusion, ratio-based edge detection, edge preservation, SRAD.

# **Dedication**

To

the loving memories of my late father.

## **Acknowledgments**

This dissertation would not have been possible without the guidance and motivation of several individuals. First, I would like to express my sincere gratitude and thanks to my supervisor Prof. Mahmoud R. El-Sakka. I am blessed by his guidance, consistent support, constructive criticism and continuous encouragement. I couldn't have imagined having a better mentor for my research work.

I would also like to thank my colleagues and lab-mates for their great support and encouragement. I consider myself lucky to get a chance to work with such friendly and intelligent individuals.

I would like to mention my ex-supervisor, late Prof. Sheng Yu, for the great care and encouragement I received from him at the early days of my Masters program. I will definitely cherish the four invaluable months under his supervision. His sudden death was a great shock to me. Thanks again to Prof. Mahmoud R. El-Sakka for his tremendous support at that period.

Last but not the least, I would like to thank my family: my late father, my mother, wife and brothers for their endless support and encouragement throughout the different stages of my life.

## List of Abbreviations

AD	Anisotropic Diffusion
DeSpeRADO	Deconvolutional Speckle Reducing Anisotropic Diffusion
DPAD	Detail Preserving Anisotropic Diffusion
FOM	Figure of Merit
ICOV	Instantaneous Coefficient of Variation
JPL	Jet Propulsion Laboratory
MROA	Modified Ratio of Averages
MSP-RoA	Maximum Strength Edge Pruned Ratio of Averages
MSSIM	Mean Structural Similarity Index Measure
OSRAD	Oriented Speckle Reducing Anisotropic Diffusion
PDE	Partial Differential Equation
REDISRAD	Ratio-based Edge Detection Inspired Speckle Reducing Anisotropic Diffusion
REDISRAD-EBF	REDISRAD with Edge-sensitive Boosting Factor
REDISRAD-WDF	REDISRAD with Weighted Diffusion Function
RGoA	Ratio and Gradient of Averages
RoA	Ratio of Averages
SAR	Synthetic Aperture Radar
SAS	Synthetic Aperture Sonar
SPLab	Signal Processing Lab
SRAD	Speckle Reducing Anisotropic Diffusion
SSIM	Structural Similarity Index Measure

# Table of Contents

<b>Abstract</b> .....	ii
<b>Dedication</b> .....	iii
<b>Acknowledgments</b> .....	iv
<b>List of Abbreviations</b> .....	v
<b>Table of Contents</b> .....	vi
<b>List of Tables</b> .....	viii
<b>List of Figures</b> .....	ix
<b>Chapter 1: Introduction</b> .....	1
1.1 Speckle .....	2
1.2 Various approaches to speckle reduction.....	2
1.3 Motivations and contributions .....	3
1.4 Thesis contributions .....	5
1.5 Thesis outline .....	5
<b>Chapter 2: Background</b> .....	6
2.1 Model of speckle noise .....	6
2.2 Model of speckle noise .....	8
2.2.1 Homomorphic filters.....	8
2.2.2 MMSE based non-iterative adaptive filters .....	9
2.2.3 Anisotropic diffusion based adaptive filters .....	12
2.2.4 Wavelet based adaptive filters .....	19
2.3 Edge detection in speckled image.....	22
2.3.1 Ratio-based edge detection methods.....	22
2.3.2 Gradient/Laplacian-based Vs ratio-based edge detection.....	25
<b>Chapter 3: Methodology</b> .....	28

3.1	Guidance of ratio-based edge detection .....	30
3.1.1	Generating ratio and direction matrices .....	30
3.1.2	Acquisition of global edge information .....	31
3.1.3	Guidance of global edge information .....	35
3.2	Modified scaling factor and ICOV coefficient .....	39
3.2.1	Scaling factor selection strategy .....	39
3.2.2	ICOV coefficient calculation using larger window .....	40
<b>Chapter 4: Experimental Results and Analysis .....</b>		<b>42</b>
4.1	Datasets and performance measures .....	42
4.1.1	Datasets used in different experiments .....	42
4.1.2	Performance measures .....	44
4.2	Parameter adjustment for the proposed filters .....	47
4.2.1	Window size for ICOV calculation.....	47
4.2.2	Weight constant $m$ of REDISRAD-WDF .....	51
4.3	Experimental settings.....	51
4.4	Experimental results and analysis.....	52
4.4.1	Edge and structural similarity preservation .....	52
4.4.2	Mean preservation and variance reduction .....	60
4.4.3	Intensity profiles .....	64
4.4.4	Effectiveness on real-world speckled images .....	71
4.5	Overall results discussion .....	95
<b>Chapter 5: Concluding Remarks and Future Work .....</b>		<b>96</b>
5.1	Conclusion .....	96
5.2	Future work.....	97
<b>References .....</b>		<b>99</b>
<b>Curriculum Vitae .....</b>		<b>104</b>

## List of Tables

Table 4.1	FOM and MSSIM values of REDISRAD-EBF for various window sizes. ....	48
Table 4.2	FOM and MSSIM values of REDISRAD-WDF for various window sizes. ....	48
Table 4.3	FOM and MSSIM values of REDISRAD-WDF for different values of the weight constant.....	51
Table 4.4	Results of edge and structural similarity preservation experiment on synthetic dataset with two different noise levels.....	56
Table 4.5	Results of edge and structural similarity preservation experiment on semi-synthetic dataset.....	59
Table 4.6	Mean preservation and variance reduction results for the synthetic input image corrupted by a multiplicative Gaussian noise with zero mean and standard deviation of 0.35 .....	61
Table 4.7	Mean preservation and variance reduction results for the synthetic input image corrupted by a multiplicative Gaussian noise with zero mean and standard deviation of 0.50 .....	61
Table 4.8	Mean preservation and variance reduction results for the semi-synthetic input image –Lena, corrupted by a multiplicative Gaussian noise with zero mean and standard deviation of 0.50.....	63
Table 4.9	Mean preservation and variance reduction results for the semi-synthetic input image –Parrots, corrupted by multiplicative Gaussian noise with zero mean and standard deviation of 0.50.....	63

## List of Figures

Figure 2.1	Four usual directions to partition a $W \times W$ window into two adjacent and non-overlapping regions.....	23
Figure 2.2	Pruning directions perpendicular to four window-partitioning directions. ....	24
Figure 2.3	A simple plot to illustrate the properties of multiplicative noise. ....	25
Figure 2.4	Edge maps of the speckled version of the standard image Lena generated by gradient and ratio-based methods.....	26
Figure 3.1	A pictorial demonstration of the major weaknesses of SRAD.....	29
Figure 3.2	Curves representing two monotonically increasing functions proposed for the modeling of the global diffusion function of REIDSRAD-WDF. ....	34
Figure 4.1	Synthetic dataset used for experiments..	43
Figure 4.2	Semi-synthetic dataset used for experiments. ....	43
Figure 4.3	Performances of REDISRAD-EBF for various window sizes used in ICOV calculation.....	49
Figure 4.4	Performances of REDISRAD-WDF for various window sizes used in ICOV calculation.....	50
Figure 4.5	Three different homogeneous regions (for scaling factor calculation) on the artificially speckled synthetic image, denoted by R-1, R-2 and R-3.....	53
Figure 4.6	Results of various filters on an image (synthetic) with multiplicative noise with zero mean and standard deviation of 0.35. ....	53
Figure 4.7	Results of various filters on an image with multiplicative noise with zero mean and standard deviation of 0.50.....	54
Figure 4.8	146% zoomed view of a $138 \times 101$ sub-region from the top-left corner of the output images.....	56
Figure 4.9	Homogeneous regions on corrupted Lena and Parrots .....	58
Figure 4.10	Results of various filters on an image (Lena) corrupted by a multiplicative noise with zero mean and standard deviation of 0.50. ....	58
Figure 4.11	Results of various filters on an image (Parrots) corrupted by a multiplicative noise with zero mean and standard deviation of 0.50. ....	59

Figure 4.12	Three homogeneous regions on the synthetic image to evaluate mean preservation and variance reduction performance.....	61
Figure 4.13	Three homogeneous regions on the semi-synthetic images to evaluate mean preservation and variance reduction performance.....	62
Figure 4.14	Scan line on the synthetic image for intensity profile generation .....	64
Figure 4.15	Intensity profiles of the original and noisy synthetic images along the scan line.....	65
Figure 4.16	Intensity profiles of the original synthetic image and de-noised output image generated by Lee filter.....	67
Figure 4.17	Intensity profiles of the original synthetic image and de-noised output image generated by Frost filter.....	67
Figure 4.18	Intensity profiles of the original synthetic image and de-noised output image generated by homomorphic AD filter.....	68
Figure 4.19	Intensity profiles of the original synthetic image and de-noised output image generated by DPAD filter.....	68
Figure 4.20	Intensity profiles of the original synthetic image and de-noised output image generated by SRAD filter.....	69
Figure 4.21	Intensity profiles of the original synthetic image and de-noised output image generated by OSRAD filter.....	69
Figure 4.22	Intensity profiles of the original synthetic image and de-noised output image generated by REDISRAD-EBF filter.....	70
Figure 4.23	Intensity profiles of the original synthetic image and de-noised output image generated by REDISRAD-WDF filter.....	70
Figure 4.24	Real SAR images captured by NASA SIR-C/X-SAR system.....	72
Figure 4.25	A 150×90 rectangular area at the top-left corner of each SAR image.....	73
Figure 4.26	Two SAR images de-noised by the Lee filter.....	76
Figure 4.27	Two SAR images de-noised by the Frost filter.....	77
Figure 4.28	Two SAR images de-noised by the homomorphic AD filter.....	78
Figure 4.29	Two SAR images de-noised by the DPAD filter.....	79
Figure 4.30	Two SAR images de-noised by the SRAD filter.....	80
Figure 4.31	Two SAR images de-noised by the OSRAD filter.....	81

Figure 4.32	Two SAR images de-noised by the REDISRAD-EBF filter.....	82
Figure 4.33	Two SAR images de-noised by the REDISRAD-WDF filter. ....	83
Figure 4.34	Ultrasound images of carotid artery (of two different persons) in longitudinal section acquired by Sonix OP ultrasound scanner. ....	85
Figure 4.35	A 150×90 rectangular area at the lower-middle part of each ultrasound image. ....	86
Figure 4.36	Ultrasound images of carotid arteries of two different persons de-noised by the Lee filter .....	87
Figure 4.37	Ultrasound images of carotid arteries of two different persons de-noised by the Frost filter. ....	88
Figure 4.38	Ultrasound images of carotid arteries of two different persons de-noised by the homomorphic AD filter. ....	89
Figure 4.39	Ultrasound images of carotid arteries of two different persons de-noised by the DPAD filter. ....	90
Figure 4.40	Ultrasound images of carotid arteries of two different persons de-noised by the SRAD filter.....	91
Figure 4.41	Ultrasound images of carotid arteries of two different persons de-noised by the OSRAD filter.....	92
Figure 4.42	Ultrasound images of carotid arteries of two different persons de-noised by the REDISRAD-EBF filter.....	93
Figure 4.43	Ultrasound images of carotid arteries of two different persons de-noised by the REDISRAD-WDF filter. ....	94

## Chapter 1

# Introduction

Noise in digital images can be defined as random variation of brightness or color information. It reduces image quality and makes object recognition, segmentation, and classification difficult. The principal sources of noise in digital images arise during image acquisition and/or transmission. The quality of sensing elements and environmental conditions are the two key sources of noise in the image acquisition or digitization process. Image noise can also result from the interference in the channel used for transmission. According to the noise-model, noise created in image acquisition and/or transmission process can be grouped into two major categories— additive and multiplicative noise.

Noise reduction is an active research area of digital image processing. A good number of recent image de-noising research-works focus on the reduction of a special form of multiplicative noise named speckle. Speckle commonly occurs in SAR (Synthetic Aperture Radar), SAS (Synthetic Aperture Sonar) and ultrasound images. The ultimate goal of speckle reducing filters is to reduce the speckle noise level with minimal distortion of image details. But, this form of multiplicative noise is locally correlated which makes speckle reduction quite challenging. This thesis work proposes two filtering techniques for speckle reduction with a major focus on the preservation of image details.

In this chapter, we will present a brief introduction to the nature of speckle, various approaches to speckle reduction as well as the motivations and contributions of this thesis.

## 1.1 Speckle

A well known characteristic of coherent imaging is the presence of speckle. Speckle is simply a form of locally correlated multiplicative noise that inherently exists in and degrades the quality of various kinds of images including synthetic aperture radar (SAR), synthetic aperture sonar (SAS) and ultrasound images. Speckle normally occurs in these types of images in the image acquisition process. A distinctive property of speckle noise is local correlation. This local correlation property of speckle pattern makes it difficult to define a model of speckle.

The reason behind the local correlation in speckle pattern can be explained by the image acquisition processes of SAR, SAS and ultrasound images. For example, speckle noise in SAR system results from random fluctuations in the electromagnetic return signals (radio and microwave, specifically) from the underlying objects. Reflected signals returned from different objects have different fluctuation patterns. The speckles in a sub-region of the SAR image representing a specific object exhibit local correlation since they resulted from the same fluctuation pattern. Similarly, in case of SAS and ultrasound images, the local brightness of the speckle pattern, reflects the local echogenicity (the extent to which a structure/object gives rise to reflections of ultrasonic waves) of the underlying backscatter.

The goal of enhancement of speckled imaging is to reduce speckle without destroying significant edge details. Speckle filters first originated in the SAR community. Later, it became popular in SAS and ultrasound imaging. In each of these fields, speckle reduction is the pre-processing step of region-based detection, segmentation and classification.

## 1.2 Various approaches to speckle reduction

Standard additive noise filtering techniques are not effective in speckle reduction. It is already mentioned that pixels of speckled images are locally correlated. This property of speckled image limits the use of additive noise filters in SAR, SAS and ultrasound imaging.

Speckle reducing techniques can be grouped into two major categories— homomorphic and adaptive filtering. Homomorphic filters do not account for the local correlation property of speckled image. The key idea of homomorphic filtering is to transform multiplicative speckle noise into additive noise by applying some nonlinear memoryless operator and then applying standard additive noise filters for noise reduction. Then, an inverse nonlinear operator is applied to the de-noised image to produce the final output image. In the homomorphic filtering approach, the model of speckle noise is oversimplified since it doesn't account for an image transfer function involved in the image acquisition process (will be described in details in Chapter 2). This type of filters is inefficient in speckle reduction and quite outdated.

As the name implies, adaptive filters adapt with the change in underlying image sub-region and/or time. Unlike homomorphic filters, most of the successful adaptive filters account for the local correlation property of speckled images. Adaptive filters gather local statistics from image sub-regions and exploit this information to ensure better speckle reduction performance. Lee [1][2][3], Frost [4], Kuan [5] filters were the first few adaptive filters that showed appreciable speckle reducing performance. Later, anisotropic diffusion based adaptive filters like Speckle Reducing Anisotropic Diffusion (SRAD) [6] and various extensions to SRAD [7][8][9][10] showed significant improvement over the predecessors. Another family of speckle reducing adaptive filters uses wavelet techniques [11][13][14][15]. The main trend in wavelet based filters is to generate a set of wavelet coefficients corresponding to different scales of the input image and apply soft or hard thresholding on the coefficients to reduce the speckle. Then inverse wavelet transform is performed to produce the de-noised output image. Currently, anisotropic diffusion and wavelet based filtering techniques are the two most active research topics in the image de-noising research community.

### **1.3 Motivations**

Diffusion based filters like SRAD are more successful in speckle reduction compared to other speckle reducing filters. However, in highly speckled environment, performance of SRAD suffers both in terms of noise reduction and edge preservation. Sometimes, speckles are misinterpreted as edge details and at the same time, finer edges details are

misinterpreted as speckles. Such misinterpretations result in the preservation of speckles and smoothing of finer edge details. Moreover, edges in the SRAD output are not so sharp. Over-smoothing of edges also results in the dislocation/broadening of edge lines.

The main goal of this thesis work is to propose a speckle reducing technique to ensure a fine balance between edge preservation and noise reduction. Obviously, we want to denoise more. At the same time, we want to keep the finer edge details. We also expect to keep the sharpness of the preserved edges by ensuring appropriate level of smoothing. Moreover, edge dislocation/broadening can be avoided if we can manage to prevent over-smoothing of edges.

The performance of SRAD highly depends on a gradient/Laplacian operator based edge detector. According to the guidance of this edge detector, SRAD decides the level of smoothing required to be applied at various image sub-regions. Minimal smoothing should be applied on the image areas detected as edges since edge preservation is crucial. The level of smoothing should be adjusted based on the homogeneity of an image sub region. Maximal smoothing should be applied on an image sub-region which is completely homogeneous; edge preservation in such a sub-region is not an issue since we do not have edge details to preserve.

The main reason behind the shortcomings of SRAD is the inefficiency of the gradient and Laplacian based edge detector. It is well established that in highly speckled environment, gradient and Laplacian based methods are not efficient in terms of edge detection. As a result, the edge detector of SRAD often misinterprets speckles as edges and finer edge details as speckles which results in insufficient noise reduction and smoothing of edges, respectively. Moreover, SRAD uses a scaling factor to control the level of diffusion which is computed over an initially selected small homogenous region. If the initially selected region is not homogeneous enough, SRAD ends up producing a highly diffused image where the speckles as well as a great deal of finer edge details are removed due to over-smoothing.

## 1.4 Thesis contributions

To guide the gradient/Laplacian based edge detector of SRAD for the sake of better edge detection and de-noising in highly speckled environment, we propose the use of a ratio based edge detection technique. In speckled environment, ratio based edged detectors are known to perform better than the gradient and Laplacian based edge detectors. To incorporate ratio based edge detection guidance in the diffusion model of SRAD, we propose two different extensions. One of the proposed extensions calculates an edge sensitive boosting factor based on the edge information gathered by a ratio based edge detector. Then, this boosting factor is used to guide the edge decisions of the original edge detector of SRAD. The other proposed extension uses an edge sensitive global diffusion function which is defined by the edge information provided by an inherent ratio based edge detector. Instead of directly guiding the edge detector of SRAD, this global diffusion function is used to guide the original diffusion function of SRAD to ensure appropriate level of smoothing in different image sub-regions.

A hybrid scaling factor calculation strategy is also proposed to prevent over-smoothed or highly diffused image output. Our approach is to determine the homogeneity of the initially selected image-region and then, depending on how homogeneous the region is we select a scaling factor from two available options— the originally defined scaling factor of SRAD and a median based scaling factor (will be described in details in Chapter 3). Our work also promotes the use of a bigger window size for gathering local statistics from the input image. Local statistics gathered from a larger sample space should help to deal with the local correlation property of the speckled image.

## 1.5 Thesis outline

This thesis is divided into five chapters including this introductory discussion, Chapter 1. Chapter 2 presents a relevant background of existing speckle reduction methods as well as the ratio based edge detection techniques for speckled environment. In Chapter 3, the proposed methods are thoroughly described. Experimental results and relevant analysis are presented in Chapter 4. Chapter 5 offers the concluding remarks and future directions of the presented research work.

## Chapter 2

# Background

The main objectives of this chapter are to introduce the model of multiplicative speckle noise, and elaborate major previous works on speckle reduction and ratio-based edge detection. Section 2.1 presents the model of speckle noise. Section 2.2 summarizes common noise filtering techniques and previous significant works on speckle reduction. Relevant backgrounds of ratio-based edge detection techniques are presented at the beginning of Section 2.3. Finally, Section 2.3 ends with a comparison based discussion to validate the superiority of ratio-based edge detection methods over the gradient/Laplacian based techniques in speckled environment.

## 2.1 Model of speckle noise

It is a common practice to model additive noise by a Gaussian variable of zero mean and a given standard deviation. The model is given by

$$I_n = I_{org} + N_a, \quad (2.1)$$

where  $I_n$  is the observed signal corrupted by additive noise,  $I_{org}$  is the original signal without noise and  $N_a$  is the noise itself introduced by the acquisition and/or transmission processes.

We cannot express synthetic aperture radar (SAR) or ultrasound images by this simple Gaussian additive model. The acquisition processes of SAR and ultrasound images introduce a specific type of noise commonly known as speckle. Speckle is a locally correlated multiplicative noise that inherently exists in and degrades the quality of SAR

and ultrasound images. The local brightness of speckle pattern reflects the local echogenicity (the ability to bounce the sound as an echo) of the underlying backscatter. This local correlation makes it difficult to define a model for speckle.

A. K. Jain [16] considered the effects of both multiplicative and additive noise in his simple speckle model. According to his model, the speckled image can be expressed as

$$I_n = I_{org} N_m + N_a, \quad (2.2)$$

where  $N_m$  and  $N_a$  are the multiplicative and additive noise components, respectively. The effect of the additive noise component is considered to be very small compared to the multiplicative one. By neglecting the insignificant additive noise part, the speckle-model can be simplified to

$$I_n = I_{org} N_m. \quad (2.3)$$

In practice, the model is not as simple as equation (2.3). Frost [4] proposed a model for speckled SAR image where he took into account the spatial correlation introduced by the image acquisition process. He pointed out that there are several components of a SAR system like antenna and receiver which introduce a spatial correlation. Ultrasound image acquisition processes share similar characteristics though the components are different. Harger [17] represented such SAR system components by a linear spatially invariant transfer function. Using this transfer function, speckled image is modeled by

$$I_n(x, y) = [I_{org}(x, y) \cdot N_m(x, y)] * h(x, y), \quad (2.4)$$

where  $(x, y)$  is the spatial coordinate in 2D,  $h(x, y)$  is the system impulse response representing the transfer function and  $*$  denotes the convolution. A crucial goal of enhancement of speckled imaging is to generate an estimate of the original/ideal image  $I_{org}(x, y)$  from the corrupted observed image  $I_n(x, y)$ .

In the speckle model described above, the multiplicative noise component,  $N_m$ , is not enough to define the speckle. Rather we need both the transfer function and the

multiplicative noise component to model the speckle noise. In some research works on ultrasound imaging, it has been modeled as a Rayleigh distribution [18] [19] which is used in communication theory to model scattered signals that reach a receiver by multiple paths. If the components of a vector are given by independent normal distributions with zero means and equal variances, then the vector magnitude is characterized by a Rayleigh distribution. However, in practice, none of the proposed distributions effectively models speckle noise and as a result, filters based on such distributions cannot directly account for the local correlation property of speckle. In the absence of a proper model, the multiplicative noise component  $N_m(x, y)$  of Equation (2.4) is treated as stationary in most of the de-speckling filters. The local correlation property of speckled image is handled by exploiting local statistics based information. This strategy, employed by different filters, will be described elaborately in the next section.

## 2.2 Model of speckle noise

Linear spatially invariant filters [20][21] are primitive and inefficient in multiplicative speckle reduction. The non-stationarity of the speckled images is not accounted for in most of these techniques. These spatially invariant filters are more suitable for additive noise reduction. In terms of effectiveness, only two families of filters are relevant for speckle reduction: homomorphic and adaptive. Homomorphic filters use conventional additive noise filters augmented by a pre-processing stage. The adaptive filters exploit the local statistics to account for the non-stationarity of the speckled image. Based on noise reduction strategy, adaptive filters can be grouped into three major categories: minimum mean square error (MMSE) based non-iterative filters, anisotropic diffusion filters and wavelet based filters.

### 2.2.1 Homomorphic filters

Homomorphic filtering refers to a technique of preprocessing the observed image to transform non-additive noise into additive noise using a nonlinear memoryless operator. Then standard additive noise filtering is applied for noise reduction. The enhanced image is formed by applying the inverse nonlinear operator. For speckle-like multiplicative noise (i.e., assuming that the model of the noise is defined as Equation (2.3)), logarithmic

and exponential operators are required for forward and inverse transformations, respectively. Arsenault et al. [22] proposed such a homomorphic filter which applies the additive version of Lee [1] filtering (see Section 2.2.2) on the logarithm of the observed image.

A speckled image represents the observed data as being multiplicative noise operated on by a linear system [4] as defined by Equation (2.4). In such a case, a logarithmic operation will not properly separate the signal from the noise. As a result, homomorphic filters are not efficient in speckle reduction.

### 2.2.2 MMSE based non-iterative adaptive filters

Lee [1][2][3], Kuan [5], Frost [4] separately proposed local statistics based non-iterative adaptive speckle filters. These filters, originally tailored to SAR image de-noising, significantly exploited the local statistics of speckled images. They de-noise the input image in a single pass which makes them efficient in terms of execution time.

The basic approach followed by these filters was to derive the functional form of a minimum mean square error (MMSE) filter to estimate the original image  $I_{org}(x, y)$  from the observed image  $I(x, y)$  under the assumption of stationary image data. The non-stationary property that defines the local correlation of real SAR image is considered and handled exploiting some local statistics.

#### A. Lee Filter

Lee filter [1][2][3] is designed to eliminate speckle noise while preserving edges and point features in radar images. The filter produces the enhanced data by

$$\hat{I}_s = I_s \cdot W_s + \bar{I}_s \cdot (1 - W_s), \quad (2.5)$$

where  $\hat{I}_s$  is the filtered image intensity data,  $\bar{I}_s$  is the mean value of the intensity of the observed image within a filter window  $\eta_s$ ,  $W_s$  is a weighting function and  $s$  denotes the spatial coordinate, used as subscript. The weighting function is given by

$$W_s = 1 - \frac{C_u^2}{C_s^2}. \quad (2.6)$$

Here,  $C_s$  is the coefficient of variation and is the core component of Lee filter which accounts for the local statistics of input image data. The coefficient of variation  $C_s$  is defined as

$$C_s^2 = \left( \frac{1}{|\eta_s|} \right) \sum_{p \in \eta_s} (I_p - \bar{I}_s)^2 / (\bar{I}_s)^2, \quad (2.7)$$

where  $|\eta_s|$  is the size of filter window,  $p$  denotes a pixel in the window  $\eta_s$ ,  $I_p$  is the image intensity of pixel  $p$ .  $C_u$  is an image specific constant which is determined by

$$C_u^2 = \frac{\text{var}(z')}{(\bar{z}')^2}, \quad (2.8)$$

where  $\text{var}(z')$  and  $\bar{z}'$  are the intensity variance and mean over a small homogeneous area  $z$  of the image, respectively.

The coefficient of variation  $C_s$  plays the most crucial role in controlling the filter. If  $C_s \rightarrow C_u$ , then  $W_s \rightarrow 0$  and if  $C_s \gg C_u$ , then  $W_s \rightarrow 1$ . In the homogeneous regions, the value of  $C_s$  should take a lower value as the variance goes low there and ideally, we expect  $C_s \rightarrow C_u$  in a perfectly homogeneous region. So, in the homogeneous region the  $W_s$  is expected to take the value 0 which leads to a mean filter. On the contrary, in the heterogeneous regions the value of  $C_s$  should be higher than  $C_u$ . Ideally, it is expected that at the center of an edge  $C_s \gg C_u$  and  $W_s$  approaches unity. That makes the Lee filter to act like an identity filter. As a result, edges are kept in the heterogeneous regions.

## B. Kuan Filter

Kuan filter [5] operates in a similar way to the Lee filter. The enhanced data is produced by the Equation (2.5). Unlike Lee, Kuan defined the weighting function  $W_s$  by

$$W_s = \frac{1 - \frac{C_u^2}{C_s^2}}{1 + C_u^2}. \quad (2.9)$$

Both  $C_s$  and  $C_u$  are similarly defined as in Lee filter (see Equation (2.7) and (2.8)). However, in Kuan filter,  $C_u$  plays a more important role as  $W_s$  is more directly scaled by  $C_u$  in Equation (2.9). The local statistic  $C_s$  still plays the crucial role in controlling the filter though. In Kuan filter  $W_s$  never goes to 1, so the update Equation (2.2) always produces a weighted combination of averaging and all pass filtering. As a result, the Kuan filter is expected to perform well in terms of smoothing and to perform a bit poor in terms of edge preservation.

### C. Frost Filter

The Frost filter [4] uses an exponentially damped convolution kernel instead of the weighting function  $W_s$  of the Lee and Kuan filters. The kernel adapts to regions containing edges by exploiting local statistics. Though the approach to data enhancement is a bit different, the Frost filter uses the same local statistic,  $C_s$ , used in the Lee and Kuan filters. By using the exponential kernel, Frost eliminated the use of the constant scaling factor  $C_u$ . Frost filter produces the enhanced data by

$$\hat{I}_s = \sum_{p \in \eta_s} m_p I_p, \quad (2.10)$$

where

$$m_p = e^{-KC_s^2 d_{s,p}} / \sum_{p \in \eta_s} e^{-KC_s^2 d_{s,p}} \quad (2.11)$$

$$d_{s,p} = \sqrt{(i - i_p)^2 + (j - j_p)^2}, \quad (2.12)$$

where  $m_p$  is the weight assigned to pixel  $p$  in window  $\eta_s$ ,  $K$  is the damping constant,  $(i, j)$  are the grid coordinates of pixel  $s$ , and  $(i_p, j_p)$  are those of pixel  $p$ . The Euclidian distance between the pixels  $(i, j)$  and  $(i_p, j_p)$  is given by  $d_{s,p}$ .

The selection of the damping constant  $K$  is really important for Frost filter. Unfortunately, it is hardwired and need to be supplied by the user. The value of  $K$  is carefully chosen such that in homogeneous regions  $KC_s^2$  approaches zero, resulting a mean filter output. At the same time, on the edges  $KC_s^2$  goes so large that filtering is almost inhibited, yielding an all pass filter approximation.

### 2.2.3 Anisotropic diffusion based adaptive filters

#### A. Perona-Malik filter

Perona and Malik [23] used the concept of diffusion phenomena of physics to define a scale-space model for digital images. By using a gradient-sensitive diffusion coefficient they made the scale-space model space-variant and thereby, the ‘diffusion’ becomes anisotropic. The property of intra-region smoothing in preference to inter-region smoothing [23], made the Perona-Malik model an excellent additive noise filtering technique. However, as their model didn’t account for the local correlation property of speckled images, the Peron-Malik filter is not efficient in speckle reduction. It enhances speckle noise instead of reducing as it misinterprets speckles as edges. Though the Perona-Malik anisotropic diffusion filter is not a good choice for speckle reduction, it is the basic building block of modern diffusion based speckle reducing filters [6][9][7]. It is important to understand the working principal of Perona-Malik anisotropic diffusion filter before going to the details of modern improvements tailored to speckle reduction.

Perona and Malik defined a nonlinear partial differential equation (PDE) for smoothing image on a continuous domain. The PDE is given by

$$\begin{cases} \frac{\partial I}{\partial t} = \text{div}[c(|\nabla I|) \cdot \nabla I] \\ I(t = 0) = I_0, \end{cases} \quad (2.13)$$

where  $I_0$  is the initial image,  $t$  is the time,  $\nabla$  is the gradient operator,  $div$  is the divergence operator,  $||$  denotes the magnitude and  $c(\cdot)$  is the diffusion coefficient function. A discrete form of Equation (2.11) can be written as

$$I_s^{t+\Delta t} = I_s^t + \frac{\Delta t}{|\eta_s|} \sum_{p \in \eta_s} c(|\nabla I_{s,p}^t|) \nabla I_{s,p}^t, \quad (2.14)$$

where  $I_s^t$  is the discretely sampled image,  $s$  denotes the pixel position in 2D grid,  $\Delta t$  is the time step size,  $|\eta_s|$  is the size of the window  $\eta_s$  surrounding the pixel  $s$  and  $\nabla I_{s,p}^t$  is given by

$$\nabla I_{s,p}^t = I_p^t - I_s^t, \quad \forall p \in \eta_s. \quad (2.15)$$

The authors proposed two alternative diffusion coefficients

$$c(x) = e^{-\left(\frac{x}{k}\right)^2} \quad (2.16)$$

and

$$c(x) = \frac{1}{1 + \left(\frac{x}{k}\right)^2}, \quad (2.17)$$

where the edge magnitude parameter,  $k$ , is a constant. In fact, Equation (2.17) is the Taylor series approximation of Equation (2.16).

In the Perona-Malik anisotropic diffusion method, the gradient magnitude is used to detect any edge which is a step discontinuity in the intensity on its continuous form. The constant  $k$  of the diffusion function acts as the edge threshold. If  $|\nabla I| \gg k$ , then  $c(|\nabla I|) \rightarrow 0$ , and we have an all-pass filter. If  $|\nabla I| \ll k$ , then  $c(|\nabla I|) \rightarrow 1$ , and Perona-Malik filter acts like a Gaussian filter. The value of  $c$  varies within the closed interval  $[0,1]$  with the magnitude of the gradient. That makes the filter anisotropic, i.e., space-variant.

For images corrupted by additive noise, a single predefined threshold and gradient based edge detection is quite effective. The Perona-Malik filter excels in such a scenario. However, for a speckled image, the diffusion function of Perona-Malik filter detects the speckle noise as an edge if the corresponding gradient value happens to be greater than the edge magnitude parameter  $k$ . The problem lies in the idea of using a predefined

constant threshold. For a given speckled image, it is impossible to define a single threshold of gradient magnitude. Due to the local correlation property of speckled image, we need multiple thresholds for multiple sub-regions to compare against the gradient values. Moreover, the use of the gradient magnitude for edge detection in speckled images is not effective [24].

## B. Speckle reducing anisotropic diffusion filter

Yu and Acton [6] modified the anisotropic diffusion filter of Perona and Malik [23] using the local statistics based coefficient of variation concept of Lee [1], Kuan [5] and Frost [4]. They proposed Speckle Reducing Anisotropic Diffusion, SRAD, which uses both gradient magnitude and Laplacian for edge detection unlike Perona-Malik filter.

As we have said earlier, SRAD is highly inspired by the anisotropic diffusion filter of Perona and Malik. The update function of SRAD has a great resemblance with Equation (2.14). The discrete form of the update function SRAD is given by

$$I_{i,j}^{t+\Delta t} = I_{i,j}^t + \frac{\Delta t}{|\eta_s|} \text{div}[c(C_{i,j}^t) \nabla I_{i,j}^t], \quad (2.18)$$

where  $c(\cdot)$  is the diffusion function of anisotropic diffusion model.  $C_{i,j}^t$  is the local statistics based coefficient of variation in time  $t$ . To create a fusion of PDE based classical anisotropic diffusion with the local statistics based Lee and Kuan filters, Yu and Acton used the coefficient of variation parameter as the edge detector instead of gradient and then the diffusion function has been defined in terms of the coefficient of variation.

Yu and Acton provided a discretized version of the coefficient of variation which is applicable to the classical PDE evolution. Considering a window of four neighboring pixels, they came up with the following discretized version of coefficient of variation.

$$(C_{i,j}^t)^2 = \frac{\frac{1}{2} |\nabla I_{i,j}^t|^2 - \frac{1}{4^2} (\nabla^2 I_{i,j}^t)^2}{\left(I_{i,j}^t + \frac{1}{4} \nabla^2 I_{i,j}^t\right)^2}, \quad (2.19)$$

where  $(i, j)$  represents the position in 2D image matrix,  $C_{i,j}^t$  is the coefficient of variation at  $(i, j)$  in time  $t$ ,  $\nabla$  denotes the gradient and  $\nabla^2$  denotes the Laplacian. This coefficient of variation is the inherent edge detector of SRAD which is apparently a combination of the gradient magnitude and Laplacian. High relative gradient magnitude and low relative Laplacian tend to indicate an edge. At the center of the edge, the relative value of  $C_{i,j}^t$  is maximum as the Laplacian goes to zero and gradient reaches its peak. Assuming that the image intensity function has no zero point over its support, Yu and Acton defined an Instantaneous Coefficient of Variation, ICOV, which is given by

$$q_{i,j}^t = \frac{\sqrt{\frac{1}{2} \left( \frac{|\nabla I_{i,j}^t|}{I_{i,j}} \right)^2 - \frac{1}{4^2} \left( \frac{\nabla^2 I_{i,j}^t}{I_{i,j}} \right)^2}}{\left( 1 + \frac{1}{4} \left( \frac{\nabla^2 I_{i,j}^t}{I_{i,j}} \right)^2 \right)}, \quad (2.20)$$

where  $q_{i,j}^t$  and  $I_{i,j}^t$  are the ICOV and image intensity of pixel  $(i, j)$  in 2D image grid in time  $t$ , respectively. Finally, the update function of SRAD takes the form

$$I_{i,j}^{t+\Delta t} = I_{i,j}^t + \frac{\Delta t}{|\eta_s|} \text{div}[c(q_{i,j}^t) \nabla I_{i,j}^t], \quad (2.21)$$

Being inspired by Lee [1] and Kuan [5], Yu and Acton used a scaling factor while defining the diffusion function. The diffusion function,  $c(q_{i,j}^t)$ , is given by

$$c(q_{i,j}^t) = \frac{1}{1 + \frac{(q_{i,j}^t)^2 - (q_0^t)^2}{(q_0^t)^2 [1 + (q_0^t)^2]}}, \quad (2.22)$$

where  $q_0^t$  is the speckle scaling factor.  $q_0^t$  is equivalent to the constant term  $C_u$  of Lee and Kuan filters (see Section 2.2.2) and given by the Equation (2.8).

The ICOV exhibits high values at edges or on high-contrast features and produces low values in homogeneous regions. As a result, according to Equation (2.22),  $c(q_{i,j}^t)$  takes small values at edges and larger values at homogeneous regions. That ensures less smoothing on edge or detail containing regions and more smoothing on homogeneous

areas. The diffusion becomes isotropic when  $q_{i,j}^t \approx q_0^t$ . In a sense, the speckle scale function,  $q_0^t$ , controls the amount of smoothing applied to the image by SRAD.

SRAD avoids the use of a threshold on the norm of gradient in the diffusion function. This independent threshold parameter of Perona-Malik's diffusion has been replaced by an estimation of the standard deviation of the noise ( $q_0^t$ ), at each iteration. This scheme introduces less dependence on the norm of the gradient which can vary across a speckled image. At the same time, SRAD benefits by the natural decrease of diffusion as the estimated standard deviation of the noise decreases with time which leads to a convergence without smoothing out interesting features of the image.

### C. Deconvolutional speckle reducing anisotropic diffusion

Acton introduced the Deconvolutional Speckle Reducing Anisotropic Diffusion [8], DeSpeRADO, to compensate the detail distortion effect of SRAD. The PDE of DeSpeRADO has two main components: the diffusion component and the deconvolution component. The diffusion component is nothing but the earlier SRAD which takes care of the speckle reduction by space-variant smoothing. The deconvolution component reverses the blurring that occurs due to the transfer/point-spread function of ultrasound image acquisition (see Equation (2.4)) and balances the smoothing effect of the diffusion component by discouraging blurring of image features. Acton proposed that the point-spread function need to be deconvoluted as a two dimensional Gaussian function.

### D. Detail preserving anisotropic diffusion

Aja-Fernández et al. [9] proposed modifications to the coefficient of variation and scaling factor calculation strategy of SRAD. They called their proposed filter Detail Preserving Anisotropic Diffusion, DPAD. Aja-Fernández et al. pointed out that the coefficient of variation, CV, of SRAD (see equation (2.19)) can be written as

$$C_{i,j}^t = \sqrt{\frac{\frac{1}{|\eta_{i,j}|} \sum_{p \in \eta_{i,j}} (I_p^t - \bar{I}_{i,j}^t)^2}{(\bar{I}_{i,j}^t)^2}}, \quad (2.23)$$

where  $|\eta_{i,j}|$  is the size of the window  $\eta_{i,j}$  surrounding the pixel at location  $(i, j)$ ,  $p$  is any pixel in the window,  $I_p^t$  is the intensity of pixel  $p$  in time  $t$  and  $\bar{I}_{i,j}^t$  is the mean intensity value of the pixels in the window in time  $t$ . They proposed a  $3 \times 3$  window where the pixel  $(i, j)$  lies at the center being surrounded by eight neighboring pixels. Then the unbiased version of the CV is given by

$$(C_{i,j}^t)_U = \sqrt{\frac{\frac{1}{|\eta_{i,j}|_U - 1} \sum_{p \in (\eta_{i,j})_U} (I_p^t - \bar{I}_{i,j}^t)^2}{(\bar{I}_{i,j}^t)^2}}, \quad (2.24)$$

where  $(\eta_{i,j})_U$  is the window of size  $3 \times 3$  and  $(C_{i,j}^t)_U$  is the unbiased CV.

In lieu of the original speckle scaling factor calculation strategy of SRAD, Aja-Fernández et al. proposed some alternatives. First, they propose to take the minimum value of all CVs in the input image as the value of scaling factor  $q_0$ , i.e.,

$$q_0^2 = \text{Min}_{i,j}(C_{i,j}^2), \quad (2.25)$$

where  $C_{i,j}$  is the coefficient of variation of pixel  $(i, j)$  in 2D image grid. But the presence of outliers makes the minimum to be biased towards zero [25]. So, the minimum should be considered as the lower bound for  $q_0$ . Another alternative estimator of the speckle scaling factor is the average

$$q_0^2 = \frac{1}{N} \sum_{i,j} C_{i,j}^2, \quad (2.26)$$

where  $N$  is the total number of pixels in the image. Then Aja-Fernández et al. marked it as an over-estimator of  $q_0$  and claimed that it should be the upper bound of the speckle scaling factor. Finally, due to the robustness to outliers, they proposed the median of CVs as the speckle scaling factor. That is,

$$q_0^2 = \text{Median}_{i,j}(C_{i,j}^2). \quad (2.27)$$

In practice, the median based estimation of the scaling factor helps to preserve edge details.

### E. Oriented SRAD

Krissian et al. [7] extended the diffusion mechanism of SRAD to a matrix anisotropic diffusion. They added a non-scalar component to the SRAD filter to perform directional filtering of speckled image. First, they presented the matrix version of SRAD PDE. The 2D version of the equation is given by

$$\begin{aligned} \frac{\partial I}{\partial t} &= \text{div}(c(q)\nabla I) \\ &= \text{div}\left(\begin{pmatrix} c(q) & 0 \\ 0 & c(q) \end{pmatrix} \nabla I\right), \end{aligned} \quad (2.28)$$

where  $c(q)$  is the diffusion function of SRAD. As the diffusion matrix of SRAD is a scalar, it can be written as  $D = c(q)I_m$  where  $I_m$  is the identity matrix. The idea of Krissian et al. was to change the scalar diffusion matrix to a non-scalar one so that diffusion can be performed in the edge direction. To do so, they proposed a new diffusion matrix

$$D = \begin{pmatrix} c(q) & 0 \\ 0 & c_{tang} \end{pmatrix}, \quad (2.29)$$

where  $c_{tang}$  is a constant weighting the diffusion applied along the edge direction. They named their proposed filter-- Oriented Speckle Reducing Anisotropic Diffusion, OSRAD.

### E. More anisotropic diffusion based speckle filters

Kim et al. [26] proposed a speckle reducing anisotropic diffusion filter for ultrasound images based on direction of gradients. In the case of edge pixels, the weight of diffusion is selected adaptively according to the direction of gradient. For the non-edge pixels, diffusion is performed in eight directions (north, south, east, west, north-left, north-right, south-left, south-right).

R. Srivastava et al [27] proposed a diffusion filter based on the Schrödinger wave equation. Being inspired by the free particle Schrodinger wave equation [28], they realized the diffusion process as a complex diffusion with an imaginary diffusion coefficient. Their proposed filter operates on log-compressed images.

A diffusion filter based on the separability of images has been introduced by S. Liu et al. [29]. They modified the diffusion coefficient of SRAD by separability to enhance the precision of detecting edges and control the amount of smoothing.

An overview of the related diffusion based works makes it clear that most of the anisotropic diffusion based speckle filters are based on the original SRAD filter of Yu and Acton [6]. The deconvolutional version (DeSpeRADO) [8] of Acton was not so successful due to the simplistic assumption of point-spread function (PSF) based on Gaussian model. Extensive calculations due to deconvolution also limit its application in real data. Aja-Fernández et al. [9] specifically focused on detail-preservation in their DPAD work. Their contributions were an unbiased ICOV and a modified scaling factor calculation strategy. Though DPAD showed some improvement in detail preservation, its de-noising performance is questionable. Some extensions of SRAD exploited the direction of gradient. The OSRAD by Krissian et al. [7] is a prominent inclusion in this category. It shows impressive de-noising performance in highly speckled environment. However, OSRAD has a tendency to over-smooth which limits its application in SAR image de-noising where preserving finer edge details is crucial. Very recent works like the use of Schrödinger wave equation [27] in the diffusion model seems promising and may lead to a new research path.

#### **2.2.4 Wavelet based adaptive filters**

The fundamental idea of wavelet analysis is to analyze a signal in different scales. Wavelets are functions that satisfy certain mathematical requirements and are used to represent data or other functions [30]. The basic idea is same as the Fourier transform [31]— approximation by superposition of functions. In Fourier transform, we superpose sine and cosine functions to represent other signals. Though wavelet technique shares the

basic principal, it varies in two important aspects. First, it doesn't use sine and cosine functions for superposing. Sine and cosine functions are non-local and they stretch out to infinity. As a result, they do a poor job at approximating sharp spikes or edges [30]. Wavelet analysis uses some functions that are contained neatly in finite-domain like Daubechies' family of wavelets, Coiflets wavelets, M-band wavelets, etc. [32]. Second, the wavelet technique processes data at different scales or resolutions [30]. If we analyze a signal at higher scale, we notice gross features. If we analyze it at lower scale, we get the fine or detailed features. Wavelet based techniques try to make the best out of both of the scenarios.

Wavelet analysis of an input signal (digital image, in our case) returns multiple sets of weights or wavelet coefficients each representing a specific scale or resolution. The most popular technique employed in wavelet based speckle filters is the thresholding of these wavelet coefficients and then performing inverse wavelet transform. Thresholding can be soft or hard. Soft thresholding of wavelet coefficients is also known as wavelet shrinkage. Guo et al. [13] proposed a wavelet based filter which proposes both soft and hard thresholding, separately. They used length-4 Daubechies' wavelet and performed the wavelet transformation for five different levels of resolutions. Then they performed thresholding only on the first level of wavelet coefficients which contains most of the speckles. Their simple hard thresholding approach is given by

$$\hat{w} = \begin{cases} w, & |w| > t \\ 0, & otherwise, \end{cases} \quad (2.30)$$

where  $w$  is the original wavelet coefficient,  $\hat{w}$  is the output wavelet coefficient and  $t$  is the threshold. As an alternative, they also proposed the similar kind of soft thresholding adopted by Donoho et al. [11]. Donoho's soft thresholding can be presented as the following weight adjusting equation:

$$\hat{w} = \text{sign}(w)(|w| - t), \quad (2.31)$$

where the function  $\text{sign}$  returns the sign of the argument  $w$  and  $t$  is the threshold.

Hao et al. [15] introduced a multiscale nonlinear thresholding method for speckle reduction of ultrasound images. They used adaptive weighted median filtering, AWMF, [33][34] as the pre-processing stage. The input image  $\hat{t}$  is decomposed into two images  $\hat{t}_1$  and  $\hat{t}_2$ .  $\hat{t}_1$  is the output of the AWMF and  $\hat{t}_2$  is obtained by subtracting  $\hat{t}_1$  from  $\hat{t}$ . The  $\hat{t}_1$  part contains most of the signal and  $\hat{t}_2$  contains most of the noise. These two images are decomposed into different level of resolutions  $\hat{t}_{1j}, \hat{t}_{2j}$  ( $j = 1, 2, \dots, k$ ) by a two-dimensional wavelet transform. Hao et. al. proposed a modified version of Donho's soft-thresholding to generate the output wavelet coefficients  $W_{\hat{t}_{1j}}$  and  $W_{\hat{t}_{2j}}$ . After soft thresholding, coefficients of the two parts are inversely transformed to space domain and then, summed up to produce the output image. Mellet et al. [35] proposed a similar type of wavelet-coefficient thresholding based filters.

Rabbani et al. [14] proposed several multiscale nonlinear thresholding methods for ultrasound speckle suppression. The wavelet coefficients of the logarithm of image were modeled as the sum of a noise-free component plus an independent noise. Assuming that the noise-free component has some local mixture distribution (MD), and the noise is either Gaussian or Rayleigh, they derived the minimum mean squared error (MMSE) and the averaged maximum estimators for noise reduction. The authors used Gaussian and Laplacian MD for each noise-free wavelet coefficient to characterize their heavy-tailed property.

Bhuiyan et al. [36] proposed a spatially adaptive wavelet-based method in order to reduce the speckle noise from ultrasound images. A spatially adaptive threshold was introduced for denoising the wavelet coefficients of log-transformed ultrasound images. The threshold was obtained from a Bayesian maximum a posteriori estimator that was developed using a symmetric normal inverse Gaussian probability density function (PDF).

The main trend in wavelet based speckle filtering is to generate different sets of wavelet coefficients corresponding to different level of resolutions and then thresholding these coefficients to reduce the speckle. It is noticeable that this approach does not account for

the local correlation property of multiplicative speckle noise. As a result, anisotropic diffusion based speckle filters are more successful compared to the wavelet based ones.

## 2.3 Edge detection in speckled image

### 2.3.1 Ratio-based edge detection methods

Ratio-based edge detectors estimate the edge strength on any pixel of interest in an image by calculating the *ratio* between neighboring pixel values. The estimated ratio may be improved by calculating the averages of pixel values in two adjacent and non-overlapping regions, selected on opposite sides of pixel of interest. These two regions,  $P$  and  $Q$ , may be selected from any orientation around the pixel of interest.

The idea of a ratio-based edge detection method, named Ratio of Averages, RoA, was introduced by Bovik [37]. Zaman and Moloney modified Bovik's RoA and proposed Modified Ratio of Averages, MRoA, [38][39] method. In MRoA, a window of size  $w \times w$  centered on the pixel of interest is split into two adjacent and non-overlapping neighboring regions for each of the four usual direction (horizontal, vertical, left-slanted and right-slanted) as shown in Figure 2.1. The edge strength for a particular pixel for  $i^{th}$  pair of regions is defined as

$$R_i = \text{Min} \left( \frac{P_i}{Q_i}, \frac{Q_i}{P_i} \right), i = 1, 2, 3, 4, \quad (2.32)$$

where  $P_i$  and  $Q_i$  are the averages of the pixel values in  $i^{th}$  pair of regions on opposite sides of the current pixel and  $i$  represents the orientation. The overall edge strength  $R$  is obtained by

$$R = \text{Min}(R_1, R_2, R_3, R_4). \quad (2.33)$$

The MRoA determines edge pixel location if  $R < R_t$ , where  $R_t$  is a predefined ratio threshold.

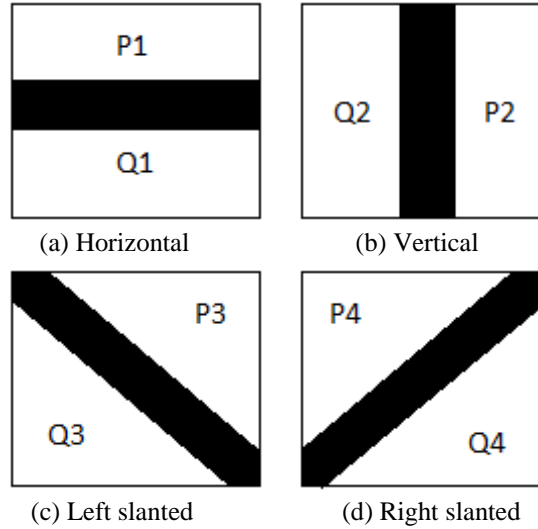


**Figure 2.1** Four usual directions (black bars) to partition a  $W \times W$  window into two adjacent and non-overlapping regions  $P_i$  and  $Q_i$  for  $i = 1, 2, 3, 4$  representing horizontal, vertical, left slanted and right slanted directions, respectively.

MROA has been extended to Ratio and Gradient of Averages, RGoA, by combining gradient edge information with ratio measure [38][39]. The gradient magnitude is computed as follows:

$$G_i = |P_i - Q_i|, i = 1, 2, 3, 4 \quad (2.34)$$

with

$$G = \text{Max}(G_1, G_2, G_3, G_4), \quad (2.35)$$

where the subscript  $i$  denotes orientation. For RGoA, the ratio threshold  $R_t$  and a gradient threshold  $G_t$  are predefined for ratio magnitude  $R$  and gradient magnitude  $G$ , respectively. Edges are detected if either  $R \leq R_t$  or  $G \geq G_t$ . Bai et al. [40] modified RGoA by changing the edge detection condition to  $R \leq R_t$  and  $G \geq G_t$ . They also proposed a scheme for dynamic threshold calculation.

Moloney et al. [41] proposed the Maximum Strength Edge Pruned Ratio of Averages, MSP-RoA, another ratio-based edge detection method. Unlike previous methods, it takes into account the edge direction while deciding whether a pixel is an edge-pixel or not. A

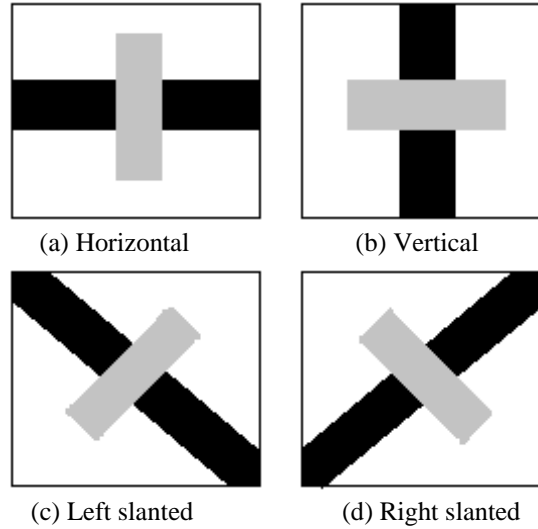


**Figure 2.2** Pruning directions (gray bars) perpendicular to four window-partitioning directions (black bars).

vector  $(R, O)$  is calculated at a pixel of interest which stores both the estimated minimal ratio strength  $R$  and an orientation  $O$  of a possible edge at the pixel. The ratio strength  $R$  is calculated by MRoA method. The direction corresponding to the minimum  $R_i$  value is noted as  $O$ . The pixels which satisfy the condition  $R \leq R_t$ , where  $R_t$  is a predefined ratio threshold, are considered as candidate edge pixels. Then MSP-RoA starts a pruning process which runs on a small window along the direction perpendicular to the minimal ratio producing direction as shown in Figure 2.2. If the ratio value of the candidate pixel is the smallest one in the pruning window, the pixel is accepted as edge. Otherwise, it is rejected and pruning process continues with other candidate edge pixels. This method produces thinner edges compared to the other methods since false-positive edge candidates near edges are rejected by pruning.

The choice of window size is crucial for all ratio-based edge detection methods. A larger window enables better edge detection in presence of higher speckles whereas a smaller window avoids the risk of missing fine edge details. So, the window size should be carefully chosen.

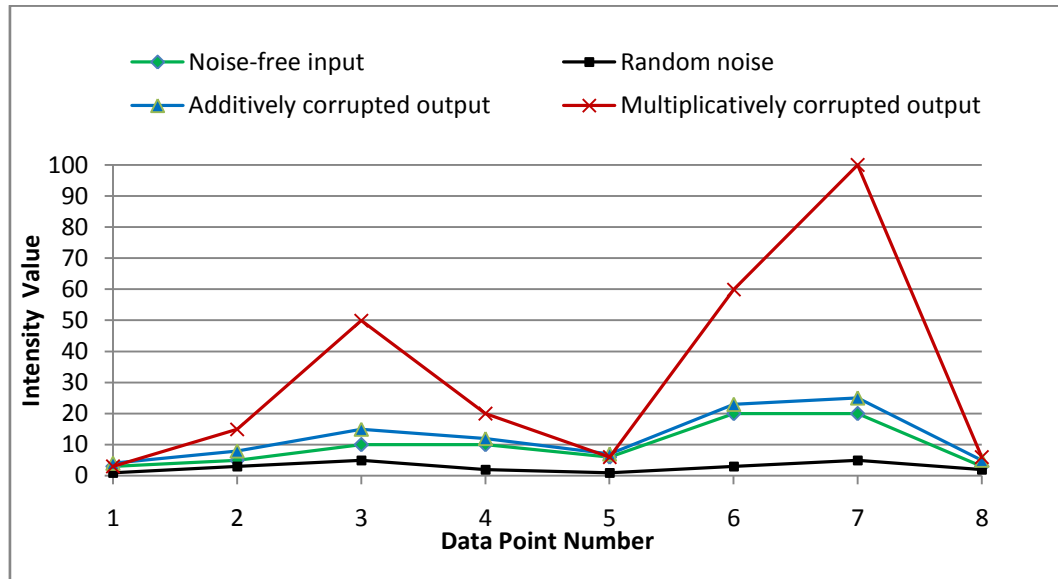


**Figure 2.3** The trend of the additive noise output (blue line) follows the random noise (black line) and less dependent on input intensity (green line). On the other hand, the multiplicative noise output (red line) is highly dependent on the underlying input intensity values.

### 2.3.2 Gradient/Laplacian-based Vs ratio-based edge detection

Detecting intensity changes across the object boundaries in speckled images is a highly complicated process due to the nature of speckle. If a conventional gradient or Laplacian based edge detector is used, the edge detector will respond to the artifacts as well as objects [37]. As the speckle intensity is multiplicative with underlying image intensity, the statistics of the image gradient is bound to vary with the underlying intensity. Figure 2.3 provides a simple demonstration of how the multiplicatively corrupted output varies with the underlying input intensity. For a simplistic one-dimensional demonstration, a random input data-set (intensity values)  $\{3,5,10,10,6,20,20,3\}$  has been corrupted by a set of random noise values  $\{1,3,5,2,1,3,5,2\}$ , both additively and multiplicatively. It is readily visible that the multiplicative noise output (red line) is highly dependent on the input intensity values which is not true for the additive noise output (blue line). Gradient and Laplacian based edge detectors perform poorly in this type of scenario [42].

Gradient based edge detectors use a gradient threshold to determine edges. Laplacian based edge detectors also use a similar type of threshold to filter out spurious zero

crossings [43]. As the variance of the speckle gradient increases with the underlying intensity, in regions of higher intensity a greater number of spurious edges (like the edge from data point 6 to 7, in Figure 2.3) will be found unless the detector threshold is also varied in some manner. Bovik [37] showed that even if the threshold is made to vary adaptively, there is no guarantee that the resulting adaptive edge detector will perform adequately near the edges.

Generally, image gradient magnitude is approximated using the absolute *difference* between intensity of two image regions. But, ratio-based estimations are calculated based on the ratio of average intensities of two image regions. As a result, the statistics of edge-magnitude estimate do not depend on the underlying local intensity [12]. This property of ratio-based edge detection techniques made them more suitable for locally correlated speckled images. Ratio-based edge detection avoids the use of an un-acceptable static gradient-threshold and at the same time, it manages to avoid a complicated and uncertain adaptive threshold-adjusting approach which produces different thresholds for different image regions.

To demonstrate the superiority of ratio based edge detection methods over the gradient based edge detectors, we present two distinct edge maps of the same speckled version of Lena (speckled by multiplicative Gaussian noise with standard deviation 0.50 and mean

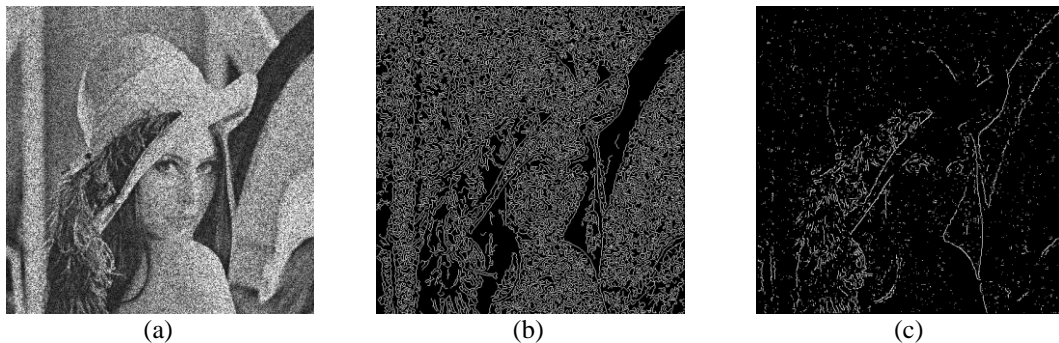


**Figure 2.4** Edge maps of the speckled version of the standard image Lena generated by gradient and ratio-based methods. (a) The standard grayscale image Lena ( $512 \times 512$ ) speckled by multiplicative Gaussian noise with standard deviation 0.5 and mean 0, (b) Edge map generated by gradient based optimal Canny edge detector with dynamic threshold and standard deviation 1 for inherent Gaussian filtering, (c) Edge map generated by ratio-based edge detector MSP-RoA with a  $5 \times 5$  window for ratio calculation and pruning window of size  $2 \times 1$ .

0) generated by the optimal Canny edge detector [44] (which is gradient based) and ratio-based MSP-RoA edge detector [41]. Figure 2.4(a) shows the speckled input image.

Figure 2.4(b) and Figure 2.4(c) show the edge maps generated by Canny edge detector and MSP-RoA edge detector, respectively. The gradient based Canny edge detector misinterpreted the speckles as edges and as a result, the generated edge map hardly provides any significant edge information. On the contrary, MSP-RoA generated a considerably superior edge map which definitely conveys more edge information than the edge map of Canny edge detector.

## Chapter 3

# Methodology

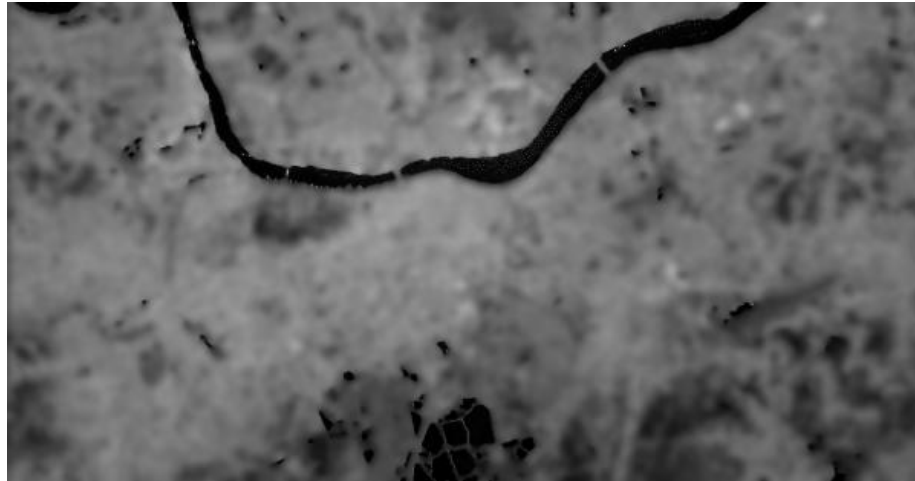
Instantaneous coefficient of variation, ICOV, is the core component of SRAD [6]. ICOV is supposed to ensure on appropriate amount of smoothing in different sub-regions of the input image to establish a nice balance between edge preservation and de-noising. This inherent edge detector of SRAD is a combination of gradient and Laplacian operators (see Equation (2.18)). Since gradient and Laplacian based methods are not efficient in terms of edge detection for speckled imagery [37], edge detection performance of ICOV-centric edge detector degrades in presence of higher level of speckles. As a result, edge preservation and de-noising performances of SRAD are not up to the mark in highly speckled environment. Moreover, SRAD produces dislocated edges due to over-smoothing of object boundaries. This undesirable property of SRAD was described by Yu and Acton [6] as ‘broadening of edges’.

Figure 3.1 shows an input SAR image and corresponding de-noised output produced by SRAD. The de-noised output image demonstrates two major drawbacks of SRAD—(1) the edges are un-sharp and dislocated/broadened in most of the sub-regions of the de-noised image and (2) most of the finer edge details have been entirely lost due to over-smoothing.

To overcome these weaknesses, we introduce two different extensions to SRAD that utilize global guidance of ratio-based edge detection. Both extensions share a common prefix name— Ratio-based Edge Detection Inspired Speckle Reducing Anisotropic Diffusion, REDISRAD. One of the two proposed extensions uses an edge-sensitive boosting factor to guide the original ICOV and hence named as REDISRAD-EBF



(a)



(b)

**Figure 3.1** A pictorial demonstration of the major weaknesses of SRAD. (a) A SAR image of the city of Calcutta, India (courtesy of NASA JPL) (b) De-noised image after 300 iterations of SRAD. Most of the edges are un-sharp and at the same time, dislocated or broadened. A great deal of finer edge details has been lost completely due to over-smoothing.

(REDISRAD with Edge-sensitive Boosting Factor). The other extension, REDISRAD-WDF (REDISRAD with Weighted Diffusion Function), defines a weighted diffusion function to propagate global edge-sensitive guidance. We also propose modified schemes for scaling factor selection and the computation of ICOV. These schemes are shared by both proposed extensions.

### 3.1 Guidance of ratio-based edge detection

Though ratio-based edge detection techniques are superior to the gradient and Laplacian based edge detectors in speckled environment, replacing the original ICOV coefficient by a ratio-based edge scoring function is not a good idea for two reasons— (1) ICOV coefficient is not just a traditional edge detector; it also accounts for the local correlation property of speckled image [6] and (2) anisotropic diffusion is an iterative process and calculating the ratio-based edge detection related terms for the entire image at each iteration will be computationally expensive. In our proposed extensions, we keep the ICOV coefficient and incorporate extra edge-sensitive guidance using the ratio-based edge detection technique to guide the diffusion process.

#### 3.1.1 Generating ratio and direction matrices

The ratio matrix generation stage is a common process adopted by most of the ratio-based edge detection methods. Unlike the conventional ratio-based methods, we smooth the speckled input image by a Gaussian kernel of size  $W_G \times W_G$  to improve the edge detection performance in the presence of higher level of speckle noise. Then, the ratio matrix is computed over the Gaussian-smoothed image. The ratio matrix contains the minimal edge ratio or edge-strength value of each pixel of the Gaussian-smoothed input image. The edge strengths of the image pixels are calculated in a similar fashion described in Section 2.3.1, except we use a slightly modified equation given by

$$R_i = \begin{cases} 1, & \text{if } P_i = 0 \text{ and } Q_i = 0 \\ \text{Min}\left(\frac{P_i}{Q_i + \epsilon}, \frac{Q_i}{P_i + \epsilon}\right), & \text{otherwise,} \end{cases} \quad (3.1)$$

where  $R_i$  is the edge strength for direction  $i$ ,  $P_i$  and  $Q_i$  are the two non-overlapping regions described in Section 2.3.1 and  $\epsilon$  is a small constant to avoid division by zero. The conventional edge strength calculation scheme (see Equation (2.31)) is modified by assigning the maximal ratio value of 1 to  $R_i$  when the average intensities of both  $P_i$  and  $Q_i$  happen to be zero. The conventional ratio-based edge detection methods assign the value 0 in such a case.

The smaller the value of  $R_i$ , the higher the edge strength of the pixel of interest along the direction  $i$ .  $R_i$  is guaranteed to take a value from the closed interval  $[0,1]$ . After calculating  $R_i$  values for all four directions, the overall minimum edge strength  $R$  is obtained by Equation (2.33).

Like MSP-RoA (see Section 2.3.1) we also keep track of the direction  $i$  that produced the minimal ratio for the pixel of interest. At the end of this process, we have a pair of 2D matrices, *Ratio\_Matrix* and *Dir*, containing the overall ratio strength and the direction producing the minimal ratio-value, respectively. While computing the ratio matrix for each pixel, we keep track of the maximal ratio value  $RMax_{global}$  and minimal ratio value  $RMin_{global}$  for the entire image matrix. At the end, by applying the technique of Bai et al. (see Section 2.3.1) the ratio threshold  $T_R$  is computed as

$$T_R = \frac{RMax_{global} + RMin_{global}}{2}. \quad (3.2)$$

### 3.1.2 Acquisition of global edge information

Both REDISRAD-EBF and REDISRAD-WDF acquire global edge information through a pruning process which is directly influenced by MSP-RoA (see Section 2.3.1). The pruning starts by comparing the ratio strength of each pixel against the ratio threshold  $T_R$ . A pixel is considered as a candidate edge pixel if

$$Ratio\_Matrix_{i,j} < T_R, \quad (3.3)$$

where  $Ratio\_Matrix_{i,j}$  is the  $(i,j)^{th}$  entry of the ratio matrix representing ratio strength of pixel  $(i,j)$ . For each candidate edge pixel, the direction producing the minimal ratio is retrieved from the direction matrix *Dir*. A small vector sub-window of size  $d \times 1$  centered on the edge candidate and perpendicular to the direction  $Dir_{i,j}$  is taken as the pruning window.  $d$  is a small positive number greater than 1 (e.g., 2 or 3).

Until this point, REDISRAD-EBF and REDISRAD-WDF operate exactly in the same fashion. After selecting the pruning window, they employ different approaches to gather

global edge information. Strategies employed by REDISRAD-EBF and REDISRAD-WDF are presented in the following Subsections 3.1.2.1 and 3.1.2.2, respectively.

### 3.1.2.1 Edge-sensitive boosting factor of REDISRAD-EBF

The ratio strength of candidate edge pixel  $(i, j)$  (given by  $Ratio\_Matrix_{i,j}$ ) is compared with the ratio strengths of other pixels in the pruning window. If  $Ratio\_Matrix_{i,j}$  is not the minimum in the pruning window, it is rejected or pruned from the edge candidate list and the value 1 is assigned to the  $(i, j)^{th}$  entry of a 2D matrix,  $Pruning\_Decision$ . If  $Ratio\_Matrix_{i,j}$  is the minimum ratio-strength in the pruning window, pixel  $(i, j)$  is accepted as an edge pixel and the  $(i, j)^{th}$  entry of  $Pruning\_Decision$  is set to 0. Then, REDISRAD-EBF defines an edge-sensitive boosting factor  $K_{i,j}$  for pixel  $(i, j)$  given by

$$K_{i,j} = \frac{T_R}{Ratio\_Matrix_{i,j} + Pruning\_Decision_{i,j} \times (T_R - Ratio\_Matrix_{i,j}) + \epsilon}, \quad (3.4)$$

where

$$Pruning\_Decision_{i,j} = \begin{cases} 1, & \text{if pixel } (i, j) \text{ is rejected by the pruning process} \\ 0, & \text{otherwise} \end{cases}. \quad (3.5)$$

Here,  $K_{i,j}$  is the edge-sensitive boosting factor for pixel  $(i, j)$ ,  $T_R$  is the ratio threshold,  $Ratio\_Matrix_{i,j}$  is the ratio-strength of pixel  $(i, j)$ ,  $Pruning\_Decision_{i,j}$  is the  $(i, j)^{th}$  entry of the pruning decision matrix and  $\epsilon$  is a small constant to avoid division by zero.

For the accepted edge pixels,  $Pruning\_Decision_{i,j} = 0$  and  $Ratio\_Matrix_{i,j} < T_R$ .  $K_{i,j}$  takes a value greater than 1. The lower the value of  $Ratio\_Matrix_{i,j}$ , the higher the value of the boosting factor. If  $Ratio\_Matrix_{i,j} = 0$ ,  $K_{i,j}$  takes a large value. For the false-positive edge candidates rejected by pruning,  $Pruning\_Decision_{i,j} = 1$  and  $Ratio\_Matrix_{i,j} < T_R$ . The  $K_{i,j}$  values for these pixels approach 1. The boosting factor can be considered neutral for the false-positive edge candidates. For the non-edge pixels,  $Pruning\_Decision_{i,j} = 0$  and  $Ratio\_Matrix_{i,j} \geq T_R$ . The  $K_{i,j}$  value for such a pixel takes value from the open interval  $(0,1)$ . The higher the value of  $Ratio\_Matrix_{i,j}$ , the lower the value of the boosting factor.

The edge-sensitive boosting factor takes a high value on the edge regions and a low value on the uniform or non-edge regions of the speckled input image. How REDISRAD-EBF uses this to guide the ICOV-centric edge decisions will be described in Sub-section 3.1.3.1.

### 3.1.2.2 Global diffusion function of REDISRAD-WDF

Instead of maintaining a pruning decision matrix, REDISRAD-WDF explicitly modifies the ratio matrix  $Ratio\_Matrix$  at the pruning stage. Let  $(i, j)$  be the pixel of interest in the 2D image grid. If the ratio-strength,  $Ratio\_Matrix_{i,j}$ , is not the minimum in the pruning window, then REDISRAD-WDF replaces the original value of  $Ratio\_Matrix_{i,j}$  by the ratio threshold value  $T_R$ . At the end of the pruning process, all false-positive candidate edge pixels of the input image would have the ratio edge strength equal to the ratio threshold  $T_R$ . In a sense, they are forced to reside on the boundary of non-edge domain. Other entries of  $Ratio\_Matrix$  remain unchanged.

After updating the ratio matrix through pruning, REDISRAD-WDF introduces a global edge-sensitive diffusion function,  $c_{global}$ . To ensure edge preservation and smoothing of non-edge regions,  $c_{global}$  should be chosen in such a way that it increases monotonically with the increase in ratio-strength. Higher value of  $c_{global}$  would imply higher level of smoothing. We can satisfy this criterion using

$$(c_{global})_{i,j} = e^{-\left(\frac{T_R}{Ratio\_Matrix_{i,j} + \epsilon}\right)^2}, \quad (3.6)$$

where  $\epsilon$  is a small constant,  $Ratio\_Matrix_{i,j}$  is the ratio-strength of pixel  $(i, j)$  and  $T_R$  is the dynamically calculated ratio threshold. For a simpler and effective implementation, we take the Taylor series approximation of Equation (3.6) up to two terms. So,  $c_{global}$  for the pixel  $(i, j)$  is defined as

$$(c_{global})_{i,j} = \frac{1}{1 + \left(\frac{T_R}{Ratio\_Matrix_{i,j} + \epsilon}\right)^2}. \quad (3.7)$$

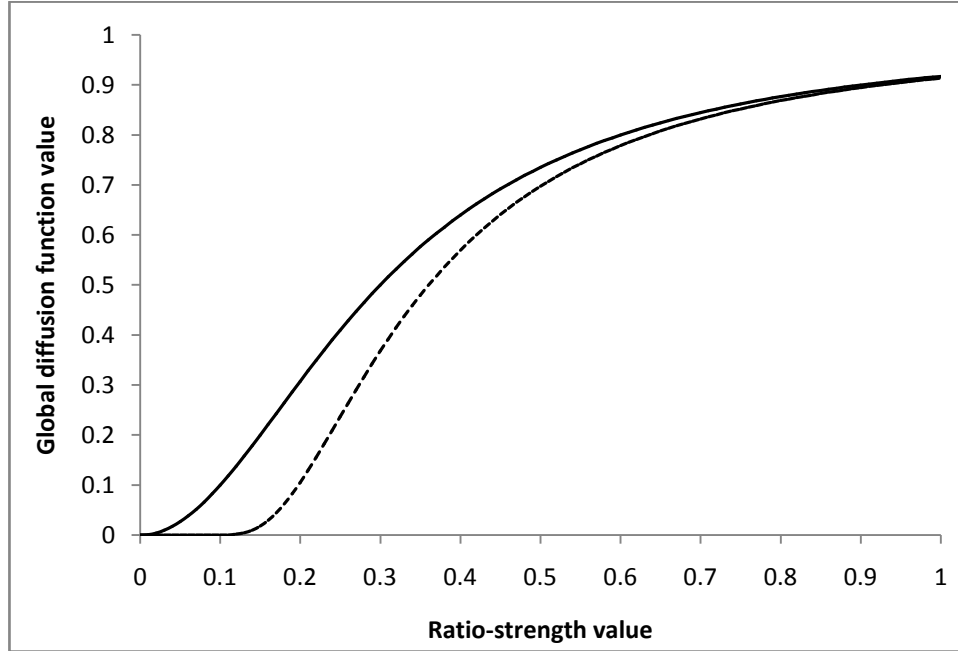


**Figure 3.2** Curves representing two monotonically increasing functions. The dotted line represents the function given by Equation (3.6). The solid line represents the Taylor series approximation of equation (3.6), given by Equation (3.7). The ratio threshold  $T_R$  was taken as 0.3 for both functions.

Figure 3.2 shows the monotonically increasing nature of the functions defined by the Equations (3.6) and (3.7).

If  $Ratio\_Matrix_{i,j} = 0$ ,  $(c_{global})_{i,j} \rightarrow 0$ . If  $Ratio\_Matrix_{i,j} = 1$ ,  $(c_{global})_{i,j} \rightarrow (\frac{1}{1+T_R^2})$ .

It should be noted that the value of the ratio threshold,  $T_R$ , is dynamically computed per image (see Equation (3.2)) and it holds the inequality  $0 \leq T_R \leq 1$ . The global diffusion function  $(c_{global})_{i,j}$  takes a value from the open-close interval  $(0,1]$ , i.e.,  $0 < (c_{global})_{i,j} \leq 1$ . For the strongest edge pixels,  $Ratio\_Matrix_{i,j}$  values approach 0. So  $(c_{global})_{i,j}$  also approaches 0 for these edge pixels. The higher the value of  $Ratio\_Matrix_{i,j}$ , the weaker the pixels are, in terms of edge strength. Higher edge strength (i.e., lower  $Ratio\_Matrix_{i,j}$ ) generates lower value of  $(c_{global})_{i,j}$ . For the non-edge points with high  $Ratio\_Matrix_{i,j}$  values,  $(c_{global})_{i,j}$  takes higher values in its valid domain. How REDISRAD-WDF uses this edge-sensitive global diffusion function will be described in Subsection 3.1.3.2.

### 3.1.3 Guidance of global edge information

#### 3.1.3.1 Guidance offered by REDISRAD-EBF

To propagate the global edge-guidance to the diffusion model, REDISRAD-EBF introduces a boosted scaled-ICOV,  $X_{i,j}$ , for pixel  $(i, j)$  given by

$$X_{i,j} = K_{i,j} \times \sqrt{\frac{(q_{i,j}^t)^2 - (q_0^t)^2}{(q_0^t)^2[1 + (q_0^t)^2]}} \quad (3.8)$$

where  $K_{i,j}$  is the edge-sensitive boosting factor for pixel  $(i, j)$  (see Subsection 3.1.2),  $q_{i,j}^t$  is the ICOV coefficient of original SRAD model at pixel  $(i, j)$  in time/iteration  $t$  and  $q_0^t$  is the scaling factor in time/iteration  $t$ , originally computed by Equation (2.6). Finally the REDISRAD-EBF PDE is given by

$$\begin{cases} \frac{\partial I}{\partial t} = \text{div}[c(X)\nabla I] \\ I(t=0) = I_0 \end{cases} \quad (3.9)$$

where

$$c(X) = \frac{1}{1 + X^2}. \quad (3.10)$$

Here,  $t$  denotes time,  $I_0$  is the initial input image,  $X$  is the boosted scaled-ICOV and  $c(X)$  is the diffusion function of REDISRAD-EBF.

For a 2D image grid, the update equation of REDISRAD-EBF takes the form

$$I_{i,j}^{t+\Delta t} = I_{i,j}^t + \frac{\Delta t}{|\eta|} \text{div}[c(X_{i,j})\nabla I_{i,j}^t] \quad (3.11)$$

which is similar to the equation of SRAD, except for the diffusion function part. Here,  $(i, j)$  denotes the position of a pixel in the 2D image grid,  $I^t$  is the discretely sampled image at time  $t$ ,  $\Delta t$  is the step size,  $|\eta|$  is the size of a given window  $\eta$ ,  $X_{i,j}$  is the boosted

scaled-ICOV value for the pixel at position  $(i, j)$ ,  $\nabla$  denotes the gradient and  $div$  denotes the divergence. The divergence part is approximated by

$$div[c(X_{i,j})\nabla I_{i,j}^t] = \sum_{p \in \eta} c(X_{i,j})(I_p^t - I_{i,j}^t), \quad (3.12)$$

where  $p$  is a pixel in a predefined window  $\eta$ .

The edge-sensitive boosting factor,  $K_{i,j}$ , takes high values for edge pixels and low values for the non-edge pixels. According to Equation (3.4), the boosted scaled-ICOV coefficient,  $X_{i,j}$ , varies proportionally with  $K_{i,j}$ . Due to the ratio-based technique employed,  $K_{i,j}$  is expected to be more accurate than the gradient and Laplacian based ICOV coefficient,  $q_{i,j}^t$ . If  $q_{i,j}^t$  miss-interprets an edge point as a non-edge (by taking a low value), the boosted scaled-ICOV coefficient still takes a high value as it uses  $K_{i,j}$  as a multiplicative factor. If  $q_{i,j}^t$  miss-interprets a non-edge pixel as an edge pixel (by taking a high value), the boosted scaled-ICOV still manages to take a low value. If the ICOV  $q_{i,j}^t$  comes with a right edge-decision, this edge-decision is supposed to be boosted in the right way which ensures more aggressive update at each iteration. That is, where it is required to restrain from flat smoothing, it will restrain more and where smoothing needs to be applied, it will ensure more aggressive smoothing.

The diffusion function,  $c$ , defines the amount of diffusivity need to be incorporated. According to Equation (3.10), if the boosted scaled-ICOV coefficient,  $X$ , value is higher, the diffusion function  $c$  takes a smaller value and vice versa. Since  $X$  takes higher values on the edges and lower values on the uniform regions, the values of  $c$  are low on edges and high on uniform regions. Thereby, REDISRAD-EBF ends up ensuring an appropriate level of smoothing in different sub-regions of the input image; decreased amount of smoothing with the increased strength of edges and increased amount of smoothing with the increase in uniformity.

### 3.1.3.2 Guidance offered by REDISRAD-WDF

In Subsection 3.1.2.2, we already described the global diffusion function,  $c_{global}$ . To use the global edge information provided by  $c_{global}$ , REDISRAD-WDF incorporates a weighted diffusion function  $f$  which is a weighted sum of local and global components. The REDISRAD-2 PDE is given by

$$\begin{cases} \frac{\partial I}{\partial t} = \text{div}[f \cdot \nabla I] \\ I(t = 0) = I_0, \end{cases} \quad (3.13)$$

where

$$f = m \times c_{local} + (1 - m) \times c_{global}. \quad (3.14)$$

Here,  $m$  is a weight constant,  $c_{global}$  and  $c_{local}$  are the global and local components of the weighted diffusion function  $f$ , respectively. The allowed range for the weight constant,  $m$ , is  $0.5 < m < 1$ . The global diffusion component,  $c_{global}$ , is given by Equation (3.7). The original diffusion function of SRAD is taken as the local component  $c_{local}$ , since it relies on the local statistics based ICOV. So, for discrete 2D images,  $c_{local}$  at pixel  $(i, j)$  is given by

$$(c_{local})_{i,j} = \frac{1}{1 + \frac{(q_{i,j}^t)^2 - (q_0^t)^2}{(q_0^t)^2 [1 + (q_0^t)^2]}}, \quad (3.15)$$

where, in iteration/time  $t$ ,  $q_{i,j}^t$  is the ICOV coefficient at pixel  $(i, j)$  and  $q_0^t$  is the scaling factor of the original SRAD model.

In a 2D image grid, the update equation of REDISRAD-WDF takes the form

$$I_{i,j}^{t+\Delta t} = I_{i,j}^t + \frac{\Delta t}{|\eta|} \text{div}[f_{i,j} \nabla I_{i,j}^t], \quad (3.16)$$

where  $f_{i,j}$  is the weighted diffusion function value for the pixel at location  $(i,j)$ . The divergence part is approximated by

$$\text{div}[f_{i,j} \nabla I_{i,j}^t] = \sum_{p \in \eta} f_{i,j} \times (I_p^t - I_{i,j}^t), \quad (3.17)$$

where  $p$  is a pixel in a predefined window  $\eta$ .

According to Equation (3.2), if and only if, all pixels of the input image are edge pixels with ratio strength 0, then  $T_R = 0$ . For meaningful images it is highly improbable that the ratio threshold,  $T_R = 0$ . Though this type of scenario is theoretically valid, it is quite impractical. Thus, the scenario  $c_{global} = 1$  is quite an unlikely one in practice (see Equation (3.7)).

There is a similarity in the behaviors of  $c_{local}$  and  $c_{global}$ . Both are supposed to take smaller values for edges and higher values for non-edges. The local diffusion component,  $c_{local}$ , is governed by local statistics based ICOV coefficient, which suffers from its reliance on gradient and Laplacian. On the other hand, the global diffusion component,  $c_{global}$ , is driven by ratio-based edge detection measure. It is worth mentioning that  $c_l$  changes with time or number of iterations whereas  $c_{global}$  remains static or global throughout the iterative process. So, the core idea is to use the global edge-guidance to guide the local edge-decisions to ensure appropriate level of smoothing.

There is an implicit assumption in the formulation of the weighted diffusion function that gradient and Laplacian based ICOV coefficient is good enough to detect the strongest of edges. For such edges the ratio strength approaches zero and thus  $c_{global} \rightarrow 0$ . In such a case, the global part contributes almost nothing to the weighted diffusion function. Still, we are doing less smoothing due to the weight distribution between local and global diffusion components in Equation (3.14). The global knowledge allows us to reduce the level of smoothing with more confidence. Undoubtedly, the scale of reduction is highly biased by the value of the weight,  $m$ . Thus, tuning  $m$  is crucial.

In the ideally uniform regions,  $c_{global}$  takes a high value in its valid domain. The value is dependent on the dynamic threshold  $T_R$ . The best we can state, in the ideally uniform regions,  $c_{global} \rightarrow 1/(1 + T_R^2)$ . Due to the high value of  $c_{global}$ , the weighted diffusion function  $f$  takes a higher value which tells REDISRAD-WDF to do more aggressive smoothing.

When the condition is not extreme, that is, the underlying sub-region is neither an obvious edge nor an ideally uniform area,  $c_{global}$  should correct the  $c_{local}$  decision, if wrong, and encourage the  $c_{local}$  decision, if right. As  $c_{global}$  is guided by the ratio-based measures, we expect it to take the correct value based on the underlying image region. After computing the weighted diffusion function,  $f$ , we saturate the value of  $f$  so that  $0 \leq f \leq 1$ .

## 3.2 Modified scaling factor and ICOV coefficient

### 3.2.1 Scaling factor selection strategy

SRAD takes the ratio of standard deviation and mean over a small homogeneous region as the scaling factor,  $q_0^t$  (see Equation (2.8)). The homogeneity of the initially selected region is crucial for the optimal performance of SRAD filter. This necessity implies that SRAD requires an experienced user to select this homogeneous region. Moreover, in some cases of SAR images, it is not easy to identify a homogeneous region in the image due to the presence of extensive details. If the region is not homogeneous enough  $q_0^t$  may take a large value. The diffusion function of SRAD given by Equation (2.22) makes it clear that a high value of  $q_0^t$  produces a high value of diffusion function. As a result, SRAD produces over-smoothed image and thereby loses important edge details [9][45].

Aja-Fernández et al. [9] suggested the use of median of ICOV values as the scaling factor. It offers a good balance between de-noising and edge preservation. But, it is not the best choice in all cases. When the initially selected region is perfectly homogeneous or nearly homogeneous, the conventionally scaling factor performs better than the median based one. To exploit the best of both choices, we calculate the percentage of edge pixels in the initial region as an indicator of homogeneity.

To deal with the issue of scaling factor selection, we employ a hybrid strategy. We do not take the ratio of the standard deviation and mean as the scaling factor by default. First, we perform MSP-RoA [41] ratio-based edge detection with dynamic threshold [40] on the initially selected region. The ratio threshold is taken by Equation (3.2).

Let the dimension of the initially selected region  $z$  be  $u \times v$  (in pixels) and  $e$  be the number of pixels in  $z$  identified as edge-pixels. We calculate the percentage of edge pixels in  $z$  by

$$p_e = \frac{e}{u \times v} \times 100. \quad (3.18)$$

Then the the scaling factor  $(q_0^t)_{hybrid}$  is given by

$$(q_0^t)_{hybrid} = \begin{cases} \frac{stdDev(z)}{mean(z)}, & \text{if } p_e < T_e \\ median_{i,j}(q_{i,j}^t), & \text{otherwise.} \end{cases} \quad (3.19)$$

If  $p_e$  is less than a positive threshold  $T_e$ , then we take the conventional ratio of standard deviation and mean over  $z$  as the scaling factor. If not, the median of all instantaneous coefficient of variation (ICOV) values throughout the image is taken as the scaling factor.  $p_e$  is compared against the pre-defined threshold  $T_e$  to determine if the region  $z$  is homogeneous enough or not. We can substantially eliminate the risk of losing finer edge details by using the median based scaling factor when the region is not homogeneous. We suggest  $T_e \leq 3$  for effective implementation.

Both proposed extensions use this scaling factor calculation strategy.

### 3.2.2 ICOV coefficient calculation using larger window

SRAD uses the same window size for the calculations of ICOV coefficient and divergence which was described in Chapter 2. Proposed variants of SRAD operate differently. We promote the use of larger window for ICOV coefficient calculation. The window for divergence calculation is kept the same as SRAD ( $3 \times 3$ ). ICOV coefficient

accounts for the local statistics of the speckled image and by using a larger window we should obtain better local information.

The gradient and Laplacian based ICOV coefficient of SRAD is directly derived from the coefficient of variation of Lee and Kuan which is given by Equation (2.7). Equation (2.7) is simply the 2D image grid approximation of the statistical coefficient of variation which is given by the ratio of standard deviation and mean over a given window. This ICOV coefficient version is used by both of the proposed extensions.

The choice of the window size is tricky. We want to exploit more local information and at the same time, an excessively large window is not preferable since it slows down the computation. We will share our experimental finding in Chapter 4 regarding this aspect.

## Chapter 4

# Experimental Results and Analysis

This chapter provides specific details of our experimental setup and obtained results. A brief introduction to the dataset used and performance measures employed are also given. All presented results can be easily reproduced using the provided details.

The performances of our proposed filters, REDISRAD-EBF and REDISRAD-WBF, are compared with the performances of the Lee [1], Frost [4], homomorphic, DPAD, SRAD and OSRAD filters. The Kuan filter [5] has been excluded from the list since its working principal and performance are almost identical to the Lee filter. For homomorphic filtering, the Perona-Malik anisotropic diffusion filter [23] is used to operate on the log compressed input image. From now on, it will be denoted by homomorphic AD. Among the rest, DPAD and OSRAD are two significant extensions of SRAD. Detailed descriptions of these filters have already been provided in Chapter 2.

Matlab was used for all implementations except that of OSRAD. For OSRAD, we used the publicly available binary version provided by one of the authors, Karl Krissian [7].

## 4.1 Datasets and performance measures

### 4.1.1 Datasets used in different experiments

Our experimental dataset includes three types of images: synthetic, semi-synthetic and real images. Synthetic and semi-synthetic images are used to quantify the performances of various filters. Real images are used to subjectively evaluate filter performances.

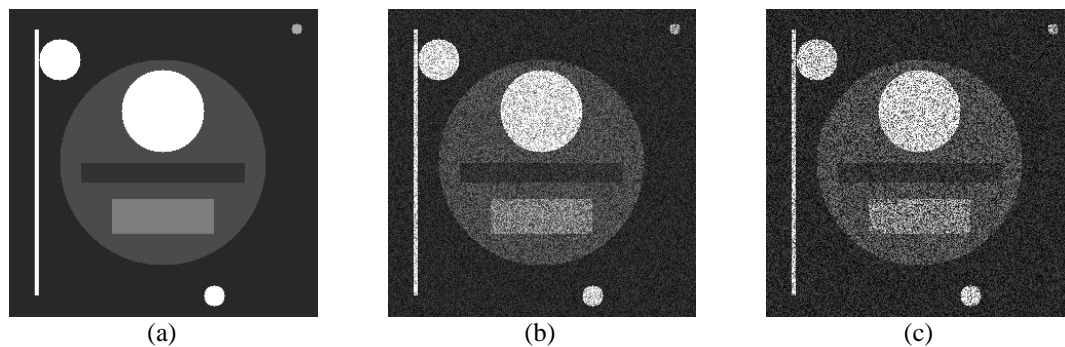


**Figure 4.1** Synthetic dataset for experiments. (a) Noise-free synthetic image containing geometrical shapes, (b) and (c) Corrupted by multiplicative Gaussian noise with zero mean and standard deviation of 0.35 and 0.5, respectively.

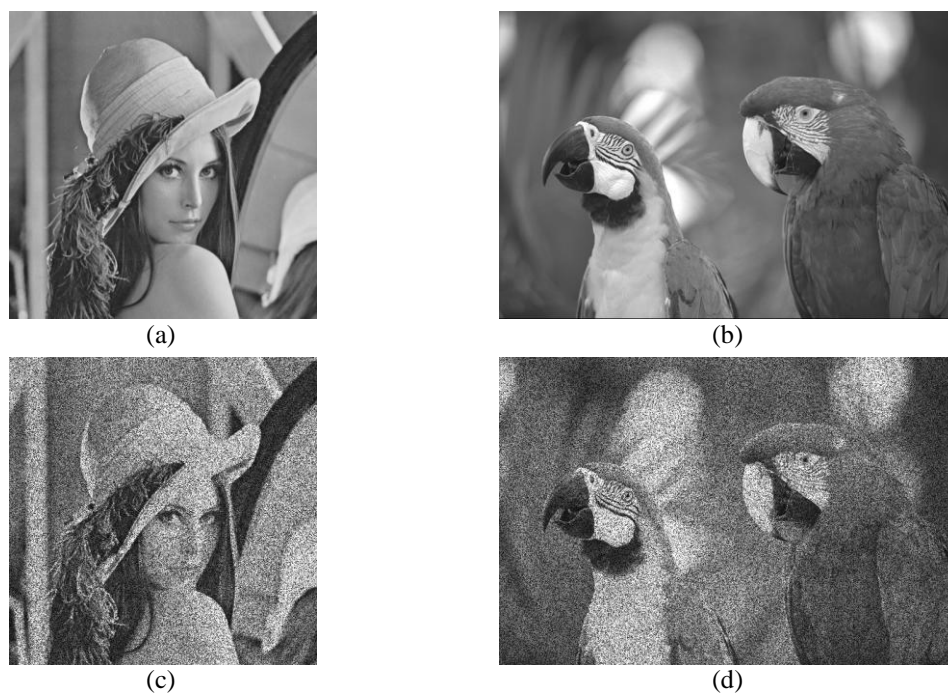


**Figure 4.2** Semi-synthetic dataset for experiments. (a) - (b) Noise-free standard images-- Lena and Parrots, respectively (c) - (d) Lena and Parrots, respectively, corrupted by multiplicative Gaussian noise with zero mean and standard deviation of 0.5.

Figure 4.1 shows the synthetic dataset used in our experiment. A  $300 \times 300$  grayscale image containing some simple geometrical shapes (shown in Figure 4.1(a)) had been corrupted by a multiplicative Gaussian noise with zero mean and standard deviations of

0.35 and 0.5 to generate two different semi-synthetic images (shown in Figure 4.1 (b) and (c)) with different level of synthetic speckle.

Figure 4.2 shows the semi-synthetic dataset generated using two standard grayscale images— Lena and Parrots, of dimensions  $512 \times 512$  and  $768 \times 512$ , respectively. These two images were artificially corrupted by multiplicative Gaussian noise with zero mean and standard deviation of 0.5. Figure 4.2(a) and Figure 4.2(b) show the original noise free images— Lena and Parrots, respectively. The artificially corrupted versions of these images are shown in Figure 4.2(c) and Figure 4.2(d), in the same order.

Our real dataset is composed of four real-life speckled images. Two of them are the SAR images of two cities captured by SIR-C/X-SAR system of NASA (courtesy of NASA JPL [46]). The other two images are ultrasound images of carotid artery (of two different persons) in longitudinal section. The ultrasound images are acquired by Sonix OP ultrasound scanner (courtesy of SPLab [47]).

The real dataset is used for the subjective evaluation of the performances of various filters. Images of this dataset and their de-noised versions (produced by various filters) will be shown at the end of Section 4.4 so that the readers can subjectively compare various de-noised outputs with the original images.

## 4.1.2 Performance measures

The performances of the proposed extensions are evaluated in terms of edge preservation, structural similarity preservation, mean preservation and variance reduction. We also present intensity profiles of the input and filtered output images to check the sharpness of edges and quality of de-noising.

### 4.1.2.1 Pratt's Figure of Merit (FOM)

To compare edge preservation performances of various de-speckling filters we use Pratt's Figure of Merit (FOM) [48]. Pratt's FOM is given by

$$FOM = \frac{1}{\max\{\hat{N}, N_{ideal}\}} \sum_{i=1}^{\hat{N}} \frac{1}{1 + d_i^2 \alpha}, \quad (4.1)$$

where  $\hat{N}$  and  $N_{ideal}$  are the number of detected and ideal edge pixels, respectively,  $d_i$  is the Euclidian distance between the  $i^{th}$  detected edge pixel and the nearest ideal edge pixel and  $\alpha$  is a constant typically set to  $1/9$ . FOM ranges between 0 and 1, where 1 implies the best possible edge detection.

The FOM largely depends on the edge detection method used to generate binary edge maps. We use the Canny edge detector [44] as the edge detector of our FOM implementation. The  $\sigma$  value and the threshold of the edge detector was set to 1 and 0.1, respectively.

#### 4.1.2.2 Mean Structural Similarity Index Measure (MSSIM)

MSSIM, proposed by Wang et al. [49], is used to evaluate the structural similarity preservation performance of various filters. This index is measured based on three comparisons: luminance, contrast and structure.

Let,  $x_i$  and  $y_i$  are two aligned blocks of a reference image  $X$  and a test image  $Y$  (denoised image, in our case). Then, the luminance comparison is given by

$$l(x_i, y_i) = \frac{2\mu_x \mu_y + C_1}{\mu_x^2 + \mu_y^2 + C_1}, \quad (4.2)$$

where,  $l(x_i, y_i)$  denotes the luminance comparison of  $x_i$  and  $y_i$  and  $C_1$  is a constant given by

$$C_1 = (K_1 L)^2, \quad (4.3)$$

where  $L$  is the dynamic range of the pixel values and  $K_1 \ll 1$ .

The contrast comparison,  $c(x_i, y_i)$ , is given by

$$c(x_i, y_i) = \frac{2\sigma_x\sigma_y + C_2}{\sigma_x^2 + \sigma_y^2 + C_2}, \quad (4.4)$$

where  $\sigma_x$  and  $\sigma_y$  denote the standard deviations on image blocks  $x_i$  and  $y_i$ , and  $C_2$  is a constant given by

$$C_2 = (K_2L)^2, \quad (4.5)$$

where  $K_2 \ll 1$ .

The structure comparison function, defined quite similarly, is given by

$$s(x_i, y_i) = \frac{\sigma_{xy} + C_3}{\sigma_x\sigma_y + C_3}, \quad (4.6)$$

where  $C_3 = C_2/2$  and  $\sigma_{xy}$  is defined as

$$\sigma_{xy} = \frac{1}{N-1} \sum_{i=1}^N (x_i - \mu_x)(y_i - \mu_y), \quad (4.7)$$

where  $N$  is the total number of pixels in an image block.

By multiplying  $l(x_i, y_i)$ ,  $c(x_i, y_i)$  and  $s(x_i, y_i)$ , Wang et al. introduced the SSIM index as

$$MSSIM(x_i, y_i) = \frac{(2\mu_x\mu_y + C_1)(2\sigma_{xy} + C_2)}{(\mu_x^2 + \mu_y^2 + C_1)(\sigma_x^2 + \sigma_y^2 + C_2)}. \quad (4.8)$$

Finally, the mean SSIM index over the entire image is given by

$$MSSIM(X, Y) = \frac{1}{M} \sum_{j=1}^M SSIM(x_j, y_j), \quad (4.9)$$

where  $X$  and  $Y$  are the reference and test images, respectively. MSSIM index value ranges between 0 and 1, where 1 means perfect similarity.

According to the recommendation of the Wang et al., we use a  $11 \times 11$  circular-symmetric Gaussian weighting function with standard deviation of 1.5. The constants  $K_1$  and  $K_2$  of equation (4.3) and (4.5) are set to 0.0001 and 0.0003, respectively.

### 4.1.2.3 Mean preservation and variance reduction

A successful speckle reducing filter should not significantly alter the mean intensity within a homogeneous region. At the same time, it should reduce the variation or fluctuation within a homogeneous region. For a fair comparison, we compute the mean and standard deviation over three homogeneous regions in the synthetic and semi-synthetic images.

## 4.2 Parameter adjustment for the proposed filters

### 4.2.1 Window size for ICOV calculation

Window size selection for ICOV calculation is quite tricky. A large window size for ICOV may provide more local statistics, but it increases the computation time. We would prefer a window size which allows gathering enough statistical information and at the same time, not that expensive in terms of computational time.

We use Pratt's FOM and Wang's MSSIM to evaluate the performances of REDISRAD-EBF and REDISRAD-WDF for various window sizes. The semi-synthetic dataset (i.e., the corrupted Lena and Parrots of Figure 4.2) is used as the input. The step size and number of iterations were set to 0.05 and 300, respectively, for both filters. For initial Gaussian smoothing of REDISRAD-EBF and REDISRAD-WDF, we selected a square window of size of 5 and set the standard deviation to 1. A  $15 \times 15$  window was chosen for global ratio matrix calculation and the size of the pruning window was set to 2 (i.e.,  $2 \times 1$ ). The hybrid scaling function was not used in this case. The weight constant  $m$  of REDISRAD-WDF was set to 0.7. Then the semi-synthetic images were de-noised by the proposed filters with different window sizes used for ICOV calculation. As the standard edge detection part of Pratt's FOM, we used Canny's edge detector [44]. The  $\sigma$  value and threshold of the edge detector was set to 1 and 0.1, respectively. The thresholds of Wang's SSIM [49] were set to 0.0001 and 0.0003.

**Table 4.1** FOM and MSSIM values of REDISRAD-EBF for various window sizes used in ICOV calculation.

Window Size	FOM		MSSIM	
	Lena	Parrots	Lena	Parrots
2	0.535	0.474	0.883	0.915
3	0.548	0.463	0.894	0.916
5	0.600	0.491	0.903	0.920
7	0.592	0.512	0.903	0.921
9	0.603	0.536	0.902	0.920
11	0.608	0.519	0.904	0.920
13	0.618	0.500	0.902	0.919

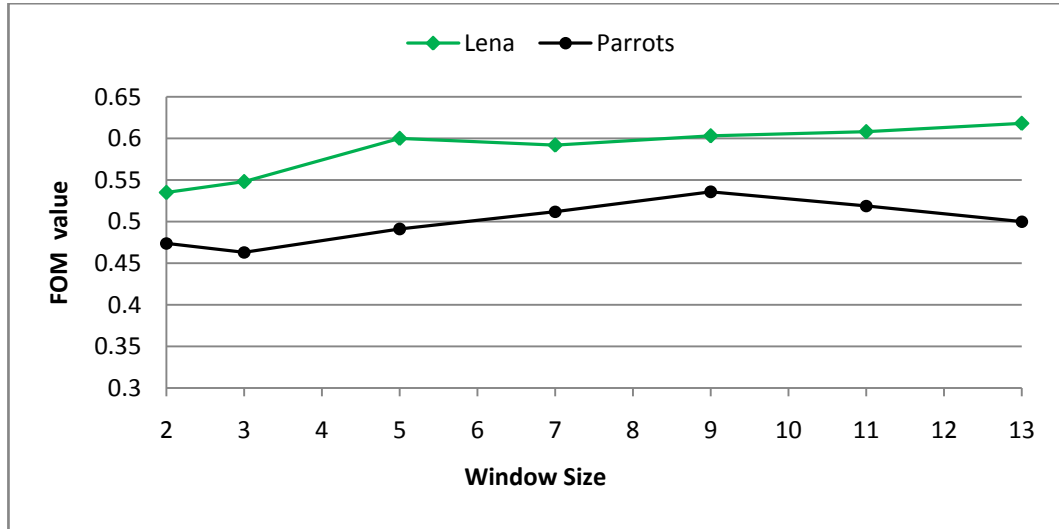
**Table 4.2** FOM and MSSIM values of REDISRAD-WDF for various window sizes used in ICOV calculation.

Window Size	FOM		MSSIM	
	Lena	Parrots	Lena	Parrots
2	0.489	0.351	0.882	0.915
3	0.528	0.391	0.892	0.918
5	0.559	0.403	0.900	0.920
7	0.573	0.409	0.903	0.921
9	0.565	0.411	0.905	0.921
11	0.578	0.427	0.904	0.921
13	0.563	0.410	0.905	0.921

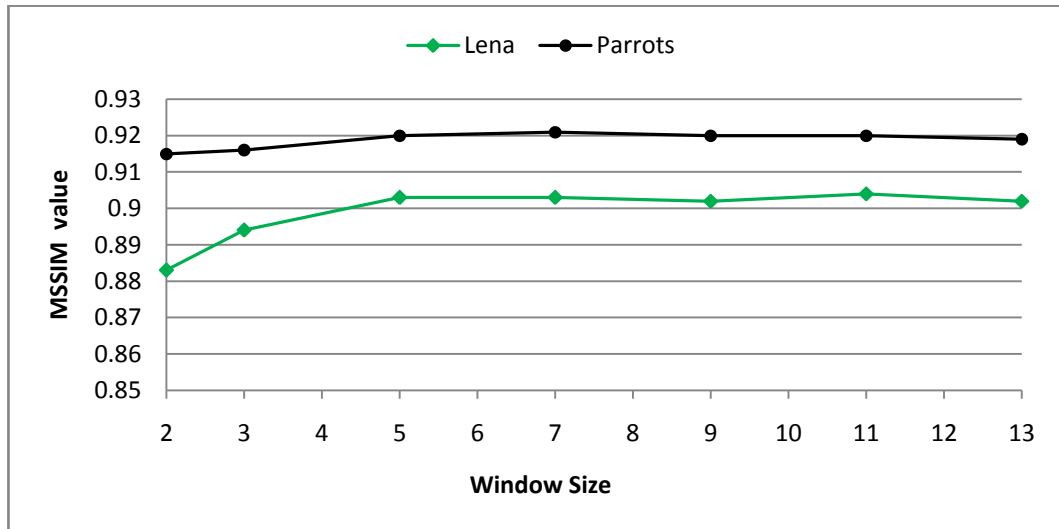
Table 4.1 and Table 4.2 present the resultant FOM and MSSIM values of REDISRAD-EBF and REDISRAD-WDF, respectively, for various window sizes. Figure 4.3 shows the plots of FOM and MSSIM values against window size for REDISRAD-EBF. Figure 4.4 does the same for REDISRAD-WDF. Since we considered only square windows, window sizes are represented by a single number (e.g., 3 for a  $3 \times 3$  window).

According to the tables and the graphs, the window size 5 (i.e., a  $5 \times 5$  window) produces good FOM values and SSIM indices in all cases. Though larger window sizes like 11 or 13 produced slightly better FOM and MSSIM values in some cases, the improvement is not that significant. Moreover, such window sizes will increase the cost of computation to a great extent. Again, the window size 5 shows considerably better performance compared to window sizes 2 and 3. In Figure 4.5 and Figure 4.6, both

window size verses FOM value and window size verses MSSIM value curves are almost saturated after window size 5. This behavior is more prominent in window size verses MSSIM value curves.

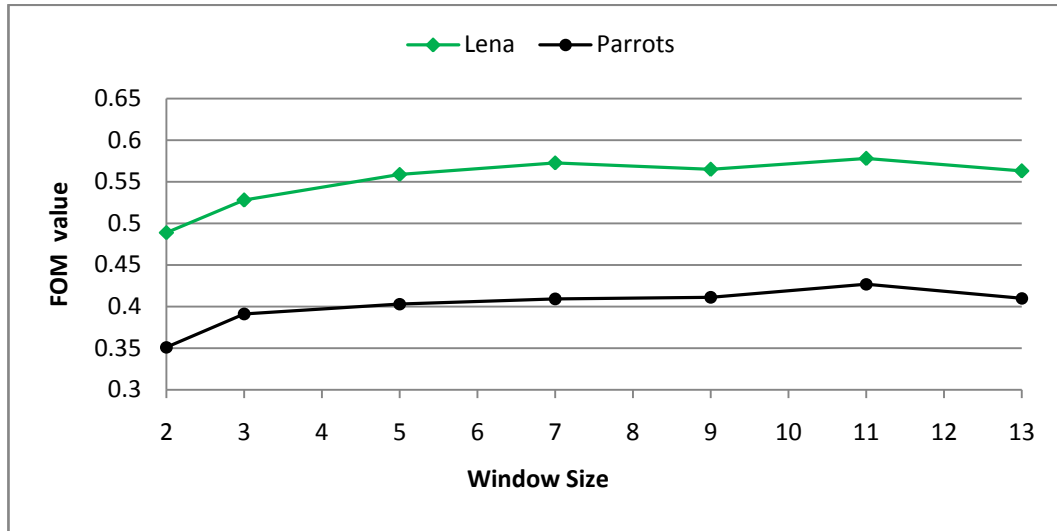


(a)

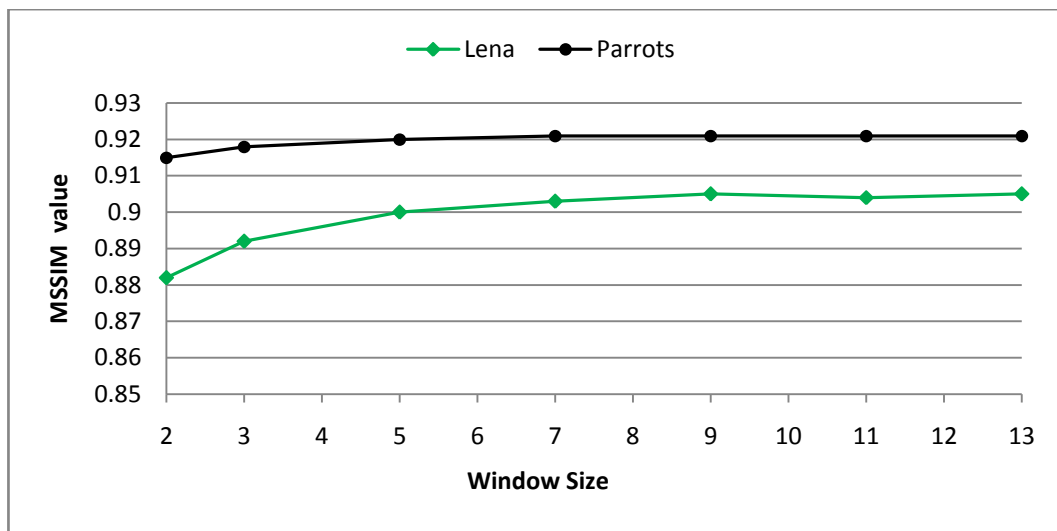


(b)

**Figure 4.3** Performances of REDISRAD-EBF for various window sizes used in ICOV calculation. (a) Window size verses FOM value curves, (b) Window size verses MSSIM value curves. The green and black curves represent REDISRAD-EBF outputs for corrupted semi-synthetic images Lena and Parrots, respectively.



(a)



(b)

**Figure 4.4** Performances of REDISRAD-WDF for various window sizes used in ICOV calculation. (a) Window size versus FOM value curves, (b) Window size versus MSSIM value curves. The green and black curves represent REDISRAD-WDF outputs for corrupted semi-synthetic images Lena and Parrots, respectively.

Analyzing the results, we selected window size 5 for the ICOV calculation REDISRAD-EBF and REDISRAD-WDF.

## 4.2.2 Weight constant $m$ of REDISRAD-WDF

For selecting the weight constant of the diffusion function of REDISRAD-WDF we ran an experiment on the same semi-synthetic dataset used in the previous subsection. The performance measures and experimental setup are also the same as Subsection 4.2.1 except only REDISRAD-WDF was used to de-noise the semi-synthetic images (corrupted Lena and Parrots). For ICOV calculation, a  $5 \times 5$  windows was used according to the finding of the Subsection 4.2.1. REDISRAD-WDF was run for different  $m$  values in the range  $0.5 \leq m \leq 1$ . FOM values and MSSIM indices were calculated for

**Table 4.3** FOM and MSSIM values of REDISRAD-WDF for different values of the weight constant

Weight Constant, $m$	FOM		MSSIM	
	Lena	Parrots	Lena	Parrots
0.5	0.524	0.367	0.897	0.916
0.6	0.561	0.389	0.898	0.916
0.7	0.576	0.404	0.900	0.919
0.8	0.562	0.39	0.900	0.915
0.9	0.534	0.369	0.896	0.913
0.1	0.519	0.364	0.894	0.911

all runs to find out the best  $m$  value.

Table 4.3 summarizes the performances of REDISRAD-WDF for various values of  $m$ . For both synthetically corrupted images (Lena and Parrots),  $m = 0.7$  produced the highest FOM and MSSIM values. So, to ensure optimal performance, REDISRAD-WDF will be run with the weight constant  $m = 0.7$  in all our further experiments.

## 4.3 Experimental settings

This section gives specific details of our experimental setup including filter-specific parameter values and constants. All parameter values and constants are chosen for optimal performance and in most of the cases, suggested by the original authors.

For Lee and Frost filters, a  $7 \times 7$  window was used throughout various experiments. The  $K$  value for Frost filter was set to 5 for real input images, and 3 for synthetic and semi-synthetic images. The step size and number of iterations of homomorphic AD filter were set to 0.1 and 150, respectively. The threshold value for homomorphic AD was set to 0.5 for real images, and 0.3 for synthetic and semi-synthetic images. For DPAD, median of ICOV values was chosen as the scaling factor. The number of iterations and the step size were set to 300 and 0.05, respectively, for DPAD and SRAD. OSRAD was run with step size 0.05. The number of iterations for OSRAD was set to 100 for semi-synthetic images, and 200 for synthetic and real images. The number of iterations, step size, initial Gaussian smoothing window size, window for ratio matrix calculation, size of the pruning window of REDISRAD-EBF and REDISRAD-WDF were set similarly as in sub-section 4.2.1. For the scaling factor calculation strategy of the proposed filters, the threshold  $T_e$  was set to 3 and a small  $3 \times 3$  window was chosen for ratio-based edge detection of the initially selected homogeneous area. According to the finding of Section 4.2, a  $5 \times 5$  window was chosen for ICOV calculation of both proposed filters and the  $m$  value of REDISRAD-WDF was set to 0.7. Parameters for Pratt's FOM and Wang's MSSIM were set as described in Subsection 4.2.1.

## 4.4 Experimental results and analysis

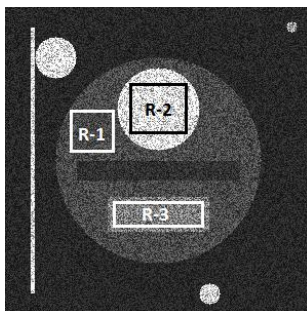
### 4.4.1 Edge and structural similarity preservation

In this section, we compare edge and structural similarity preservation performances of REDISRAD-EBF and REDISRAD-WDF to other speckle reducing filters. The same experiment is run on both synthetic and semi-synthetic images.

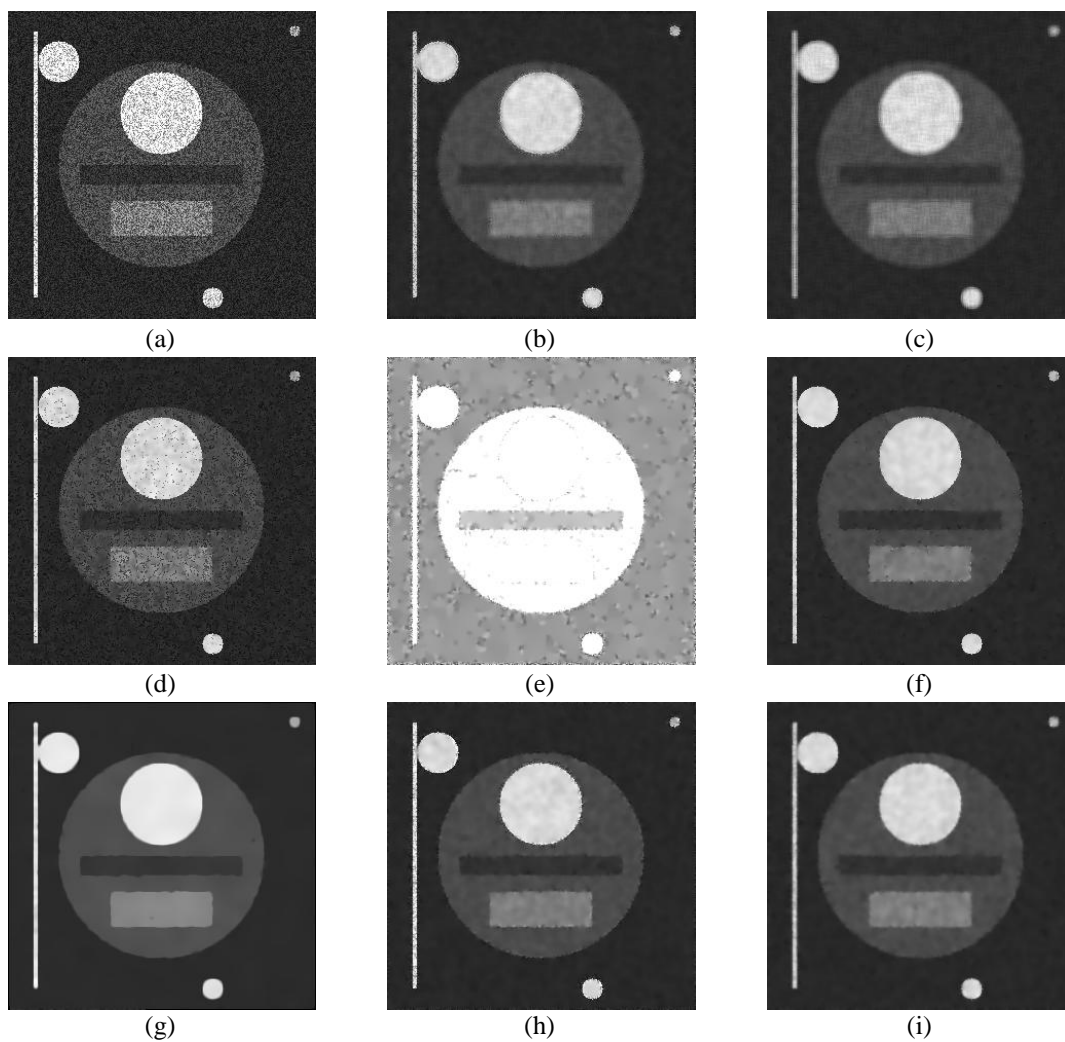
#### 4.4.1.1 Using synthetic dataset

Figure 4.5 shows three homogeneous regions over the artificially speckled version of the synthetic image. These three regions are used for the scaling factor calculation of Lee, SRAD, OSRAD, REDISRAD-EBF and REDISRAD-WDF filters.

Figure 4.6 shows the results of various de-speckling filters applied to the artificially corrupted synthetic image with noise of standard deviation 0.35 (shown in Figure 4.6(a)).



**Figure 4.5** Three different homogeneous regions (marked by rectangles) on the artificially speckled synthetic image, denoted by R-1, R-2 and R-3. These initial regions are used for scaling factor calculation of Lee, SRAD, OSRAD, REDISRAD-EBF and REDISRAD-WDF filters.



**Figure 4.6** Results of various filters on an image with multiplicative noise where  $\sigma_n = 0.35$ . The following filters have been applied: (a) noisy synthetic image with  $\sigma_n = 0.35$ , (b) Lee, (c) Frost, (d) homomorphic AD, (e) DPAD, (f) SRAD, (g) OSRAD, (h) REDISRAD-EBF and (i) REDISRAD-WDF.

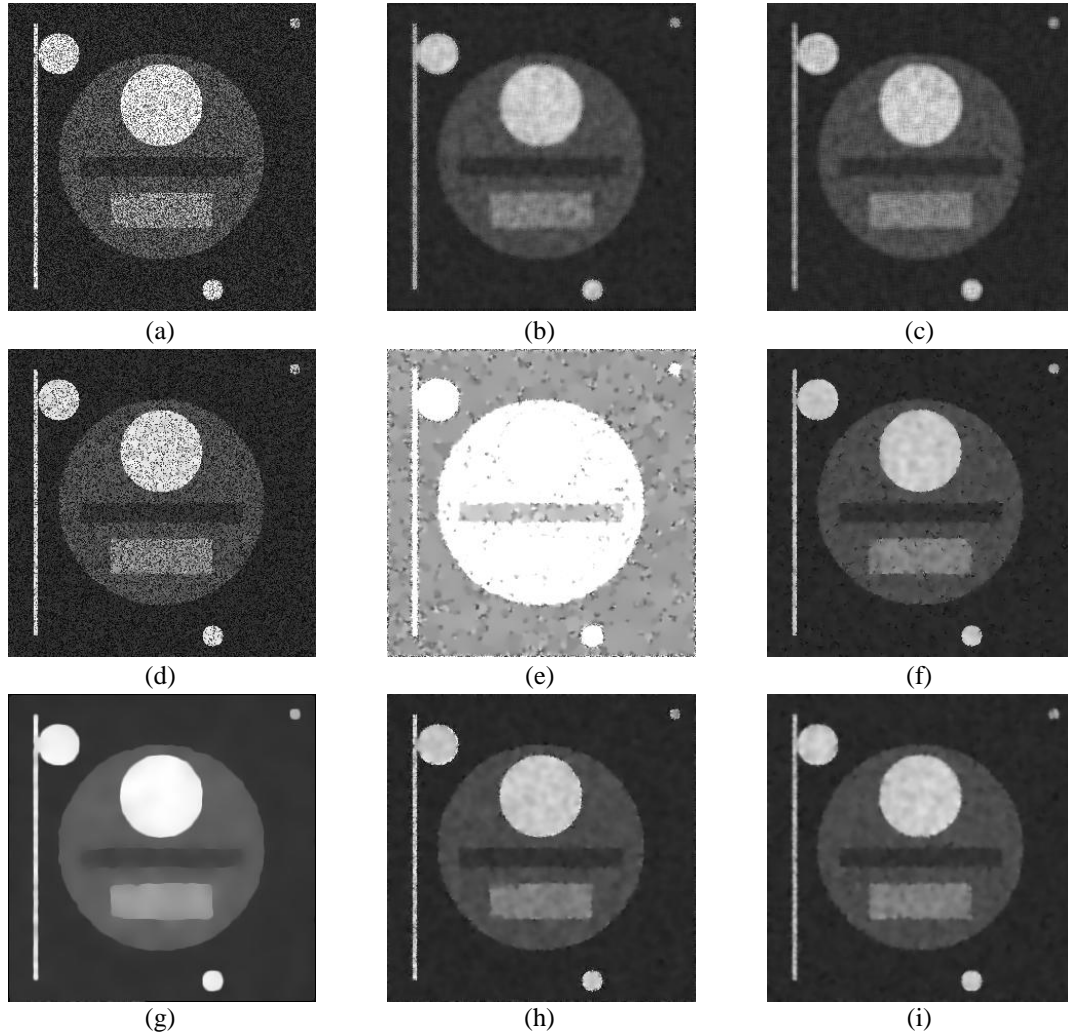


**Figure 4.7** Results of various filters on an image with multiplicative noise where  $\sigma_n = 0.50$ . The following filters have been applied: (a) noisy synthetic image with  $\sigma_n = 0.50$ , (b) Lee, (c) Frost, (d) homomorphic AD, (e) DPAD, (f) SRAD, (g) OSRAD, (h) REDISRAD-EBF and (i) REDISRAD-WDF.

Figure 4.7 shows the results of a similar experiment ran on the synthetic image with noise of standard deviation 0.5. Figure 4.8 shows a 146% zoomed in view of the top-left regions of SRAD, OSRAD, REDISRAD-EBF and REDISRAD-WDF outputs presented in Figure 4.7. This zoomed view will be helpful in subjective evaluation.

The homogeneous regions shown in Figure 4.5 were used for both experiments of Figure 4.6 and Figure 4.7. The results produced using the initial region R-3 (for scaling factor calculation) is presented in Figure 4.6 and Figure 4.7. An initially selected homogeneous

region is irrelevant for Frost, homomorphic AD and DPAD filters since they do not rely on such region for scaling factor calculation.

Table 4.4 summarizes the results of edge and structural similarity preservation experiment on synthetic input image, with two different noise levels. The  $p_e$  columns for two different noise levels present the percentage of edge pixels in the initially selected homogeneous regions (see equation (3.18)) for REDISRAD-EBF and REDISRAD-WDF.

If we have a subjective look at the filter outputs shown in Figure 4.6, Figure 4.7 and Figure 4.8, we will find that SRAD noticeably kept some speckles as edges in presence of higher level of speckle noise ( $\sigma = 0.5$ ). OSRAD seems to do an excellent job in terms of speckle reduction. However, if we look carefully, shapes are diffused and edges are over-smoothed in OSRAD outputs (see Figure 4.8). The FOM values of OSRAD outputs should confirm this observation. Both REDISRAD-EBF and REDISRAD-WDF did a good job in preserving edges and de-noising at the same time. Other filters failed to show satisfactory performances.

According to Table 4.4, both REDISRAD-EBF and REDISRAD-WDF significantly outperformed other filters in terms of edge preservation. For noise level with  $\sigma = 0.35$ , FOM values of REDISRAD-EBF (with different initial regions) were slightly better than that of REDISRAD-WDF. For noise level  $\sigma = 0.5$ , REDISRAD-EBF showed significantly better performance compared to REDISRAD-WDF. Still, REDISRAD-WDF managed to outperform other filters except REDISRAD-EBF. Though SRAD showed good performance in terms of edge preservation for noise level  $\sigma = 0.35$ , it greatly suffered in presence of higher level of noise ( $\sigma = 0.5$ ). Moreover, SRAD showed poor edge preservation performances when operated with initial region R-2 (see Figure 4.5), in case of both noise levels. This validates that performance of SRAD as being greatly dependent on the initially selected homogeneous region. Edge preservation performance of OSRAD was moderate for both noise levels and the edges are noticeably over-smoothed. Lee, Frost, Homo AD and DPAD filters showed poor edge preservation performances for higher level of noise.

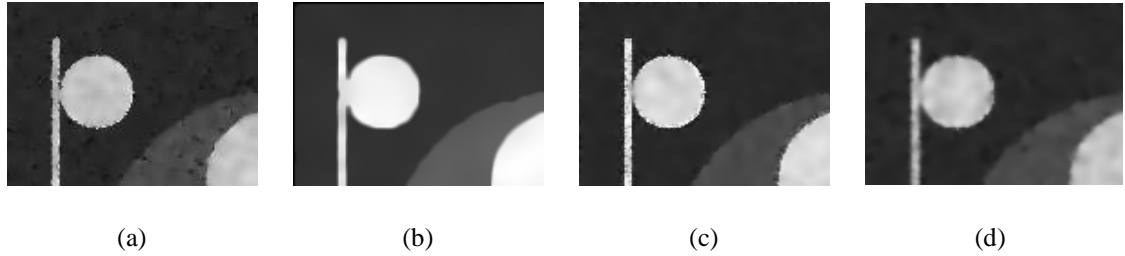


**Figure 4.8** 146% zoomed view of a  $138 \times 101$  sub-region from the top-left corner of output images (presented in Figure 4.7) of -- (a) SRAD, (b) OSRAD, (c) REDISRAD-EBF and (d) REDISRAD-WDF.

**Table 4.4** Results of edge and structural similarity preservation experiment on synthetic dataset with two different noise levels ( $\sigma = 0.35, 0.50$ )

Filter	Initial region	Noise with $\sigma = 0.35$			Noise with $\sigma = 0.50$		
		$p_e$	FOM	MSSIM	$p_e$	FOM	MSSIM
Lee	R-1	-	0.842	0.959	-	0.473	0.933
	R-2	-	0.733	0.850	-	0.474	0.820
	R-3	-	0.888	0.959	-	0.492	0.933
Frost	-	-	0.674	0.921	-	0.510	0.894
Homomorphic AD	-	-	0.455	0.809	-	0.244	0.512
DPAD	-	-	0.302	0.492	-	0.279	0.464
SRAD	R-1	-	0.937	0.975	-	0.659	0.943
	R-2	-	0.472	0.831	-	0.346	0.792
	R-3	-	0.943	0.978	-	0.709	0.943
OSRAD	R-1	-	0.653	0.983	-	0.641	0.960
	R-2	-	0.507	0.953	-	0.518	0.940
	R-3	-	0.653	0.983	-	0.639	0.952
REDISRAD-EBF	R-1	0%	0.964	0.979	0.76	0.922	0.965
	R-2	0%	0.874	0.961	0.04	0.761	0.949
	R-3	0%	0.963	0.979	0.81	0.918	0.965
REDISRAD-WDF	R-1	0%	0.963	0.967	0.76	0.800	0.953
	R-2	0%	0.852	0.962	0.04	0.658	0.948
	R-3	0%	0.951	0.968	0.81	0.806	0.955

Structural similarity preservation performances of OSRAD, REDISRAD-EBF and REDISRAD-WDF are the most impressive according to the presented MSSIM values in Table 4.4. These three filters showed quite similar performances for both levels of noise. Performances of SRAD, Lee and Frost filters were better than homomorphic AD and DPAD filters in terms of structural similarity preservation. However, SRAD showed poor performance when operated with initial region R-2.

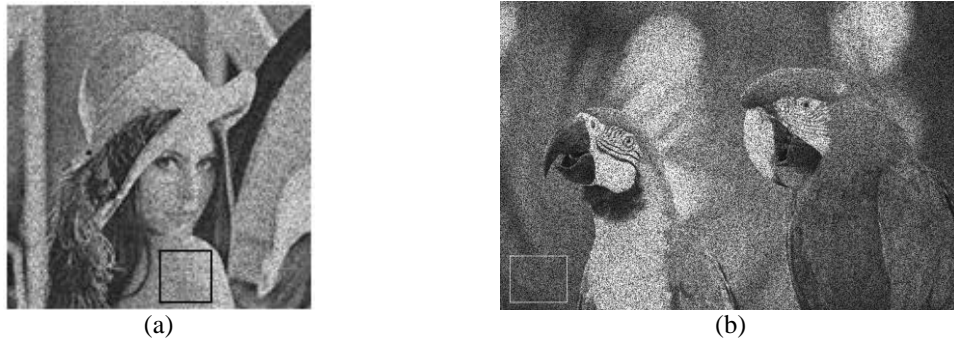
#### 4.4.1.2 Using semi-synthetic dataset

Figure 4.9(a) and Figure 4.9(b) show the initially selected small homogeneous areas used in scaling factor calculation for corrupted semi-synthetic Lena and Parrots images (see Subsection 4.1.1), respectively. Figure 4.10 shows the de-noised outputs of different filters operated on the corrupted version of Lena. Similarly, outputs of the same set of filters operated on the corrupted version of Parrots are presented in Figure 4.11. Finally, Table 4.5 summarizes the results of edge and structural similarity preservation experiment on semi-synthetic input dataset.

In open eyes, OSRAD again did great in terms of noise reduction. However it over-smoothed the edges. As a result, the edges are not sharp and some finer edge details (e.g., wig and lips of Lena) are almost lost. Both REDISRAD-EBF and REDISRAD-WDF did better than SRAD in speckle reduction. At the same time, they kept the finer edge details.

According to Table 4.5, DPAD produced the highest FOM value for input image Lena though its MSSIM index is highly disappointing. For Parrots image, the FOM value of DPAD reduced drastically and the MSSIM index is also very low. So, the performance of DPAD is quite unstable. REDISRAD-EBF and REDISRAD-WDF produced the second and third best FOM values for Lena, respectively. In case of Parrots image, the FOM value of REDISRAD-EBF is the highest in the table and REDISRAD-WDF produced the second highest FOM value. The MSSIM values of both proposed filters are impressive for Parrots, though OSRAD produced the highest MSSIM index.

For both input images (Lena and Parrots), SRAD produced good FOM and MSSIM values, but couldn't manage to beat the REDISRAD-EBF and REDISRAD-WDF versions.



**Figure 4.9** (a) Lena and (b) Parrots-- both corrupted by a multiplicative Gaussian noise with zero mean and standard deviation ( $\sigma$ ) of 0.50. The area marked by a rectangle (black for Lena, gray for Parrots) is taken as the initial homogeneous region.

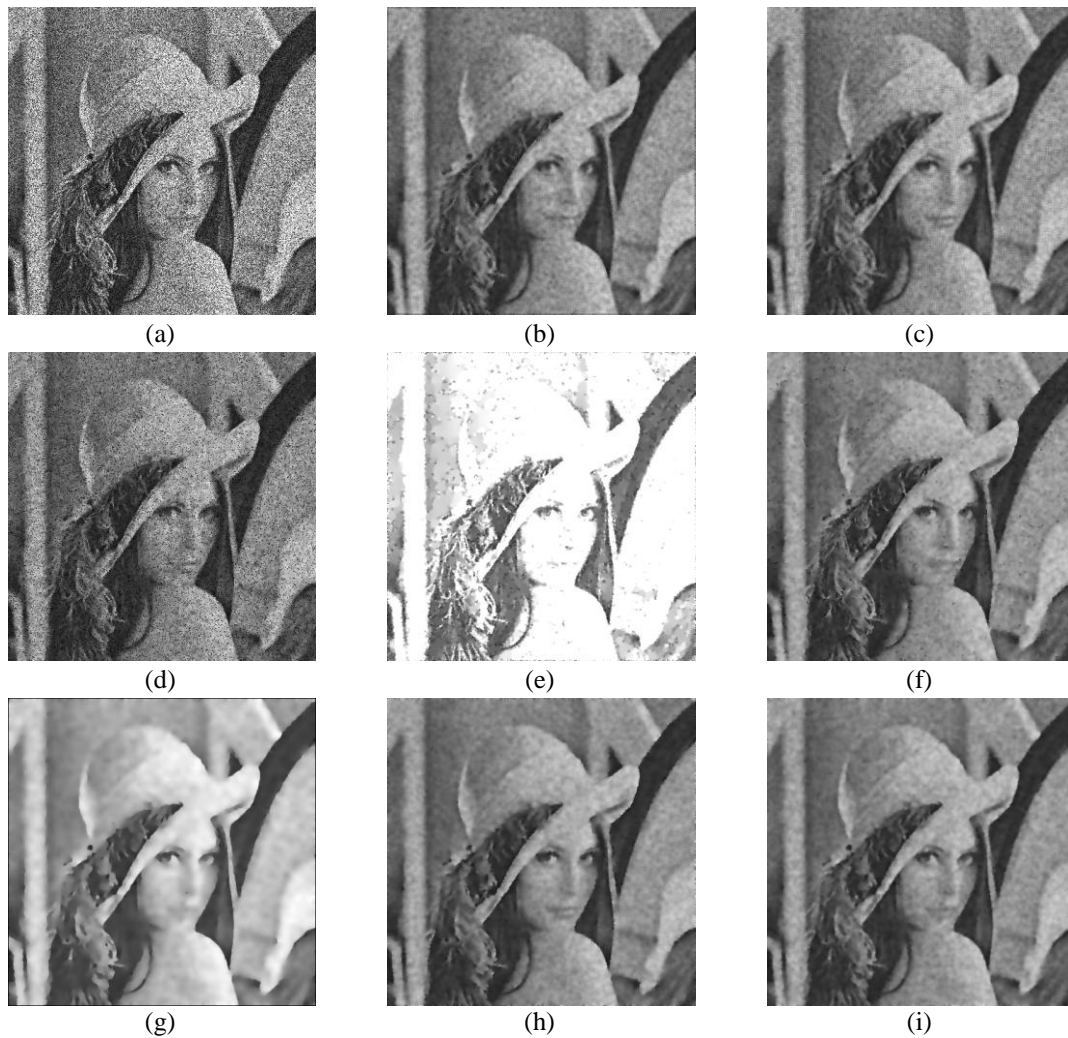


**Figure 4.10** Results of various filters on an image (Lena) corrupted by a multiplicative noise with zero mean and  $\sigma_n = 0.50$ . The following filters have been applied: (a) noisy synthetic image with  $\sigma_n = 0.50$ , (b) Lee, (c) Frost, (d) homomorphic AD, (e) DPAD, (f) SRAD, (g) OSRAD, (h) REDISRAD-EBF and (i) REDISRAD-WDF.

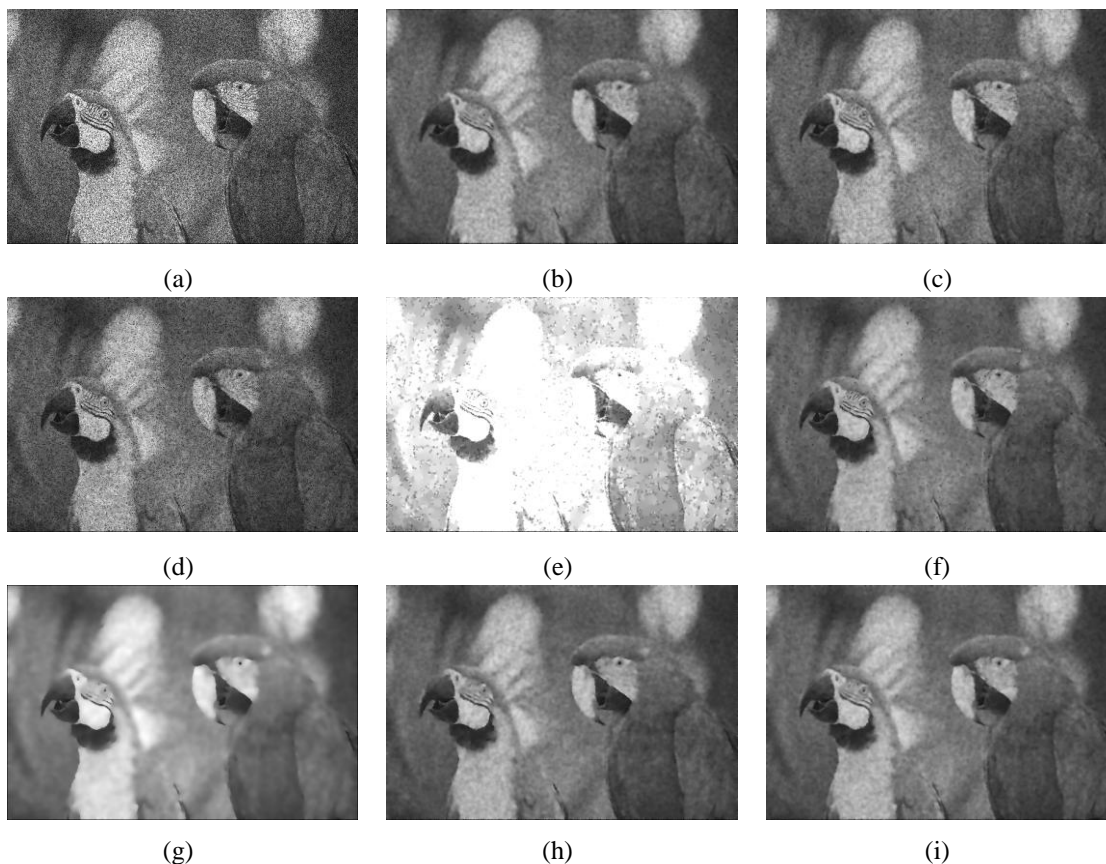


**Figure 4.11** Results of various filters on an image (Parrots) corrupted by a multiplicative noise with zero mean and  $\sigma_n = 0.50$ . The following filters have been applied: (a) noisy synthetic image with  $\sigma_n = 0.50$ , (b) Lee, (c) Frost, (d) homomorphic AD, (e) DPAD, (f) SRAD, (g) OSRAD, (h) REDISRAD-EBF and (i) REDISRAD-WDF.

**Table 4.5** Results of edge and structural similarity preservation experiment on semi-synthetic dataset

Filter	Lena			Parrots		
	$p_e$ value	FOM	MSSIM	$p_e$ value	FOM	MSSIM
Lee	-	0.443	0.869	-	0.310	0.892
Frost	-	0.413	0.851	-	0.266	0.864
Homomorphic AD	-	0.392	0.639	-	0.251	0.663
DPAD	-	0.642	0.528	-	0.323	0.382
SRAD	-	0.515	0.888	-	0.403	0.906
OSRAD	-	0.417	0.882	-	0.283	0.998
REDISRAD-EBF	1.08%	0.582	0.899	1.24%	0.501	0.920
REDISRAD-WDF	1.08%	0.576	0.900	1.24%	0.404	0.919

Though OSRAD produced high MSSIM values for both input images, its edge preservation performances (FOM values) were poor due to over-smoothing.

On average, REDISRAD-EBF stands out as the most successful one closely followed by REDISRAD-WDF in terms of edge and structural similarity preservations.

#### **4.4.2 Mean preservation and variance reduction**

We ran this experiment on the same synthetic and semi-synthetic input datasets used in the earlier edge and structural similarity preservation experiment.

##### **4.4.2.1 Using synthetic dataset**

Figure 4.12 shows another three homogeneous regions (R1, R2 and R3) in the synthetic image used in this experiment. We computed the means and standard deviations over these regions in the noisy synthetic image and de-noised outputs produced by different filters. The same experiment was run on input images corrupted by noise with standard deviations 0.35 and 0.50 (already shown in Figure 4.6(a) and Figure 4.7(a)). Table 4.6 and Table 4.7 present the results of the mean preservation and variance reduction experiment for noise levels of 0.35 and 0.50, respectively.

For the noisy input with standard deviation 0.35, the mean preservation and variance reduction performance of SRAD, REDISRAD-EBF and REDISRAD-WDF are quite similar. They showed good balance between mean preservation and variance reduction. OSRAD showed the best variance reduction performance, but did a poor job in preserving the means over the homogeneous regions. The over-smoothing nature of OSRAD is responsible for that.

For the noisy input with standard deviation 0.50, REDISRAD-EBF showed the best mean preservation performances. SRAD and REDISRAD-WDF are also close to REDISRAD-EBF in terms of mean preservation. OSRAD significantly increased the mean value of all three regions and again performed poorly in mean preservation. Both REDISRAD-EBF and REDISRAD-WDF outperformed other filters except OSRAD in terms of variance

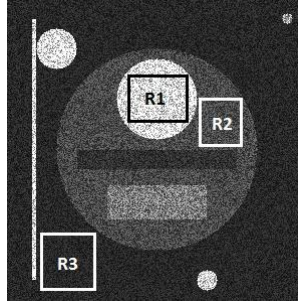


**Figure 4.12** Three homogeneous regions R1, R2 and R3 marked by three rectangles. The mean and standard deviations over these regions of the noisy synthetic image and the de-noised outputs are computed and compared to analyze mean preservation and variance reduction performance.

**Table 4.6** Mean preservation and variance reduction results for the synthetic input image corrupted by a multiplicative Gaussian noise with zero mean and  $\sigma = 0.35$

Filters	Mean			Std dev		
	R1	R2	R3	R1	R2	R3
Noisy	214.00	74.37	40.36	51.25	26.34	14.06
Lee	216.96	74.52	39.90	6.89	4.05	1.97
Frost	216.84	75.86	39.97	8.25	4.53	2.35
Homo AD	210.67	71.70	37.75	19.46	15.26	7.39
DPAD	255.00	254.72	155.40	0.00	2.35	5.29
SRAD	216.43	75.31	40.12	4.79	2.93	1.87
OSRAD	232.09	80.50	43.30	1.83	1.43	0.74
REDISRAD-EBF	217.31	74.49	39.99	5.92	2.80	1.78
REDISRAD-WDF	215.49	74.27	40.10	5.28	2.77	1.54

**Table 4.7** Mean preservation and variance reduction results for the synthetic input image corrupted by a multiplicative Gaussian noise with zero mean and  $\sigma = 0.50$

Filters	Mean			Std dev		
	R1	R2	R3	R1	R2	R3
Noisy	198.70	75.46	39.89	70.26	37.29	20.11
Lee	200.84	75.61	39.91	9.33	5.22	2.89
Frost	197.95	74.56	40.50	13.29	7.34	3.57
Homo AD	197.76	72.68	38.59	59.66	30.65	16.20
DPAD	255.00	252.59	157.34	0.00	11.46	13.03
SRAD	198.59	74.86	40.04	7.45	5.91	3.95
OSRAD	249.84	94.08	50.16	3.79	2.05	1.17
REDISRAD-EBF	198.83	75.28	39.88	7.04	3.41	2.19
REDISRAD-WDF	201.06	76.29	40.14	7.41	3.60	2.35

reduction. Between the two proposed filters, variance reduction performance of REDISRAD-EBF was slightly better than REDISRAD-WDF.

#### 4.4.2.2 Using semi-synthetic dataset

Figure 4.13 shows another three homogeneous regions (R1, R2, R3) in the semi-synthetic images Lena and Parrots (corrupted by a multiplicative Gaussian noise with zero mean and standard deviation of 0.5). Table 4.8 and Table 4.9 summarize the results of the mean preservation and variance reduction experiment operated on corrupted Lena and Parrots, respectively.

According to the results presented in Table 4.8 and Table 4.9, Lee, Frost and SRAD filters did a good job in terms of mean preservation performance. REDISRAD-EBF and REDISRAD-WDF showed the best mean preservation performance though the difference with SRAD was marginal. Meanwhile, homomorphic AD, DPAD and OSRAD performed poorly in terms of mean preservation. Variance reduction performances of Lee, Frost, homomorphic AD and DPAD filters were not satisfactory. DPAD showed unstable performance as usually. Both REDISRAD versions and OSRAD performed better than SRAD in terms of variance reduction. OSRAD won over REDISRAD-EBF in regions R1 and R2, but was significantly outperformed by REDISRAD-EBF in region R3, in terms of variance reduction. The variance reduction performance of REDISRAD-EBF was evenly impressive throughout the all three regions.

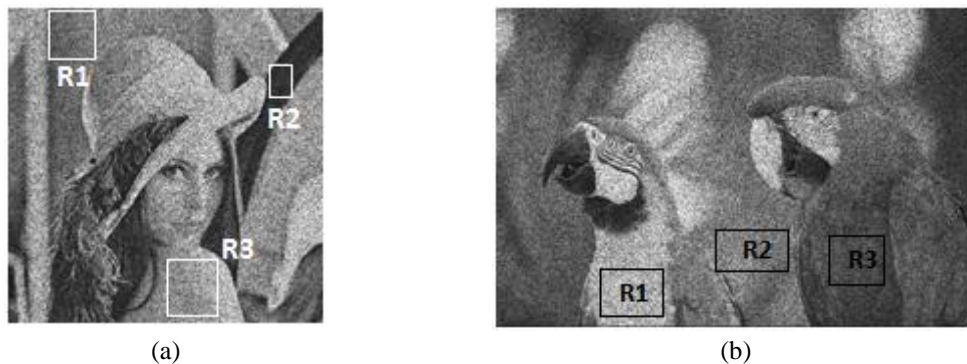


**Figure 4.13** Three homogeneous regions (R1, R2, R3) over semi-synthetic images — (a) Lena and (b) Parrots, marked by white and black colored rectangles, respectively. The mean and standard deviations over these regions of the noisy semi-synthetic images and the de-noised outputs are computed and compared to analyze mean preservation and variance reduction performance.

**Table 4.8** Mean preservation and variance reduction results for the semi-synthetic input image –Lena, corrupted by a multiplicative Gaussian noise with zero mean and  $\sigma = 0.50$ 

Filters	Mean			Std dev		
	R1	R2	R3	R1	R2	R3
Noisy	109.96	50.70	152.33	57.11	26.57	75.50
Lee	108.97	51.41	155.30	12.78	4.83	18.11
Frost	109.72	50.05	152.85	14.53	6.00	19.48
Homo AD	99.12	44.98	141.86	29.56	13.57	42.80
DPAD	232.04	109.10	254.06	23.40	11.97	7.05
SRAD	110.04	50.95	153.68	13.42	5.13	17.02
OSRAD	142.89	65.34	198.59	14.33	3.96	19.75
REDISRAD-EBF	109.68	49.96	152.90	11.74	4.19	16.18
REDISRAD-WDF	109.96	50.52	152.22	12.12	4.33	16.34

**Table 4.9** Mean preservation and variance reduction results for the semi-synthetic input image –Parrots, corrupted by multiplicative Gaussian noise with zero mean and  $\sigma = 0.50$ 

Filters	Mean			Std dev		
	R1	R2	R3	R1	R2	R3
Noisy	174.78	127.41	76.67	76.51	64.67	38.89
Lee	174.84	127.01	76.20	11.24	12.08	8.19
Frost	176.76	126.20	76.65	15.65	16.80	10.27
Homo AD	163.61	116.66	69.37	42.14	35.36	20.41
DPAD	255.00	253.12	183.65	0.00	8.55	19.30
SRAD	175.15	126.94	76.63	9.63	12.06	7.32
OSRAD	217.77	158.94	95.27	6.05	11.73	6.16
REDISRAD-EBF	174.92	125.52	77.13	7.70	8.66	7.09
REDISRAD-WDF	174.69	127.40	76.55	8.29	11.19	6.66

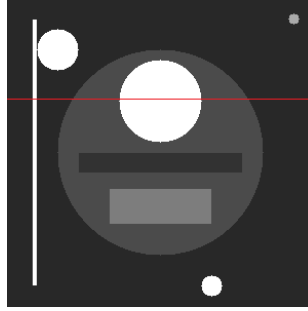


**Figure 4.14** Row number 100 of the 300×300 synthetic image is chosen as the scan line (presented by a red straight line) to generate intensity profiles. Intensity values are collected from the noise-free synthetic, corrupted/noisy ( $\sigma = 0.5$ ) synthetic and de-noised images along the same line.

### 4.4.3 Intensity profiles

In this experiment, we select a horizontal scan line on the input image. Then we plot the intensity value of each pixel along the scan line. Similar plots are generated for the noise-free, noisy and de-noised versions of the same image. This type of intensity profile provides some concrete idea about the sharpness of edges in the output image and overall de-noising performance of different filters.

We use only the synthetic input dataset to generate intensity profiles for different filter outputs. Our synthetic image contains limited number of simple and strong edges which makes it an excellent candidate for the evaluation of edge-sharpness and smoothing performances by one dimensional (1D) intensity profile curves. Images with extensive edge-details are not appropriate for this type of experiment.

In the synthetic image, we select the 100<sup>th</sup> row as the scan line. This scan line is shown in Figure 4.14 as a red straight line. Intensity values are collected from the noise-free, noisy and de-noised synthetic images (generated by different filters). For the noisy synthetic image, we use the image of Figure 4.7(a), which is corrupted by multiplicative Gaussian noise with standard deviation 0.5 and mean 0.

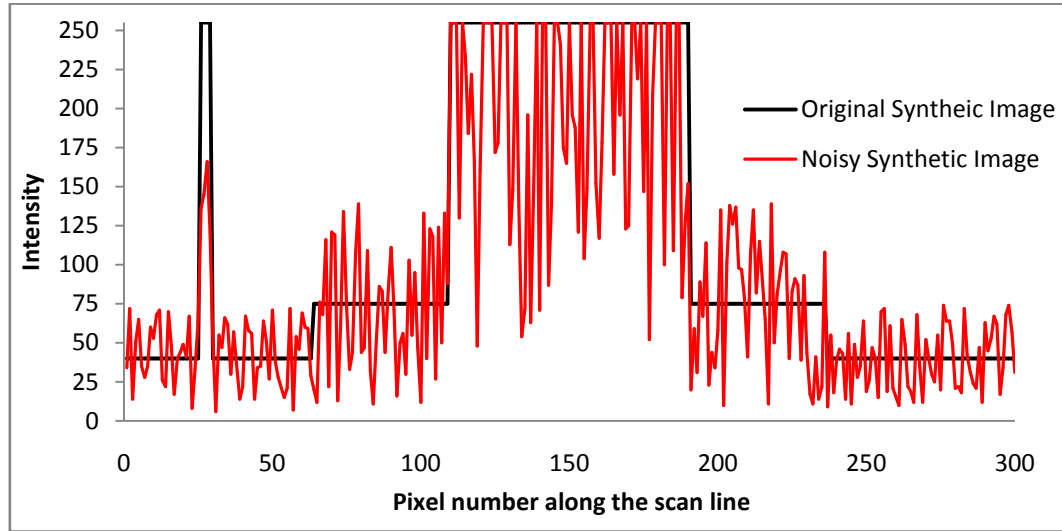


**Figure 4.15** Intensity profiles of the original and noisy synthetic images along the scan line. The black and red curves represent the intensity profiles (along the scan line) of the original noise-free synthetic image and the noisy synthetic image, respectively.

Figure 4.15 shows the intensity profiles of the noise-free and noisy synthetic image along the scan line. The black line refers to the intensity values of the original noise-free synthetic image whereas the red line represents the intensity values of the noisy synthetic image. The horizontal and vertical axes represent pixel numbers along the scan line and intensity values, respectively. It is noticeable in some image regions that the intensity profile of the noisy image is consistently below the noise-free intensity level (e.g., the region between the 100<sup>th</sup> and 200<sup>th</sup> pixel) which is contradictory with the nature of multiplicative Gaussian noise. In fact, these regions represent the white colored areas of the synthetic image and in a grayscale image, there is no way we can have intensity greater than the white grayscale value (255). Due to thresholding, the noisy intensity profile is forced to take intensity values less than or equal to the maximum grayscale value.

Figure 4.16—Figure 4.23, show the intensity profiles along the scan line of the de-noised output images generated by Lee, Frost, homomorphic AD, DPAD, SRAD, OSRAD, REDISRAD-EBF and REDISRAD-WDF, respectively. Each of these intensity profiles is paired with the intensity profile of the noise-free synthetic image so that the edge-preservation and den-noising performance can be compared.

In the intensity profiles of Lee and Frost filters (shown in Figure 4.16 and Figure 4.17, respectively) we observe numerous sharp spikes in the homogeneous regions (horizontal straight lines in the intensity profile of noise-free image). This observation confirms that Lee and Frost filters kept considerable amount of speckles as edge details in the homogeneous regions. The intensity profile of homomorphic AD (Figure 4.18) shows that Homo AD filter completely failed to reduce the speckles. In fact, it produced strong edges (sharp spikes) throughout the entire scan line which validates the fact that homomorphic filters are inefficient in multiplicative speckle reduction.

According to the presented edge profile of DPAD (shown in Figure 4.19), DPAD completely missed the two major edges in the middle (two sharp edges between the 100<sup>th</sup> and 200<sup>th</sup> pixel). Again, in the homogeneous regions it completely failed to maintain the mean intensity level of the original noise-free image.

The intensity profile of SRAD (shown in Figure 4.20) is more impressive than the earlier profiles. It followed closely the original intensity profile curve of the noise-free image in most of the cases. However, it kept some speckles as edges in the homogeneous regions although these spurious edges are not as sharp as that of Lee and Frost filters. Moreover, the edges produced by SRAD are quite un-sharp or smoothed.

Analyzing the intensity profile of OSRAD (Figure 4.21) it can be stated that OSRAD nicely reduced the speckles throughout the scan line but it failed to maintain the intensity level of the original noise-free image in the homogeneous regions. Uncharacteristically, OSRAD managed to keep the intensity level of the homogeneous region at the middle (the vertical straight line in the original noise-free profile, between the 100<sup>th</sup> and 200<sup>th</sup> pixel). This region represents a white circle in the synthetic image (see Figure 4.14). Since white grayscale value (255) is the highest value possible in a grayscale image, the mean-increasing tendency (i.e., poor mean preservation) of OSRAD did not matter in that case. Due to over-smoothing, edges produced by OSRAD are un-sharp. Whenever preserving finer edge details is crucial, this over-smoothing nature of OSRAD may introduce major issues.

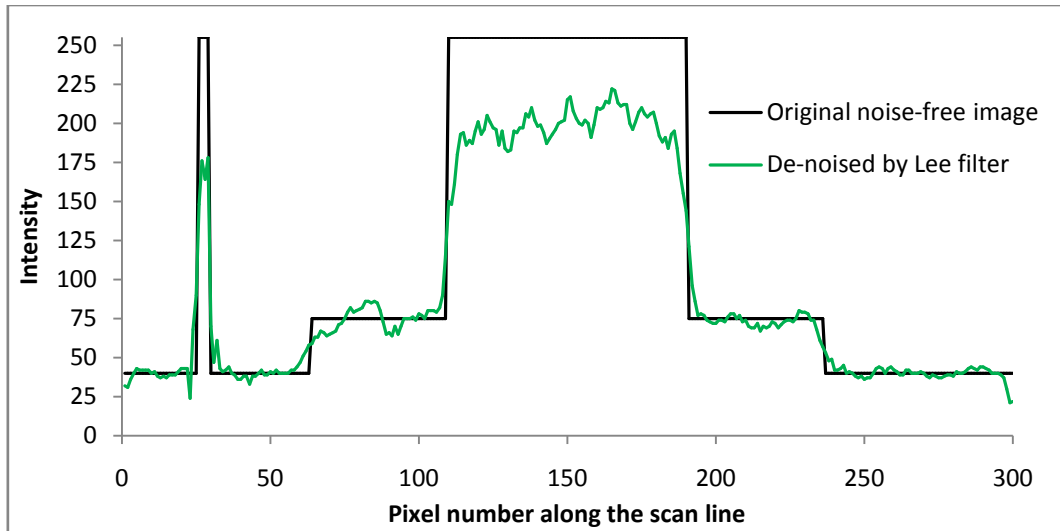


**Figure 4.16** Intensity profiles of the original synthetic image and de-noised output image generated by Lee filter. The black and green curves represent the intensity profiles of the original noise-free synthetic image and the de-noised image, respectively.

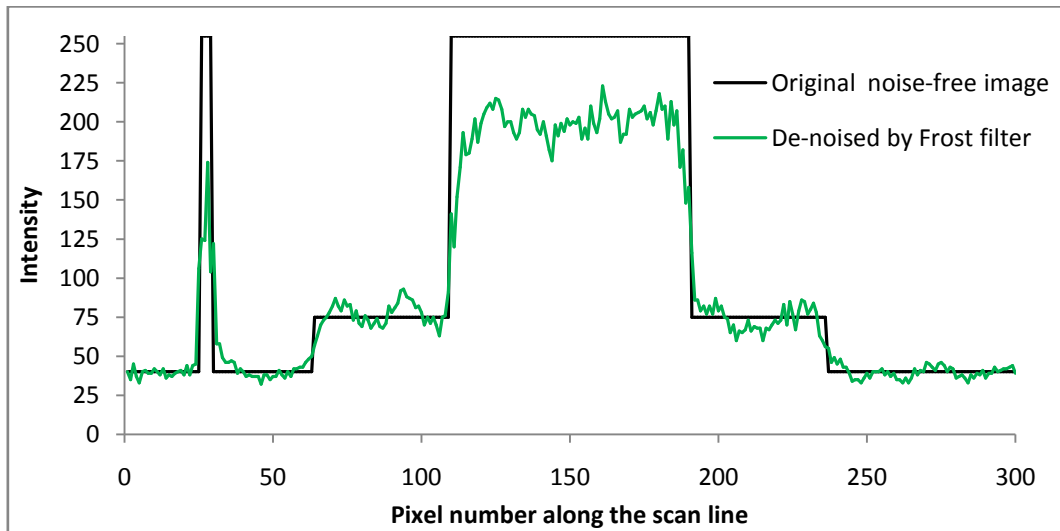


**Figure 4.17** Intensity profiles of the original synthetic image and de-noised output image generated by Frost filter. The black and green curves represent the intensity profiles of the original noise-free synthetic image and the de-noised image, respectively.

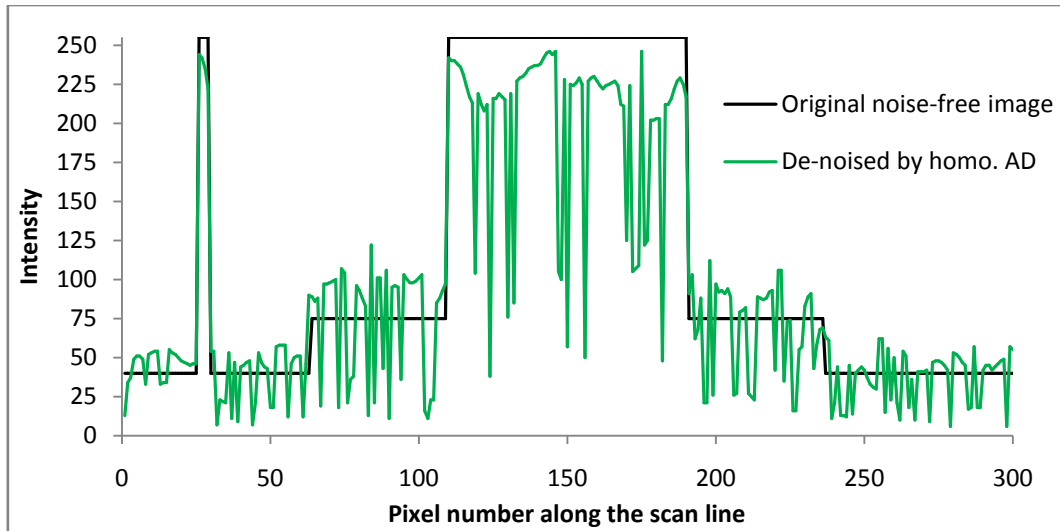


**Figure 4.18** Intensity profiles of the original synthetic image and de-noised output image generated by homomorphic AD filter. The black and green curves represent the intensity profiles of the original noise-free synthetic image and the de-noised image, respectively.

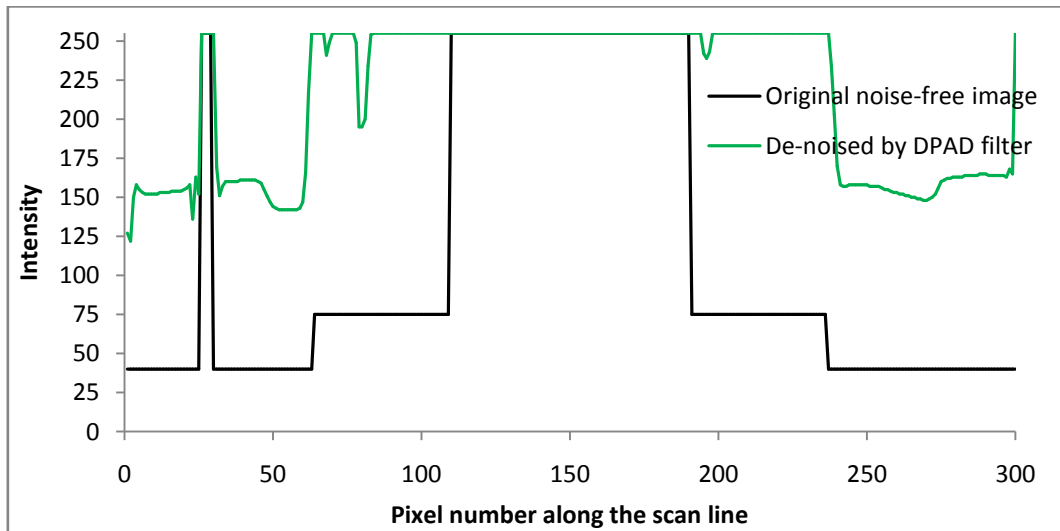


**Figure 4.19** Intensity profiles of the original synthetic image and de-noised output image generated by DPAD filter. The black and green curves represent the intensity profiles of the original noise-free synthetic image and the de-noised image, respectively.

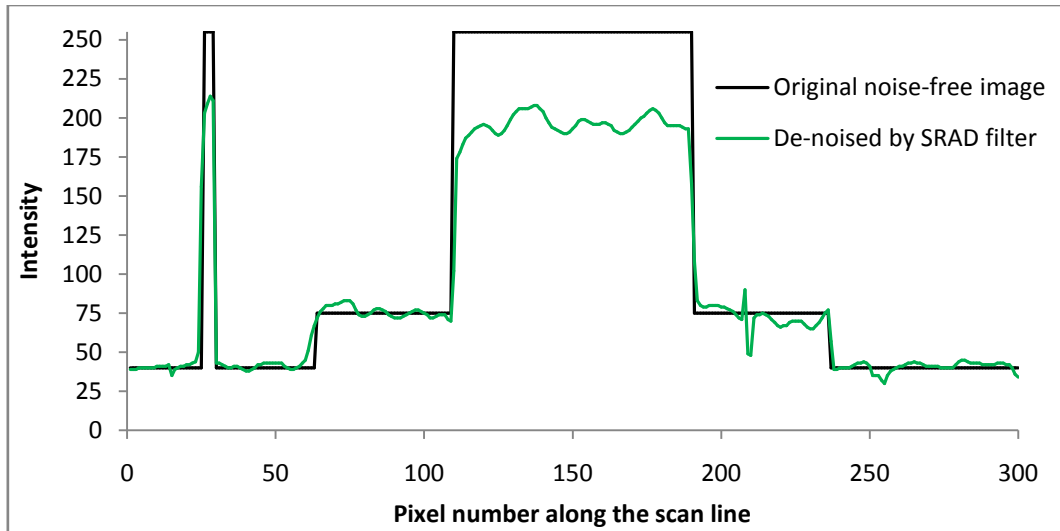


**Figure 4.20** Intensity profiles of the original synthetic image and de-noised output image generated by SRAD filter. The black and green curves represent the intensity profiles of the original noise-free synthetic image and the de-noised image, respectively.

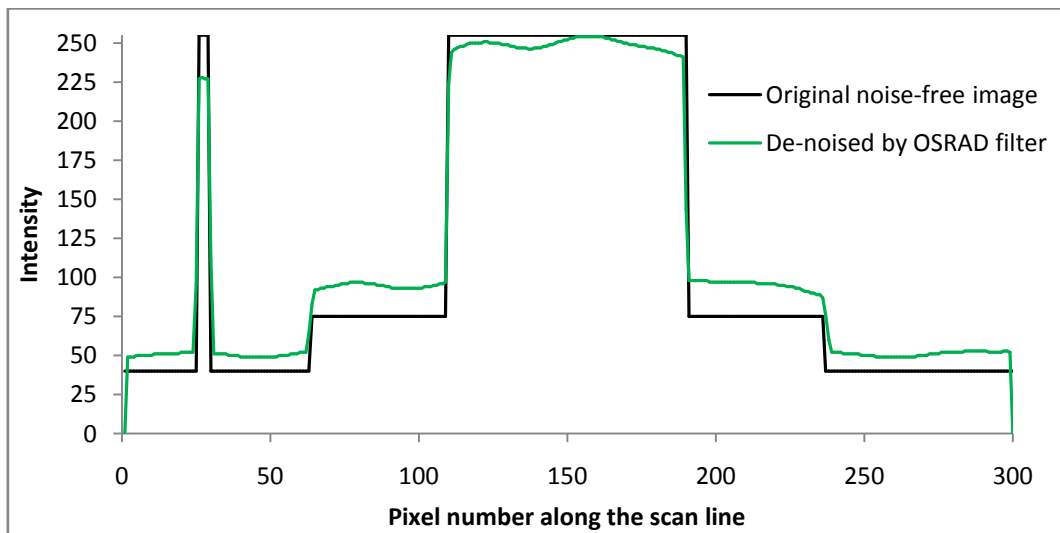


**Figure 4.21** Intensity profiles of the original synthetic image and de-noised output image generated by OSRAD filter. The black and green curves represent the intensity profiles of the original noise-free synthetic image and the de-noised image, respectively.

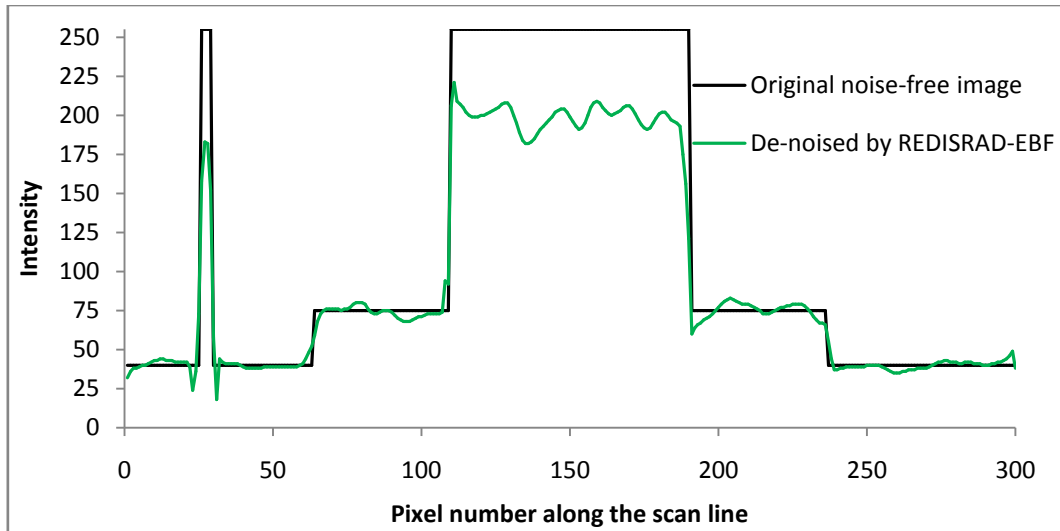


**Figure 4.22** Intensity profiles of the original synthetic image and de-noised output image generated by REDISRAD-EBF filter. The black and green curves represent the intensity profiles of the original noise-free synthetic image and the de-noised image, respectively.

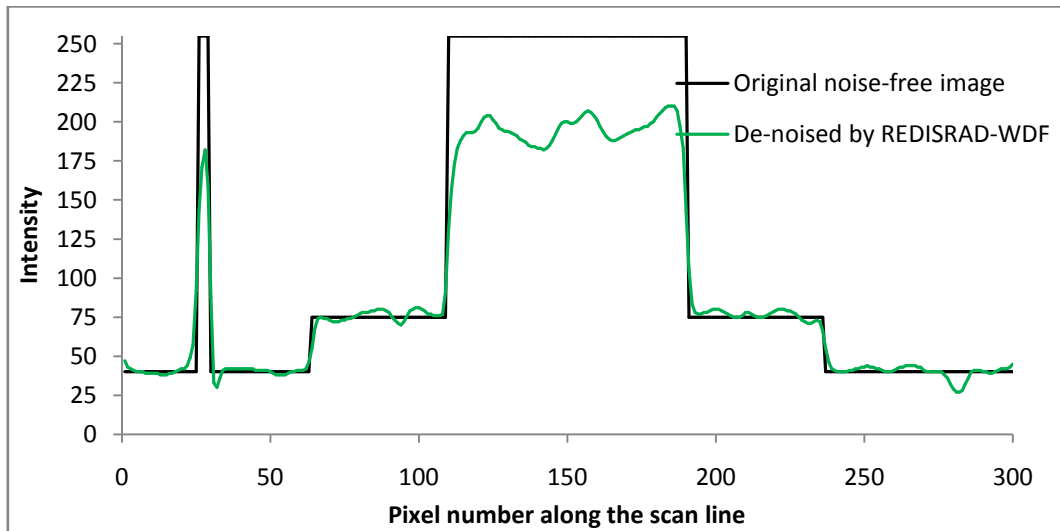


**Figure 4.23** Intensity profiles of the original synthetic image and de-noised output image generated by REDISRAD-WDF filter. The black and green curves represent the intensity profiles of the original noise-free synthetic image and the de-noised image, respectively.

The intensity profiles of REDISRAD-EBF and REDISRAD-WDF (Figure 4.22 and Figure 4.23, respectively) follow the intensity profile of original noise-free image more closely compared to SRAD or any other filters. The smoothing or noise-reduction performances of the proposed filters are good and less spurious edges are present in the homogeneous regions. The edges of REDISRAD-EBF output are significantly sharper than the edges produced by other filters.

#### 4.4.4 Effectiveness on real-world speckled images

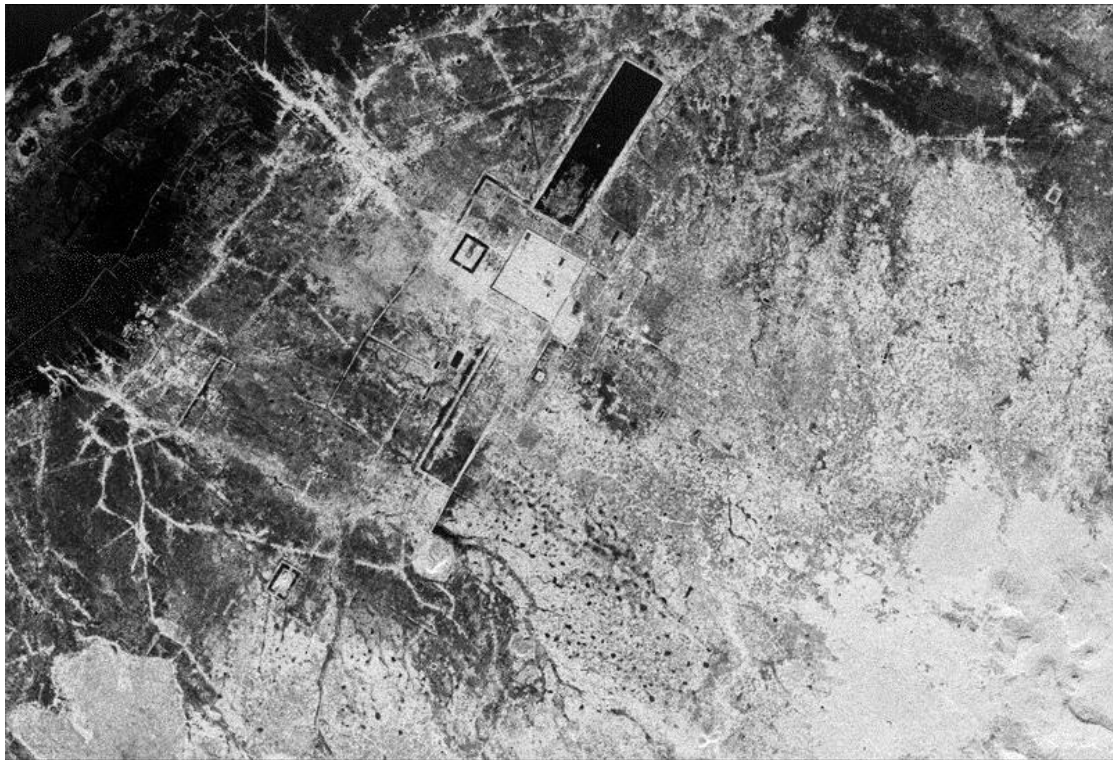
We ran various speckle-reducing filters on our real dataset and then, the performances of REDISRAD-EBF and REDISRAD-WDF are compared with other filters by subjectively analyzing the de-noised output images. Our subjective evaluation is based on speckle reduction, edge preservation and sharpness of the preserved edges in the de-noised image.

The SAR images in our real dataset are shown in Figure 4.24. Figure 4.24(a) is a  $600 \times 314$  radar image of Calcutta, India, that illustrates different urban land-use patterns. Calcutta, the largest city in India, is located on the banks of the Hugli River, shown as the thick, dark line in the upper portion of the image. Two small white lines crossing the dark line are the two bridges over the Hugli river. The surrounding area is a flat swampy region with a subtropical climate. The international airport is in the lower right of the image where two parallel thin lines (airstrips) are visible. On the other hand, the  $800 \times 546$  image of Figure 4.24(b) shows an ancient ‘city of temples’ of the 9<sup>th</sup> century, Angkor in Cambodia. The adjoining lines are the ancient roads and Angkor’s vast canal system. The dark regions are swamps and water reservoirs.

Figure 4.26—Figure 4.33 show the de-noised versions of the SAR images of Figure 4.24 produced by the Lee, Frost, homomorphic AD, DPAD, SRAD, OSRAD, REDISRAD-EBF and REDISRAD-WDF, respectively. For the filters relying on a small region for scaling factor selection, we selected a  $150 \times 90$  rectangular area from the top-left corner of each SAR image (shown in Figure 4.25). For REDISRAD-EBF and REDISRAD-WDF, the threshold  $T_e$  of Equation (3.19) was set to 3 as usual. The percentage of edge pixel ( $p_e$ ) values in the initially selected areas of the SAR images of Calcutta and Angkor were 4.96% and 3.68%, respectively. Since  $p_e > T_e$  for both images, the median of



(a)



(b)

**Figure 4.24** Real SAR images captured by NASA SIR-C/X-SAR system. (a) An urban area of Calcutta, India located on the banks of Hugli river, (b) Temples dating back to the 9<sup>th</sup> century in the city of Angkor, Cambodia.



(a)



(b)

**Figure 4.25** A  $150 \times 90$  rectangular area at the top-left corner of each SAR image (marked by red rectangle). This area is used for scaling factor calculation.

ICOV coefficients was chosen in the runtime as the scaling factor. In Figure 4.24(a), Lee filter performed moderately both in terms of edge preservation and speckle reduction. Some of the preserved edges are quite sharp; however, some fine edge details, like the two parallel thin lines representing the airstrips are completely lost in Lee filter output. In Figure 4.24(b) Lee filter failed to maintain the sharpness of edges. The edges representing the roof tops of the temples and the roads and canal system of the city of Anchor are diffused in most of the cases.

The outputs of Frost, homomorphic AD and DPAD filters (Figure 4.26—Figure 4.28, respectively) are inferior than that of Lee filter in terms of speckle reduction. The output images of the Frost filters are blurry and the preserved edges are not sharp at all. The Frost filter also failed to preserve the fine edges. The homomorphic AD filter kept some speckled as edges as usual. The DPAD filter managed to keep the edges quite sharp, but failed to keep the intensity level at homogeneous regions. Some edges defining the roof tops of the temples in Figure 4.28(a) are completely vanished due to over-smoothing.

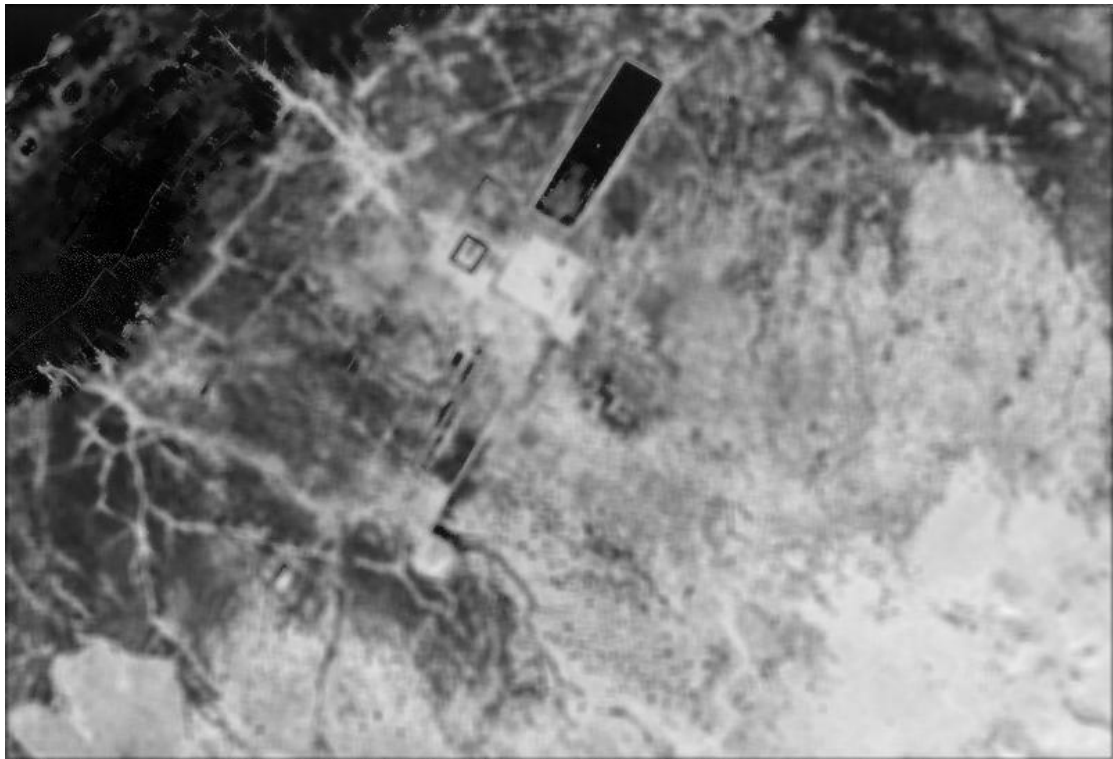
The SRAD filter failed to maintain the sharpness of edges. Some important edge details are also lost in SRAD output. In Figure 4.29(a), edges representing the river, two bridges over the river and the roads passing through the black swampy region in the bottom-middle area of the image are all smoothed and un-sharp. Over-smoothing made the edges dislocated/widened. Two thin parallel lines representing the air strip of the international airport of Calcutta (in the lower right of the image) are completely vanished due to over-smoothing. In Figure 4.29(b), the edges of temple roofs are un-sharp/smoothed in SRAD output. The adjoining lines representing the roads and the canal system of Angkor are also diffused and edges defining them are dislocated/broadened. Subjectively, even the Lee filter performed better than SRAD in terms of edge preservation. However, speckle reduction performance of SRAD was better than Lee filter.

Both output images of OSRAD (Figure 4.31) are highly diffused and the fine edge details are completely lost due to over-smoothing. The over-smoothing nature of OSRAD limits its use in SAR image de-noising since SAR images normally contain a lot of fine details.

According to Figure 4.32, REDISRAD-EBF did an excellent job in preserving finer edge details like the airstrips at the lower right corner of Figure 4.32(a) and the roads and canal systems of Figure 4.32(b). Moreover, the edges are sharper than that of any other filter outputs. REDISRAD-EBF also greatly de-noised the homogeneous regions. Since it avoided over-smoothing of edges, the preserved edges in both outputs are not so dislocated or broadened like OSRAD or SRAD. The REDISRAD-WDF outputs (shown in Figure 4.33) also share similar properties as REDISRAD-EBF. But the edges in REDISRAD-EBF are sharper than REDISRAD-WDF. Still, REDISRAD-WDF did better than other filters other than REDISRAD-EBF in terms of sharpness of the preserved edges.



(a)

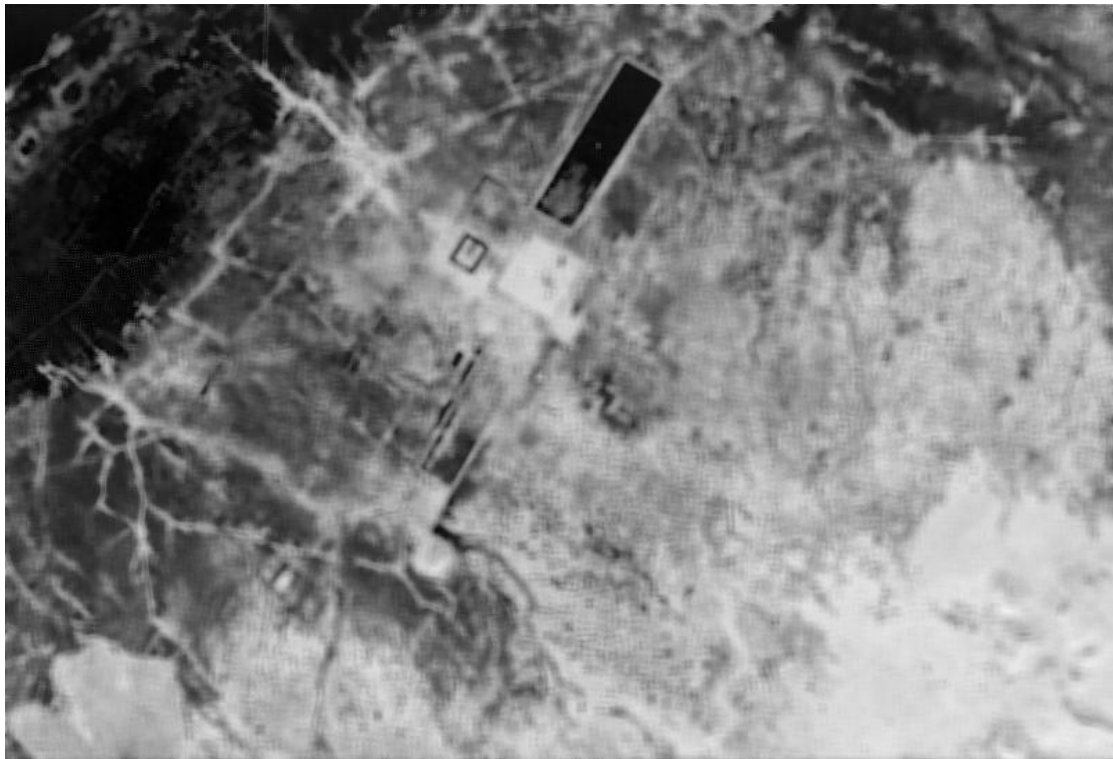


(b)

**Figure 4.26** Two SAR images de-noised by the Lee filter. Resultant de-noised version of the SAR images of (a) Calcutta, India and (b) Angkor, Cambodia.



(a)



(b)

**Figure 4.27** Two SAR images de-noised by the Frost filter. Resultant de-noised version of the SAR images of (a) Calcutta, India and (b) Angkor, Cambodia.



(a)

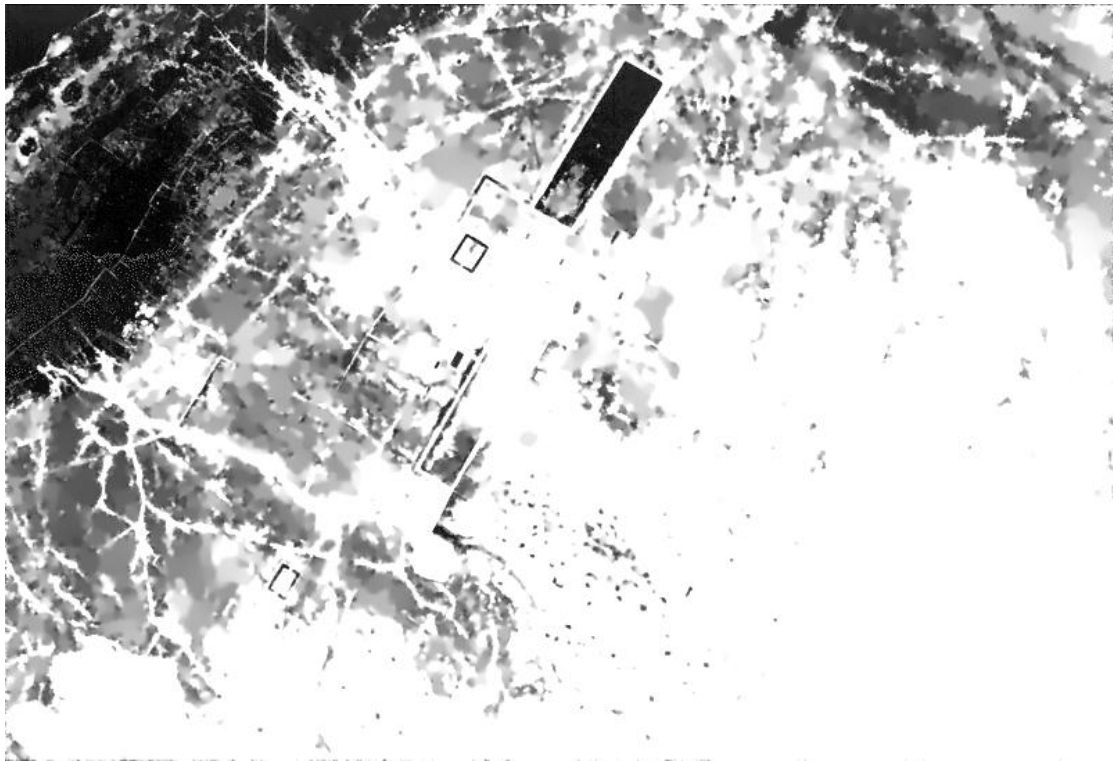


(b)

**Figure 4.28** Two SAR images de-noised by the homomorphic AD filter. Resultant de-noised version of the SAR images of (a) Calcutta, India and (b) Angkor, Cambodia.



(a)

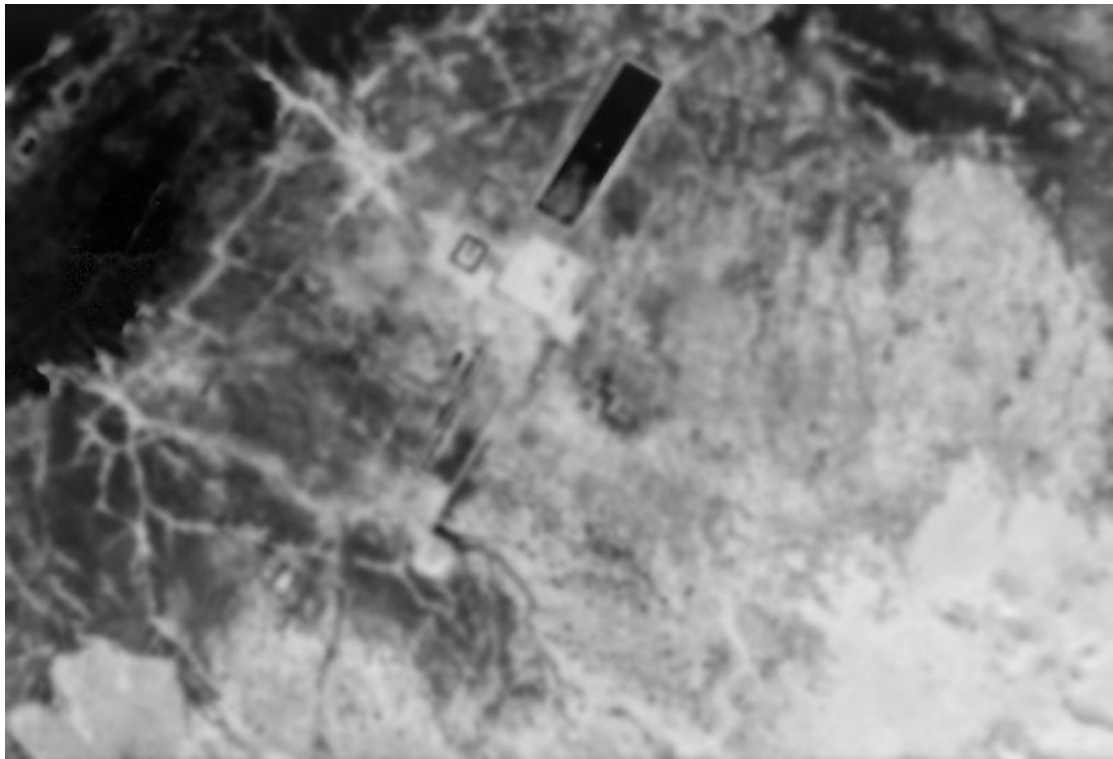


(b)

**Figure 4.29** Two SAR images de-noised by the DPAD filter. Resultant de-noised version of the SAR images of (a) Calcutta, India and (b) Angkor, Cambodia.

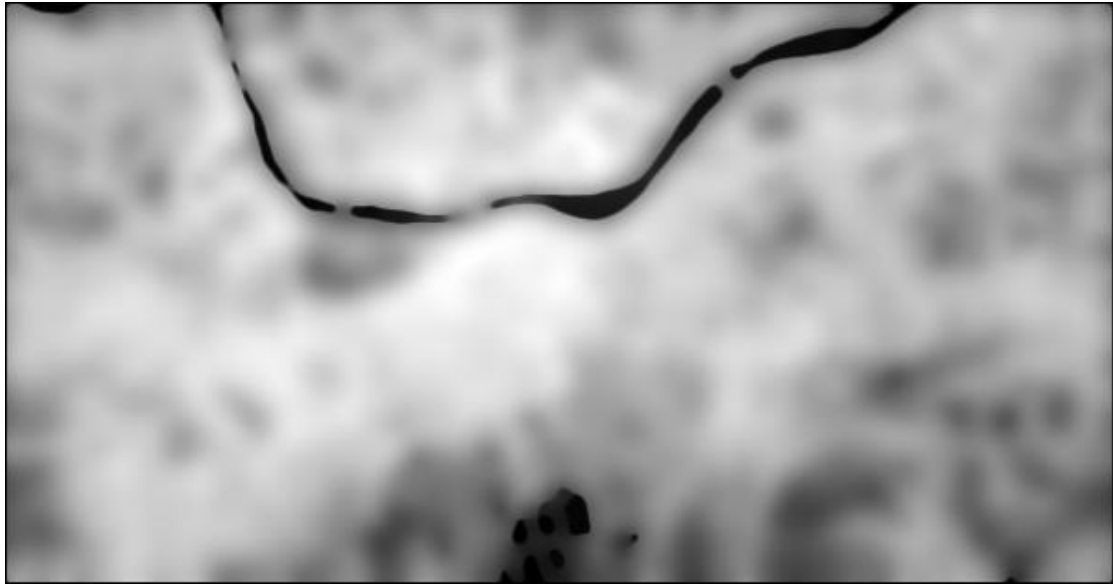


(a)

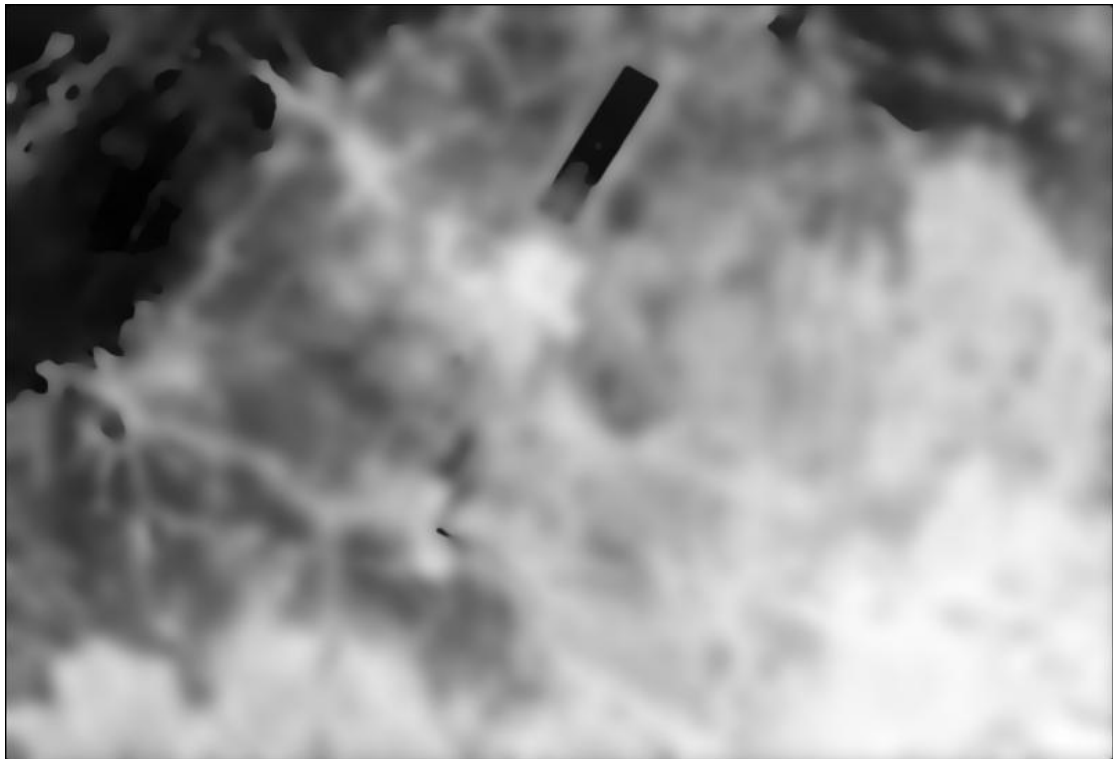


(b)

**Figure 4.30** Two SAR images de-noised by the SRAD filter. Resultant de-noised version of the SAR images of (a) Calcutta, India and (b) Angkor, Cambodia.

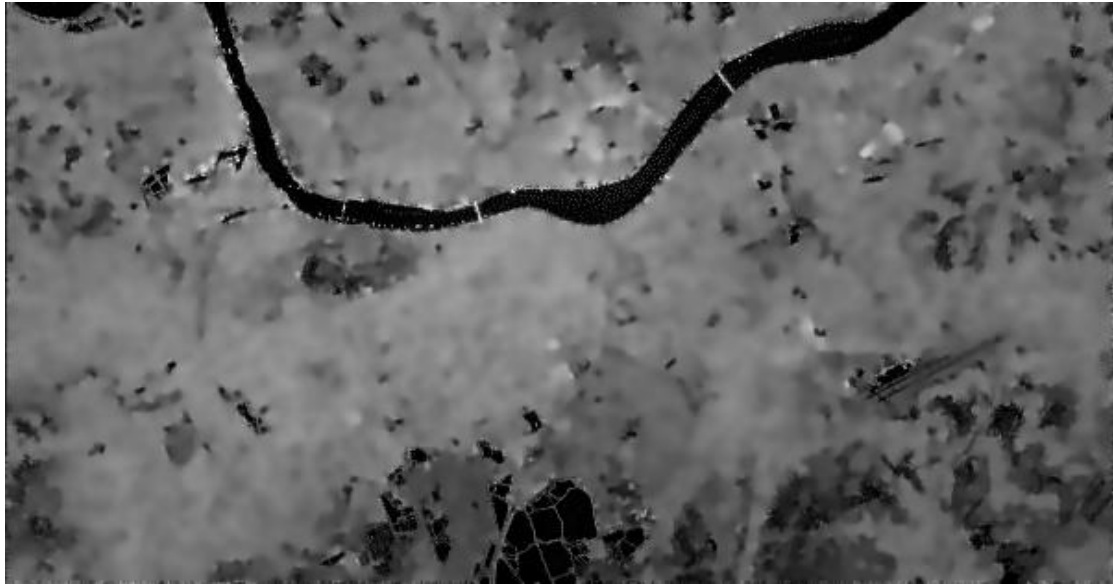


(a)



(b)

**Figure 4.31** Two SAR images de-noised by the OSRAD filter. Resultant de-noised version of the SAR images of (a) Calcutta, India and (b) Angkor, Cambodia.

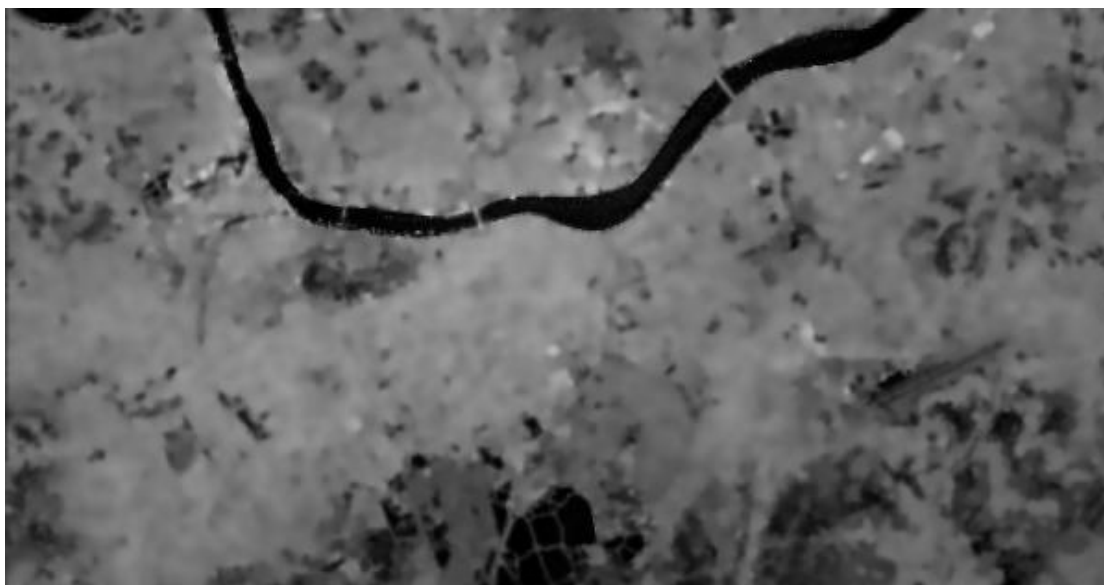


(a)



(b)

**Figure 4.32** Two SAR images de-noised by the REDISRAD-EBF filter. Resultant de-noised version of the SAR images of (a) Calcutta, India and (b) Angkor, Cambodia.



(a)



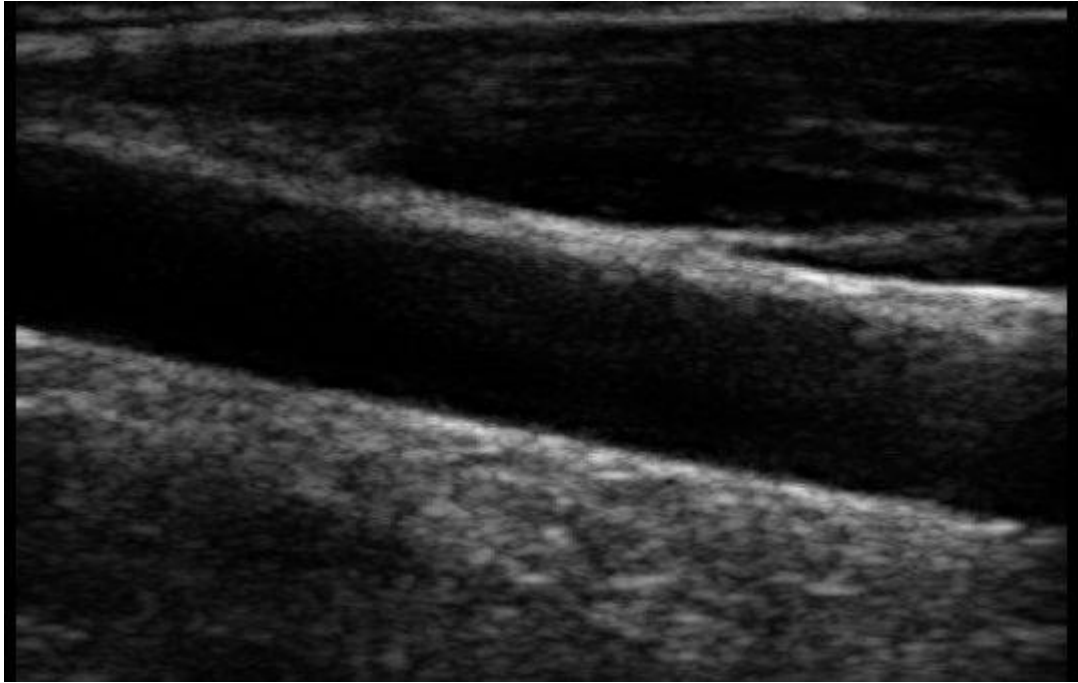
(b)

**Figure 4.33** Two SAR images de-noised by the REDISRAD-WDF filter. Resultant de-noised version of the SAR images of (a) Calcutta, India and (b) Angkor, Cambodia.

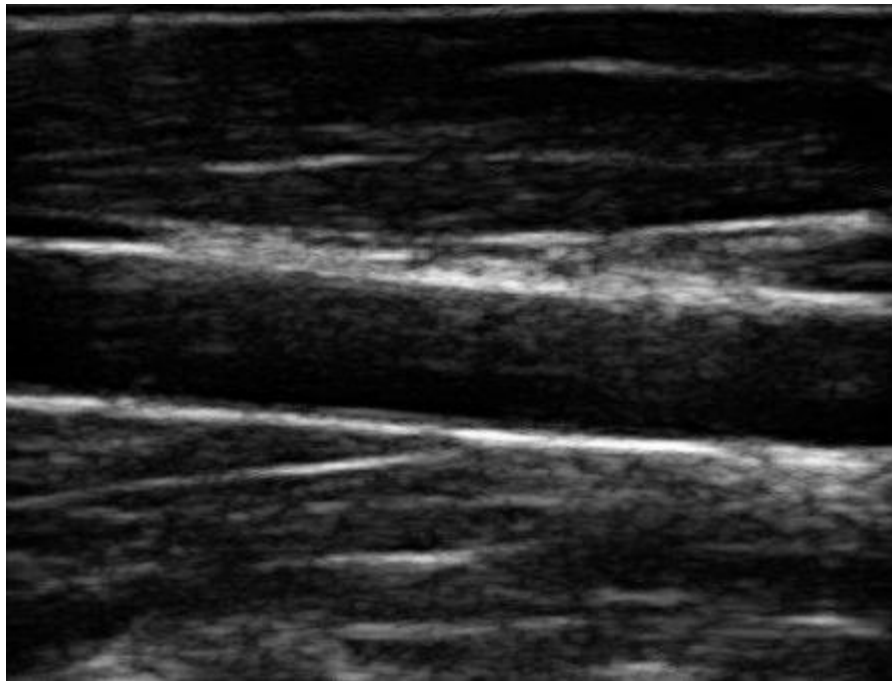
The other two images of our real dataset include ultrasound images of the carotid arteries of two individuals shown in Figure 4.34(a) and Figure 4.34(b) with dimensions  $340 \times 538$  and  $339 \times 446$ , respectively. A  $150 \times 90$  rectangular area in the lower-middle region of each image was selected as the initial homogeneous area for scaling factor calculation (shown in Figure 4.35). The threshold,  $T_e$ , for the scaling factor calculation of our proposed filters was set to 3. Then we ran different filters on the ultrasound images using the settings defined in Section 4.3. The  $p_e$  values for the initial homogeneous regions were 1.61% and 6.78% for the images shown in Figure 4.34(a) and Figure 4.34(b), respectively. As a result, our proposed filters employed the original scaling factor for the image in Figure 4.34(a) according to equation (3.19). For the image in Figure 4.34(b), median of ICOV coefficients was chosen as the scaling factor since  $p_e > T_e$ .

Figure 4.36—Figure 4.43 show the de-noised versions of the ultrasound images of Figure 4.34 generated by Lee, Frost, homomorphic AD, DPAD, SRAD, OSRAD, REDISRAD-EBF and REDISRAD-WDF filters, respectively. Subjective observation of different filter outputs gives the similar impression we got while de-noising SAR images. The edge preservation and de-noising performance of Lee and Frost filter was moderate. Though the edges are not so sharp, they are not highly diffused like OSRAD outputs either. The homomorphic AD and DPAD filters performed poorly in terms of speckle reduction. DPAD failed to maintain the intensity levels in the homogeneous regions as usual.

Again, the edges in SRAD outputs are diffused and un-sharp due to over-smoothing. Edge diffusion resulted in edge dislocation. This over-smoothing and edge dislocation/broadening behavior is more severe in case of OSRAD. Except the major edges, finer details are entirely lost in OSRAD outputs. REDISRAD-EBF again produced the sharpest edge lines and at the same time, did a good job in speckle reduction. It also managed to preserve finer edge details compared to OSRAD and SRAD. Since the boundaries of contours are not diffused like OSRAD or SRAD, it managed to reduce edge dislocation. REDISRAD-WDF outputs show similar properties as REDISRAD-EBF outputs. But the edges preserved by REDISRAD-WDF are not as sharp as that of REDISRAD-EBF.

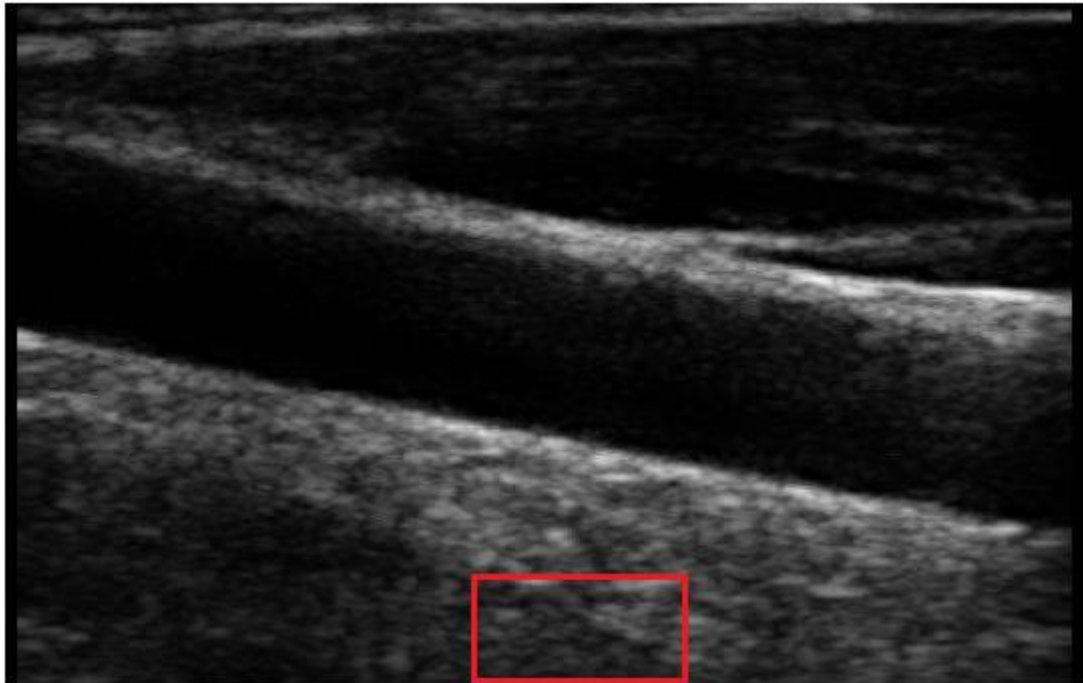


(a)



(b)

**Figure 4.34** Ultrasound images of carotid artery (of two different persons) in longitudinal section acquired by Sonix OP ultrasound scanner. The dimensions of the images of (a) and (b) are  $340 \times 538$  and  $339 \times 446$ , respectively.

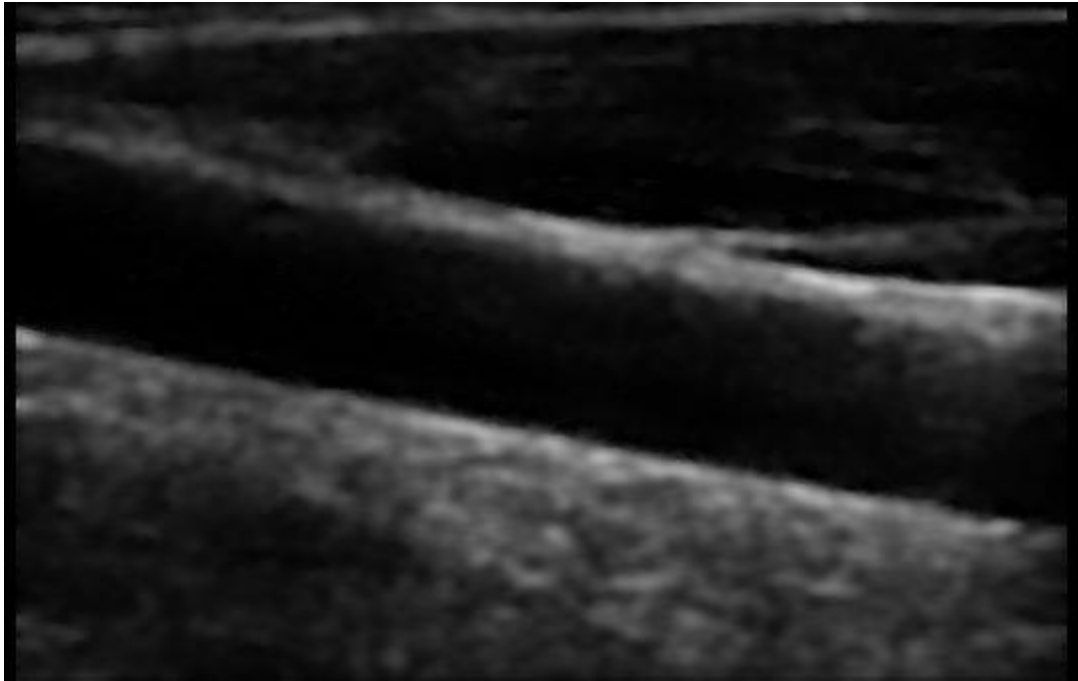


(a)

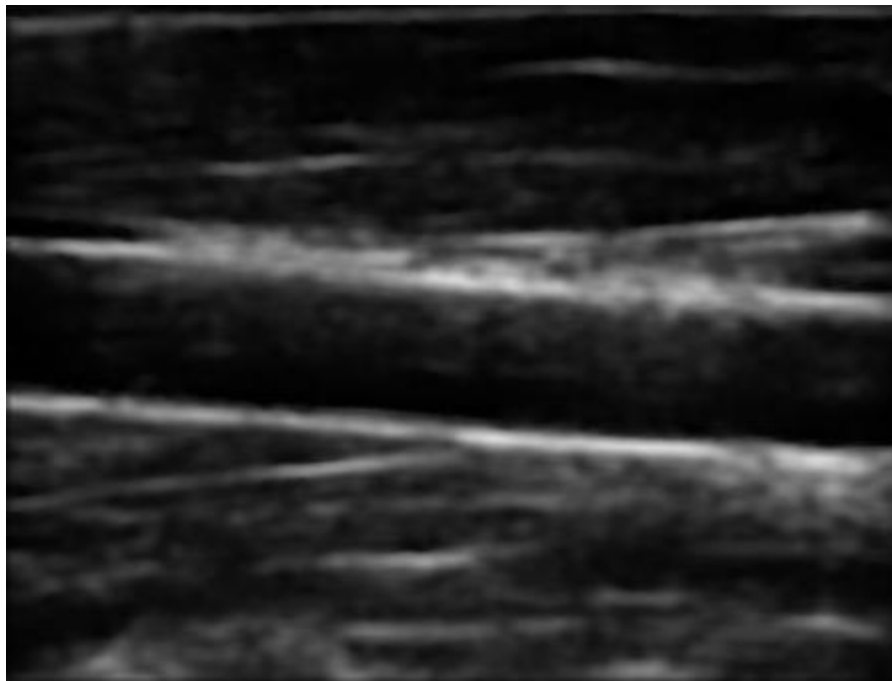


(b)

**Figure 4.35** A  $150 \times 90$  rectangular area at the lower-middle part of each ultrasound image (marked by red rectangle). This area was used for scaling factor calculation.

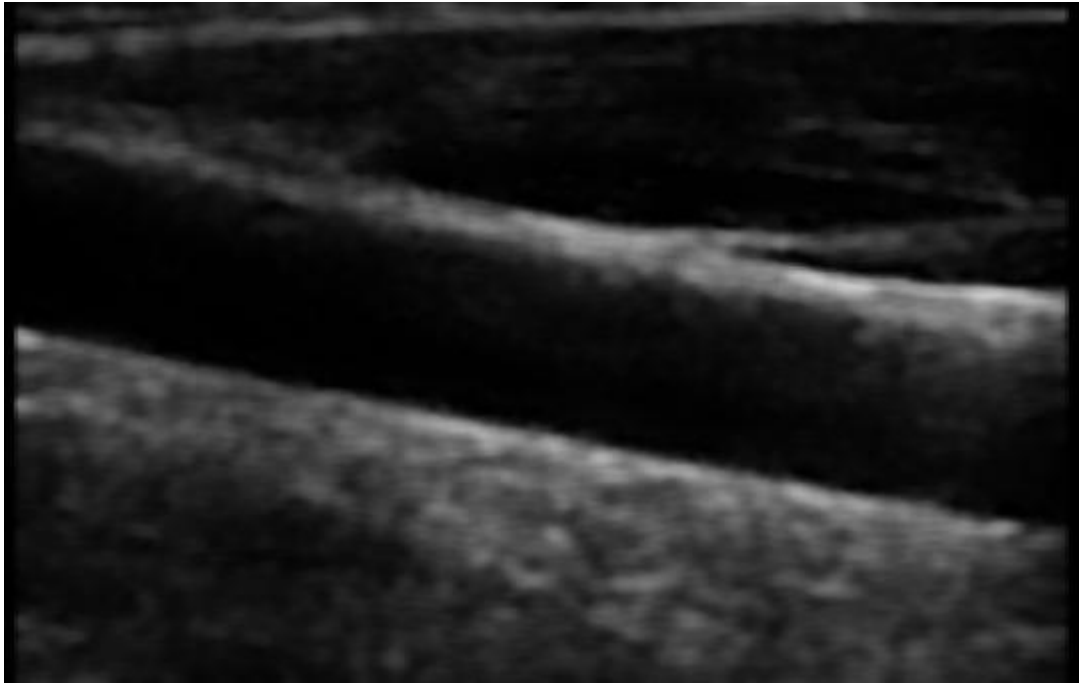


(a)

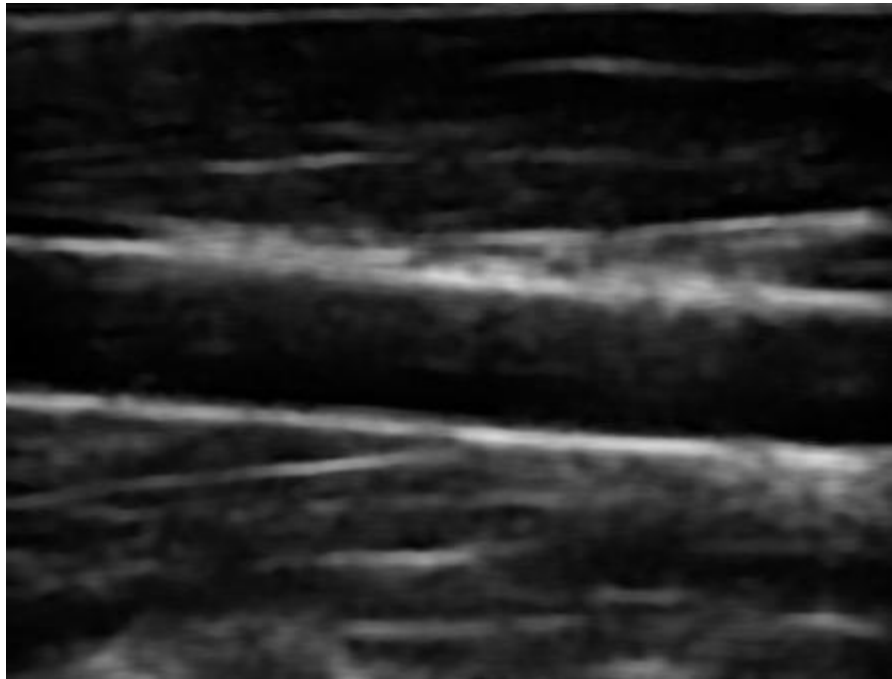


(b)

**Figure 4.36** Ultrasound images of carotid arteries of two different persons de-noised by the Lee filter. (a) De-noised version of Figure 4.32(a), (b) De-noised version of Figure 4.32(b).

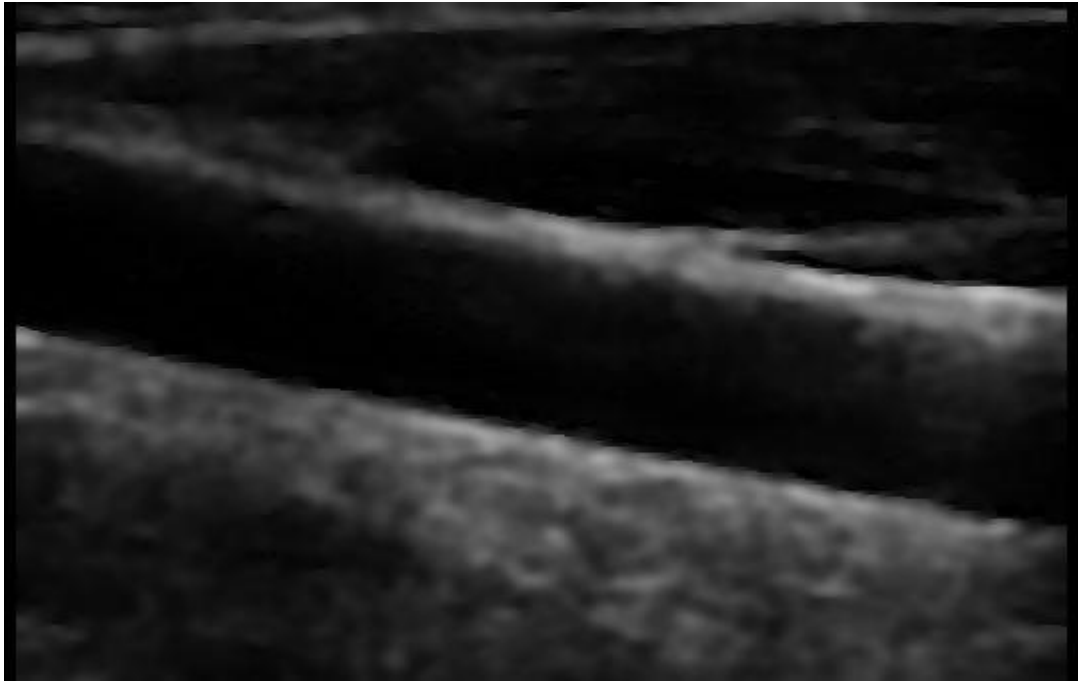


(a)

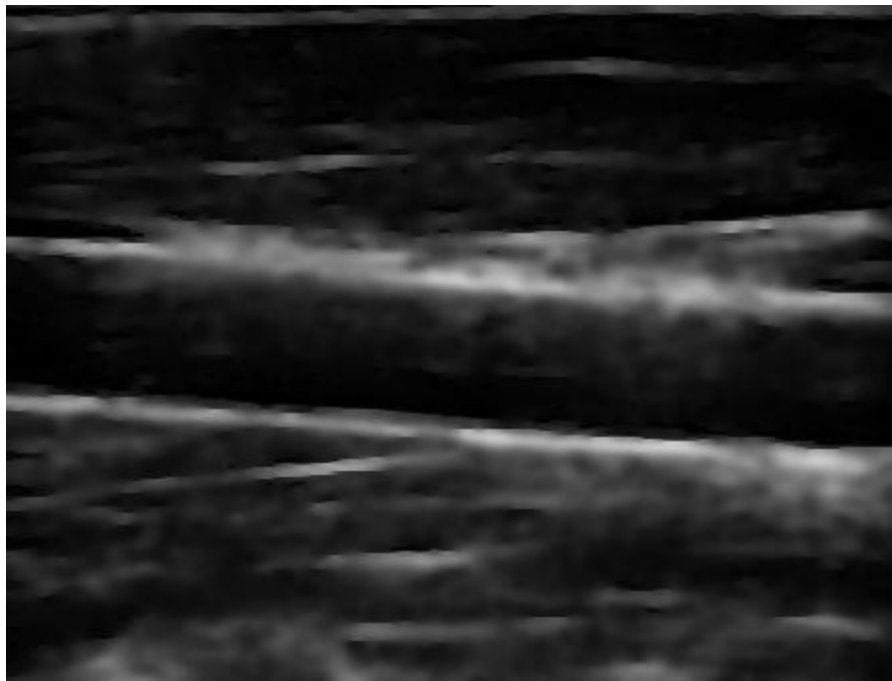


(b)

**Figure 4.37** Ultrasound images of carotid arteries of two different persons de-noised by the Frost filter. (a) De-noised version of Figure 4.32(a), (b) De-noised version of Figure 4.32(b).



(a)



(b)

**Figure 4.38** Ultrasound images of carotid arteries of two different persons de-noised by the homomorphic AD filter. (a) De-noised version of Figure 4.32(a), (b) De-noised version of Figure 4.32(b).

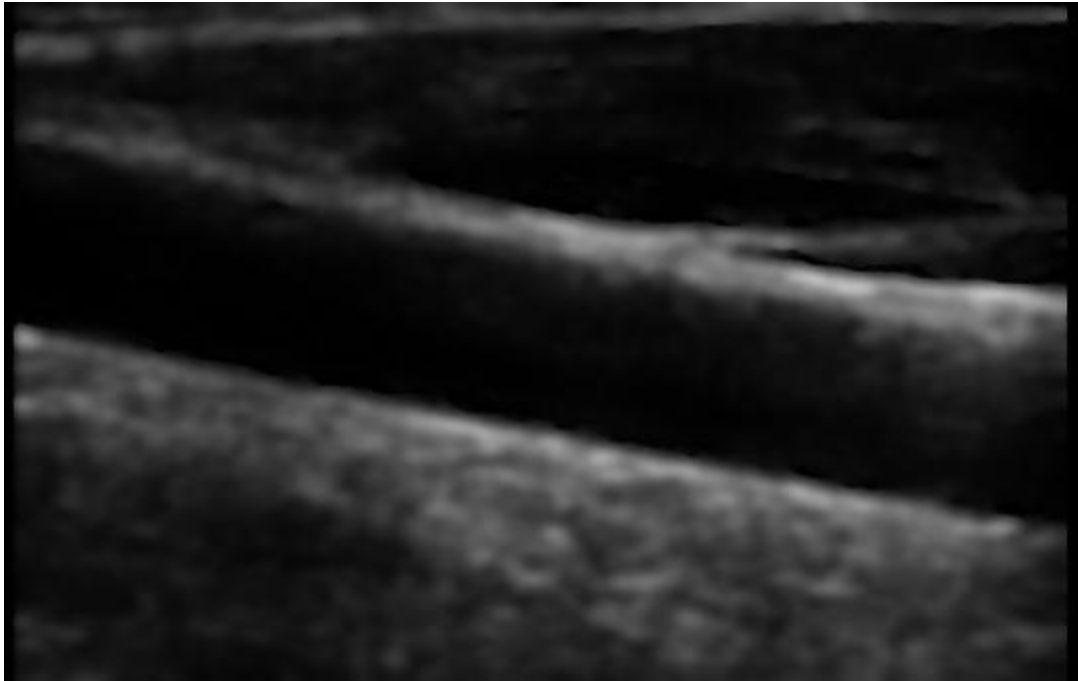


(a)

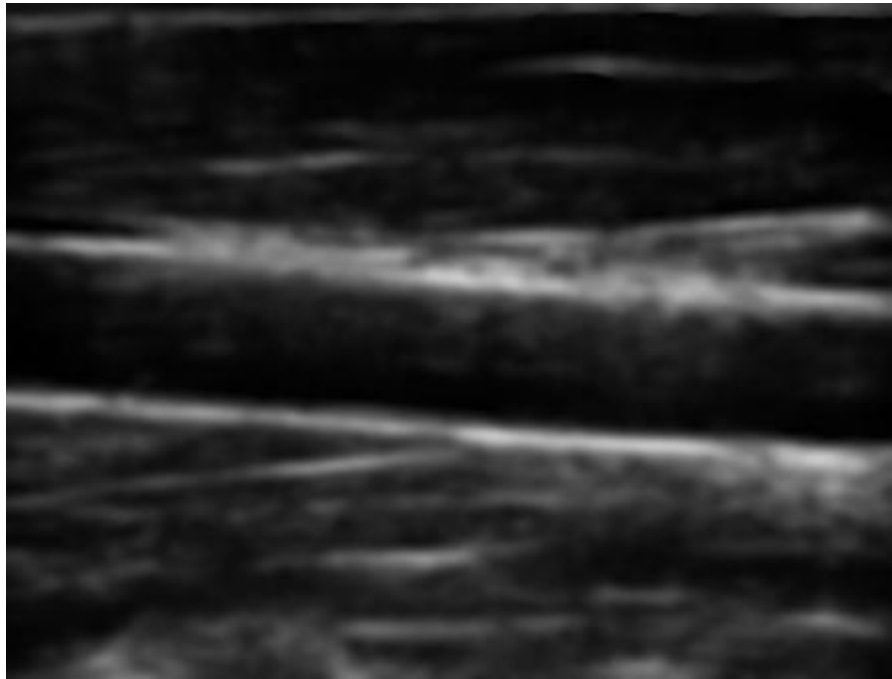


(b)

**Figure 4.39** Ultrasound images of carotid arteries of two different persons de-noised by the DPAD filter. (a) De-noised version of Figure 4.32(a), (b) De-noised version of Figure 4.32(b).



(a)

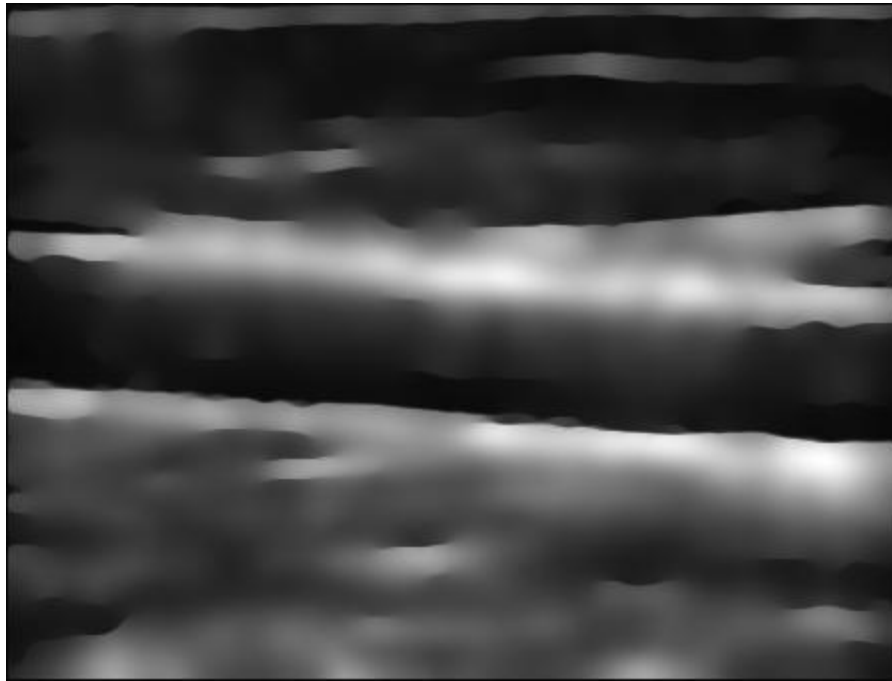


(b)

**Figure 4.40** Ultrasound images of carotid arteries of two different persons de-noised by the SRAD filter. (a) De-noised version of Figure 4.32(a), (b) De-noised version of Figure 4.32(b).



(a)

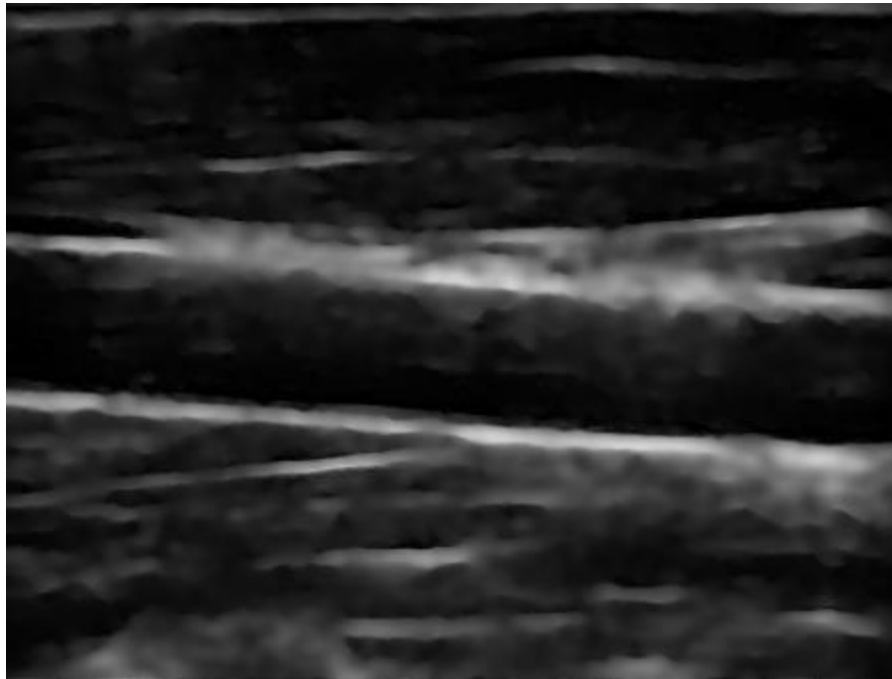


(b)

**Figure 4.41** Ultrasound images of carotid arteries of two different persons de-noised by the OSRAD filter. (a) De-noised version of Figure 4.32(a), (b) De-noised version of Figure 4.32(b).

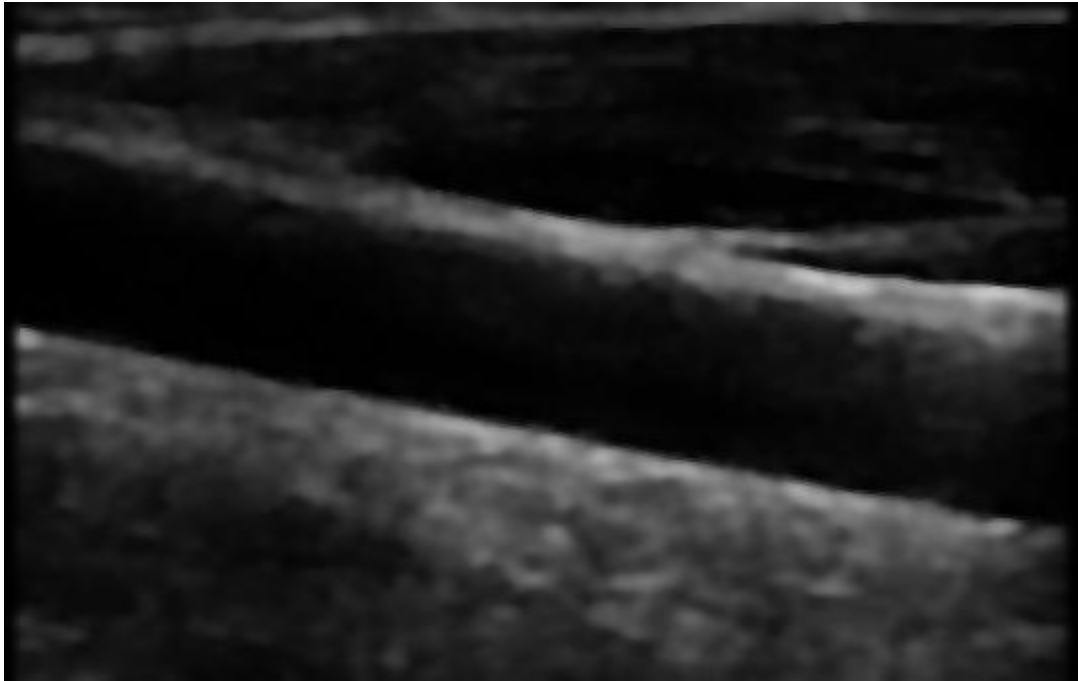


(a)

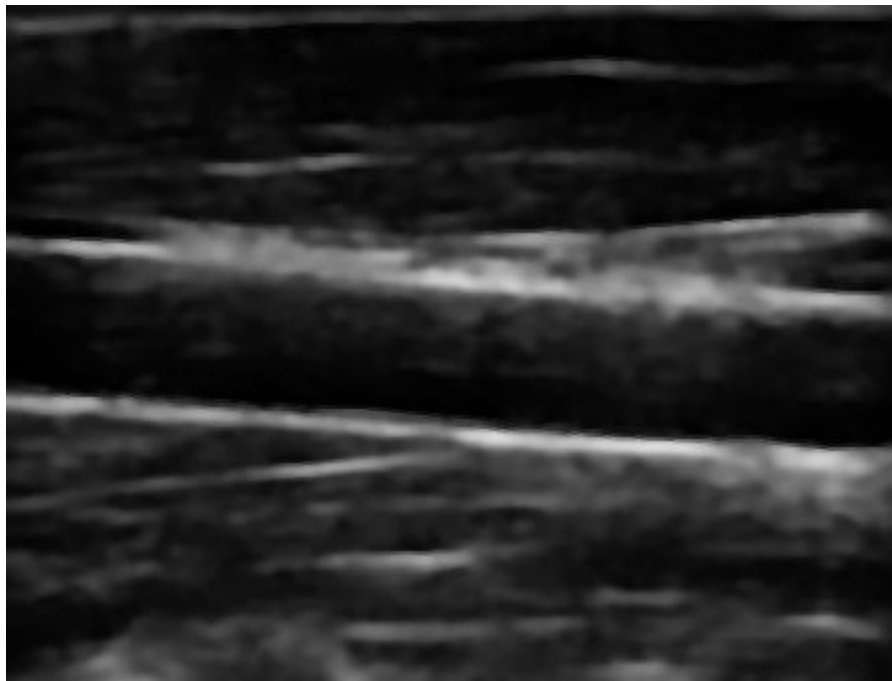


(b)

**Figure 4.42** Ultrasound images of carotid arteries of two different persons de-noised by the REDISRAD-EBF filter. (a) De-noised version of Figure 4.32(a), (b) De-noised version of Figure 4.32(b).



(a)



(b)

**Figure 4.43** Ultrasound images of carotid arteries of two different persons de-noised by the REDISRAD-WDF filter. (a) De-noised version of Figure 4.32(a), (b) De-noised version of Figure 4.32(b).

## 4.5 Overall results discussion

Both analytical and subjective experiments confirm the superiority of our proposed extensions. Between the two proposed extensions, REDISRAD-EBF was more successful compared to REDISRAD-WDF in terms of edge preservation, structural similarity preservation, variance reduction, mean preservation and sharpness of edges. The core competition lies among SRAD, OSRAD, REDISRAD-EBF and REDISRAD-WDF. Throughout the experiments, these four filters convincingly established their superiority over the rest.

In most of the cases of synthetic and semi-synthetic dataset OSRAD showed better variance reduction performance compared to the proposed extensions. We hypothesize that it resulted due to over-smoothing which also affected OSRAD by limiting its capability of mean preservation. The over-smoothing nature of OSRAD is clearly noticeable throughout all experiments. Edge dislocation/broadening and diffused contour boundaries are the byproduct of the over-smoothing nature of OSRAD. The REDISRAD filters showed a superior balance of smoothing and edge-preservation compared to OSRAD and thereby, outperformed OSRAD in every other aspect except variance reduction.

Our proposed filters, especially REDISRAD-EBF, consistently outperformed SRAD filter in every aspects—edge and structural similarity preservation, mean preservation, variance reduction and sharpness of edges. Experiments on real speckled images (SAR and ultrasound) also validated the effectiveness of our proposed filters in real-world applications.

We prefer REDISRAD-EBF over REDISRAD-WDF for two specific reasons. First, empirical results proved the superiority of REDISRAD-EBF over REDISRAD-WDF. Second, performance of REDISRAD-WDF is highly dependent on the tuning of the diffusion function weight constant  $m$ .

## Chapter 5

# Concluding Remarks and Future Work

### 5.1 Conclusion

In this research work, two ratio-based edge detection inspired extensions to SRAD were introduced. Strategies of using a hybrid scaling factor and larger window size for ICOV coefficient calculation were also proposed. One of the proposed extensions, REIDSRAD-EBF, incorporated an edge sensitive boosting factor using the edge information provided by ratio-based edge detection technique. This boosting factor guided the ICOV coefficient of original SRAD model towards better edge detection and thereby improved the overall performance in terms of edge preservation and noise reduction. Being augmented by better edge detection in speckled environment, REDISRAD-EBF also managed to keep the edges sharp in the de-noised output image. The other proposed extension, REDISRAD-WDF, re-defined the diffusion function of original SRAD model as a weighted function of local and global components. The original diffusion function is taken as the local component which is controlled by the ICOV coefficient. REDISRAD-WDF introduced a ratio-based edge detection inspired global diffusion function and used it as the global component of the re-defined weighted diffusion function. The performance of REDISRAD-WDF was very close to that of REDISRAD-EBF. However, edges in the REDISRAD-WDF output are not as sharp as the edges of REDISRAD-EBF output.

Experimental results confirm that both proposed extensions outperformed SRAD in every aspects considered. Our REDIRAD variants significantly outperformed OSRAD in every

other aspect except variance reduction. In some occasions, variance reduction performances of OSRAD were better than the proposed extensions. However, OSRAD sacrificed the edge preservation and edge-sharpness performances for this higher level of variance reduction. Unlike OSRAD, our proposed filters offered a superior balance between variance reduction and edge preservation. Subjective evaluation on some real world speckle images validated the usefulness and relative superiority of our proposed speckle reducing methods.

## 5.2 Future work

The diffusion process employed in our proposed speckle reduction methods is not directional. It will be interesting to verify whether a directional diffusion improves the performance or not. We can use the matrix anisotropic diffusion concept of OSRAD to guide the smoothing process by gradient direction.

A dynamic stopping criterion can also be effective for the proposed extensions. The proposed filters work in iterative fashion. It is important to know how long we should continue de-noising so that the speckled image is sufficiently de-noised and at the same time, finer edge details are kept. This parameter is obviously dependent on the input images. Hence, it would be a good contribution if we can determine the appropriate number of iterations for a specific input image. Some features that can be considered for the dynamic computation of this stopping criterion (i.e., total number of iteration need to be applied) are the noise level of the speckled input image, a measure of the density of edge details in the input image, time step size used etc. Some of these measures can be computed over a small Region of Interest (ROI) selected by the user or alternatively, the entire image can be considered.

We used a fixed time step size for the proposed filters. This parameter is crucial as it directly effects the final update equation. Smaller time step size results in longer processing time and higher accuracy, and vice versa. It will be interesting to see whether an adaptive time step size proves effective or not. For example, if, after certain number of iterations it can be determined that we are in the process of losing too many edge details,

the step size can be decreased to cope with the situation in hand. It is also challenging to determine to which extent the time step size needs to be varied.

REDISRAD-WDF used a pre-defined weight constant in its weighted diffusion function. We believe it will be more effective if we can calculate this constant value dynamically. For an input image with lower level of speckles, the ICOV coefficient driven local component of the weighted diffusion function should contribute more in the final diffusion decision (to which extent an image sub-region should be smoothed). In presence of higher level of speckles, the ratio-based edge detection guided global component should be more pro-active since the gradient and Laplacian based ICOV coefficient provides misleading edge decisions in such an environment. If we manage to get an estimate of the noise level of the input image and adjust the weight constant accordingly, REDISARD-WDF can be more effective.

## References

- [1] J. Lee, "Digital image enhancement and noise filtering by using local statistics," *IEEE Trans. Pattern Anal. Machine Intell.*, vol. PAM1-2, no. 2, 1980.
- [2] J. Lee, "Refined filtering of image noise using local statistics," *Comput. Graph. Image Process.*, vol. 15, no. 4, pp. 380–389, 1981.
- [3] J. Lee, "Speckle suppression and analysis for synthetic aperture radar," *Opt. Eng.*, vol. 25, no. 5, pp. 636–643, 1986.
- [4] V. Frost, J. Stiles, K. Shanmugan, and J. Holtzman, "A model for radar images and its application to adaptive digital filtering of multiplicative noise," *IEEE Trans. Pattern Anal. Machine Intell.*, vol. PAMI-4, no. 2, pp. 157–165, 1982.
- [5] D. Kuan, A. Sawchuk, T. Strand, and P. Chavel, "Adaptive restoration of images with speckle," *IEEE Trans. Acoust., Speech, Signal Processing*, vol. ASSP-35, no. 3, pp. 373–383, 1987.
- [6] Y. Yu and S. Acton, "Speckle reducing anisotropic diffusion," *IEEE Trans. Image Process.*, vol. 11, no. 11, pp. 1260–1270, Nov. 2002.
- [7] K. Krissian, C. Westin, R. Kikinis, and K. Vosburgh, "Oriented speckle reducing anisotropic diffusion," *IEEE Trans. Image Process.*, vol. 16, no. 5, pp. 1412–1424, May 2007.
- [8] S. Acton, "Deconvolutional speckle reducing anisotropic diffusion," *IEEE Int. Conference Image Process.*, vol. 1, pp. I-5-8, Sept. 2005.
- [9] S. Aja-Fernández and C. Alberola-López, "On the estimation of the coefficient of variation for anisotropic diffusion speckle filtering," *IEEE Trans. Image Processing*, vol. 15, no. 9, pp. 2694–2701, Sep. 2006.
- [10] V. Dutt and J. Greenleaf, "Ultrasound echo envelope analysis using a homodyned

- K-distribution signal model,” *Ultrason. Imag.*, vol. 16, pp. 265-287, 1994.
- [11] D. Donoho, “De-noising by soft-thresholding,” *IEEE Trans. Inform. Theory*, vol. 41, no. 3, pp. 613–627, May 1995.
- [12] A. Bovik and D. Munson, Jr., “Boundary detection in speckle images,” *IEEE Int. Conf., Acoust., Speech, Signal Process.*, Tampa, FL, vol. 10, pp. 893-896, 1985.
- [13] H. Guo, J. Odegard, M. Lang, R. Gopinath, I. Selesnick, C. Burrus, “Wavelet based speckle reduction with application to SAR based ATD/R,” *IEEE Int. Conference, Image Process., ICIP-94*, vol. 1. pp. 75-79, 1994.
- [14] H. Rabbani, M. Vafadust, P. Abolbaesumi, S. Gazor, “Speckle Noise Reduction of Medical Ultrasound Images in Complex Wavelet Domain Using Mixture Priors,” *IEEE Trans. Biomed. Engineering*, vol. 55, no. 9, pp. 2152-2160, 2008.
- [15] X. Hao, S. Gao, X. Gao, “A Novel Multiscale Nonlinear Thresholding Method for Ultrasonic Speckle Suppressing,” *IEEE Tans. Med. Imaging*, vol. 18, no. 9, pp. 787-794, 1999.
- [16] A. Jain, *Fundamental of Digital Processing*. Upper Saddle River, NJ: Prentice Hall, 1989.
- [17] R. Harger, *Synthetic Aperture Radar Systems*, New York: Academic, 1970.
- [18] R. Wagner, M. Insana, and D. Brown, “Statistical properties of radiofrequency and envelope-detected signals with applications to medical ultrasound,” *J. Opt. Soc. Amer. A*, vol. 4, no. 5, pp. 910-922, 1987.
- [19] R. Wagner, S. Smith, and J. Sandrik, “Statistics of speckle in ultrasound B-scans,” *IEEE Trans. Son. Ultrason.*, vol. SU-30, no. 3, pp. 156-163, May 1983.
- [20] H. C. Andrews and B. R. Hunt, *Digital Image Restoration*. Englewood Cliffs, NJ: Prentice-Hall, 1977.
- [21] K. Castleman, *Digital Image Processing*. Englewood Cliffs, NJ: Prentice-Hall,

1979.

- [22] H. Arsenault and M. Levesque, "Combined homomorphic and local-statistics processing for restoration of images degraded by signal-dependent noise," *Appl. Opt.*, vol. 23, no. 6, Mar 1984.
- [23] P. Perona and J. Malik, "Scale space and edge detection using anisotropic diffusion," *IEEE Trans. Pattern Anal. Machine Intell.*, vol. 12, no. 9, pp. 629–639, 1990.
- [24] A. Bovik, "On Detecting Edges in Speckle Imagery," *IEEE Trans. Acoustic, Speech, Signal Process.*, vol. 36, no. 10, pp. 1618-1627, 1988.
- [25] G. Gerig, O. Kübler, R. Kikinis, and F. Jolesz, "Nonlinear anisotropic filtering of MRI data," *IEEE Trans. Med. Imag.*, vol. 11, no. 6, pp. 221–232, Jun. 1992.
- [26] H. Kim, K. Park, H. Yoon, G. Lee, "Speckle reducing anisotropic diffusion based on direction of gradient," *IEEE Int. Conference on Adv. Language Process. and Web Info.Tech.*, pp. 198-203, July 2008.
- [27] R. Srivastava, J. R. P. Gupta, H. Parthasarthy, "Complex diffusion based speckle reduction from digital images," *IEEE Conference on Methods and Models in Computer Science*, pp. 1-6, Dec 2009.
- [28] G. Wentzel, *Quantum theory of fields*, New York, pp. 177, 1949.
- [29] S. Liu, J. Wei, B. Feng, W. Lu, B. Denby, Q. Fang and J. Dang, "An anisotropic diffusion filter for reducing speckle noise of ultrasound images based on separability," *IEEE Conference on Signal and Image Processing*, pp. 1 – 4, Dec 2012.
- [30] G. Strang, "Wavelets," *American Scientist*, vol. 82, pp. 250-255, 1992.
- [31] J. Fourier, *Théorie Analytique de la Chaleur*, Paris: Chez Firmin Didot, père et fils, 1822.

- [32] R. Gopinath and C. Burrus, *Wavelets: A Tutorial in Theories and Applications*, Academic Press, San Diego, CA, pp. 603-654, 1992.
- [33] J. Quistgaard, "Signal acquisition and processing in medical diagnostic ultrasound," *IEEE Signal Processing Mag.*, pp. 67–74, Jan. 1997.
- [34] M. Karaman, M. Kutay, and G. Bozdagi, "An adaptive speckle suppression filter for medical ultrasonic imaging," *IEEE Trans. Med. Imag.*, vol. 14, no. 2, pp. 283–292, June 1995.
- [35] J. Mallet and P. Courmontagne, "A new wavelet thresholding approach for SAS images denoising," *OCEANS*, pp. 1-6, 2006.
- [36] M. Bhuiyan, M. Ahmad, M. Swami, "Spatially adaptive thresholding in wavelet domain for despeckling of ultrasound images," *IET, Image Process.*, vol. 3, no. 3, pp. 147-162, 2009.
- [37] A. Bovik, "On Detecting Edges in Speckle Imagery," *IEEE Trans. Acoust., Speech, Signal Process.*, vol. 36, no. 10, pp. 1618-1627, 1988.
- [38] M. Zaman and C. Moloney, "A comparison of adaptive filters for edge-preserving smoothing of speckle noise", *Proc. ICASSP 93 (Minneapolis)*, April 1993, pp. 77-80.
- [39] M. Zaman and C. Moloney, "Evaluation of edge detection for images with non-additive noise", *Proceedings of NECEC 93 (St. John's, Canada)*, April 1993.
- [40] Z. Bai, P. He, "An improved ratio edge detector for target detection in SAR images," *IEEE Int. Conference on Neural Net. and Signal Process.*, pp. 982-985, Dec 2003.
- [41] S. Ganugapati and C. Moloney, "A Ratio Edge Detector for Speckled Images Based on Maximum Strength Edge Pruning," *Proceedings of Int. Conference on Image Process.*, IEEE, vol. 2, pp. 165-168, Oct. 1995.

- [42] D. Ballard and C. Brown, *Computer Vision*. Englewood Cliffs, NJ: Prentice-Hall, 1982.
- [43] D. Marr and E. Hildreth, "Theory of edge detection," *Proc. Roy. Soc. London B*, vol. 207, pp. 187-217, 1980.
- [44] J. Canny, "A computational approach to edge detection," *IEEE Trans. Pattern Anal. Mach. Intell.*, vol. PAMI-8, no. 6, pp. 679-698, 1986.
- [45] Y. Yu and S. Acton, "Edge detection in ultrasound imagery using the instantaneous coefficient of variation," *IEEE Trans. Image Process.*, vol. 13, no. 12, pp. 1640–1655, Dec. 2004.
- [46] Jet Propulsion Laboratory, NASA, <http://www.jpl.nasa.gov/>, last seen in July, 2012.
- [47] Signal Processing Laboratory, <http://splab.cz/en>, last seen in July, 2012.
- [48] W. Pratt, *Digital Image Processing*, New York: Wiley, 1978.
- [49] Z. Wang, A. Bovik, H. Sheikh, and E. Simoncelli, "Image quality assessment: From error visibility to structural similarity," *IEEE Trans. Image Process.*, vol. 13, no. 4, pp. 600–612, 2004.

# Curriculum Vitae

**Name:** Asaduzzaman Babu

**Post-secondary Education and Degrees:** B.Sc. in Computer Science and Engineering  
Chittagong University of Engineering and Technology (CUET)  
Chittagong, Bangladesh  
2001-2006

**Honours and Awards:** University of Western Ontario Graduate Teaching Assistantship  
and Graduate Research Scholarship, 2011-2013

University Merit Scholarship, CUET, Bangladesh  
2001-2006

1<sup>st</sup> Merit Position in the Computer Science and Engineering  
Department, CUET, Bangladesh, 2006.

**Related Work Experience:** Teaching Assistant  
Computer Science Department, The University of Western Ontario  
London, Ontario, N6A5B7, Canada  
Sept 2011- April 2013

Research Assistant  
Computer Science Department, The University of Western Ontario  
London, Ontario, N6A5B7, Canada  
Sept 2011-April 2013

**Publications:**  
[1] A. Babu, M. El-Sakka, "SRAD with Weighted Diffusion Function," International  
Conference on Image Analysis and Recognition, Portugal, June 2013.